Titre: Title:	Time Domain Quantum Light Source Based On Bright Spontaneous Parametric Down Conversion
Auteur: Author:	Joseph Lamarre
Date:	2025
Type:	Mémoire ou thèse / Dissertation or Thesis
Référence: Citation:	Lamarre, J. (2025). Time Domain Quantum Light Source Based On Bright Spontaneous Parametric Down Conversion [Mémoire de maîtrise, Polytechnique Montréal]. PolyPublie. https://publications.polymtl.ca/67687/

URL de PolyPublie: PolyPublie URL:	https://publications.polymtl.ca/67687/
Directeurs de recherche: Advisors:	Nicolas Godbout
Programme: Program:	Génie physique

POLYTECHNIQUE MONTRÉAL
affiliée à l'Université de Montréal

Time Domain Quantum Light Source Based On Bright Spontaneous Parametric Down Conversion

JOSEPH LAMARRE
Département de génie physique

Mémoire présenté en vue de l'obtention du diplôme de *Maîtrise ès sciences appliquées*
Génie physique

Août 2025

POLYTECHNIQUE MONTRÉAL
affiliée à l'Université de Montréal

Ce mémoire intitulé :

Time Domain Quantum Light Source Based On Bright Spontaneous Parametric Down Conversion

présenté par **Joseph LAMARRE**
en vue de l'obtention du diplôme de *Maîtrise ès sciences appliquées*
a été dûment accepté par le jury d'examen constitué de :

Denis SELETSKIY, président
Nicolas GODBOUT, membre et directeur de recherche
Philippe ST-JEAN, membre externe

DEDICATION

To the fond memories I made at Polytechnique,
those times will always stay with me...
Aux beaux souvenirs de Polytechnique,
ces temps me manqueront...

ACKNOWLEDGEMENTS

I first thank Dr. Stéphane Virally, whose foresight in conceiving this project, steady support throughout my master's journey, and insistence on rigorous critical thinking have shaped my academic foundations.

I am equally grateful to Professor Nicolas Godbout for steadfast supervision and guidance, both academically and professionally.

To Mikael Leduc and the engineering-physics technical team, thank you for the practical wisdom and hands-on assistance that kept the experiments running.

To my lab mates who made the work both possible and enjoyable. Thank you Collin Dietrich, for sharing long hours at the optical table, and Rodrigo Becerra, whose optimism and fiber-whispering skills lifted most setbacks.

To the members of my Jury, Professor Denis Seletskiy, whose inventive insights continually broadened my perspective, and Professor Philippe St-Jean, whose clear instruction helped shape the foundation of this thesis, I am grateful for the time and expertise you shared.

Finally, I owe my deepest appreciation to my partner, my four-legged companion, my family and friends for their unwavering support beyond the lab.

RÉSUMÉ

Cette thèse fait progresser l'optique quantique dans le domaine temporel en réunissant théorie, ingénierie de source et expérimentation au sein d'une plateforme partiellement fibrée pour la génération de paires de photons brillantes et spectralement pures. Elle développe d'abord la fonction de Wigner chronocyclique et, par décomposition en valeurs singulières de sa version discrétisée, définit le nombre de Schmidt chronocyclique K_{C} comme indicateur rigoureux de la pureté conjointe temps–fréquence indépendant du choix de base. Des simulations sur des peignes de fréquences modulés par de la dispersion et l'automodulation de phase, ainsi que des reconstructions complètes obtenues grâce à un montage SHG-FROG, confirment que cette approche reconstruit fidèlement les statistiques du champ et relie K_{C} au nombre de Schmidt conventionnel qui quantifie l'intrication spectrale des états biphotoniques issus du processus SPDC.

À l'aide de ce métrique, un source femtoseconde clé en main est réalisée. Un laser à fibre dopée à l'erbium auto-synchronisé, géré en dispersion, livre des impulsions de 1560 nm avec 228 mW de puissance moyenne à 121.6 MHz et une compression en espace libre les réduit à 110 fs. Puis un cristal périodiquement polarisé MgO:PPLN double la fréquence avec 45% de rendement pour fournir une pompe de 780 nm avec une puissance moyenne de 91 mW. L'analyse chronocyclique montre que l'impulsion fondamentale ($K_{\mathrm{C}} = 1.64$) et son harmonique ($K_{\mathrm{C}} = 1.18$) s'approche la limite monomode, satisfaisant ainsi les exigences de pureté des interactions non linéaires quantiques.

Enfin, le processus SPDC de type II femtoseconde est démontrée dans un cristal de niobate de lithium périodiquement polarisé. Une cartographie par seconde harmonique inverse classique fixe l'accord de phase optimal à une périodicité de 10 µm et 135 °C, prédisant 5×10^5 paires s^{-1} en régime de faible gain. Sous illumination de la source ci-haut décrite, ces conditions génèrent des faisceaux actifs et oisifs collinéaires avec une polarisation orthogonal et une brillance mesurée d'environ 6.9×10^6 paires s^{-1}. Ensemble, le cadre théorique, le pompe haute pureté et la source SPDC de démonstration posent les bases d'un système fibrés capable de fournir des paires de photons dégénérées à large bande pour la métrologie quantique et la tomographie optique cohérente à faible dose et haute résolution.

ABSTRACT

This thesis advances time-domain quantum optics by uniting new theory, source engineering, and experiment into a single fiber-based platform for bright, spectrally pure photon-pair generation. The chronocyclic Wigner-function formalism is first developed and, through a singular-value decomposition of the discretized distribution, yields the chronocyclic Schmidt number K_{C} as a rigorous, mode-agnostic gauge of joint time–frequency purity. Numerical studies on dispersion- and self-phase-modulation-shaped frequency combs, together with full reconstructions acquired on an in-house SHG-FROG apparatus, confirm that the SVD faithfully reproduces field statistics and links K_{C} to the conventional Schmidt number that quantifies spectral entanglement in biphoton SPDC states.

Building on this metric, a turn-key femtosecond pump is realized: a dispersion-managed, mode-locked Er-fiber laser delivers 228 mW, 1560 nm pulses at 121.6 MHz; free-space compression shortens them to 110 fs, and a MgO-doped PPLN crystal doubles the frequency with 45% efficiency, providing a 91 mW, 780 nm pump. Chronocyclic analysis shows that both the fundamental ($K_{\mathrm{C}} = 1.64$) and frequency-doubled ($K_{\mathrm{C}} = 1.18$) pulses approach the single-mode limit, satisfying the stringent purity requirements of quantum nonlinear optics.

Finally, femtosecond type-II SPDC is demonstrated in a periodically poled lithium-niobate bulk crystal. Classical backward-SHG mapping identifies optimal phase matching at a 10 μm grating and 135°C, predicting 5×10^5 pairs s^{-1} in the low-gain regime. Under the engineered pump these conditions yield collinear, cross-polarised signal and idler beams with a measured brightness of $\sim 6.9 \times 10^6$ pairs s^{-1}. Together, the theoretical framework, high-purity pump, and proof-of-concept SPDC source lay the groundwork for a turnkey, fiber-based system capable of delivering broadband, degenerate photon pairs for quantum-enhanced metrology and low-dose, high-resolution optical coherence tomography.

TABLE OF CONTENTS

LIST OF TABLES

LIST OF FIGURES

LIST OF SYMBOLS AND ACRONYMS

BBO	Beta Barium Borate
CEO	Carrier–Envelope Offset
COPRA	Common Pulse Retrieval Algorithm
CW	Continuous Wave
EDFA	Erbium-Doped Fiber Amplifier
FWHM	Full Width at Half Maximum
GDD	Group Delay Dispersion
GNLSE	Generalized Nonlinear Schrödinger Equation
GVD	Group Velocity Disperion
GVM	Group Velocity Mismatch
i-RIN	integrated-RIN
MO	Master Oscillator
MgO:PPLN	Magnesium Oxide-doped Periodically Poled Lithium Niobate
PMF	Phase Matching Function
PPKTP	Periodically Poled Potassium Titanyl Phosphate
PPLN	Periodically Poled Lithium Niobate
PSD	Power-Spectral Density
RIN	Relative Intensity Noise
RMS	Root Mean Square
SAM	Saturable-Absorber Mirror
SESAM	Semiconductor Saturable-Absorber Mirror
SGF	Sum-Frequency Generation
SHG	Second Harmonic Generation
SHG-FROG	Second Harmonic Generation Frequency-Resolved Optical Gating
SPDC	Spontaneous Parametric Down-Conversion
SPM	Self Phase Modulation
SVD	Singular Value Decomposition
TBP	Time Bandwidth Product
TOD	Third-Order Dispersion
WDM	Wavelength Division Multiplexer

LIST OF APPENDICES

CHAPTER 1 INTRODUCTION

Bright quantum states of light with noise characteristics below the Poissonian (shot-noise) limit are fast becoming the foundation of next-generation metrology and imaging [1,2]. Their landmark use in the Laser Interferometer Gravitational-Wave Observatory delivered the first direct observation of gravitational waves, showcasing that quantum enhancement can boost sensitivity in kilometer-scale interferometers by several decibels [3]. Pushing these techniques further, toward brighter, broadband, and spectrally engineered sources, promises to extend the same quantum advantage to other fields [4, 5]. In particular, quantum-enhanced optical coherence tomography, a proposed biomedical application of the work presented here, could pair sub-micron depth resolution with reduced illumination levels, enabling real-time, high-contrast imaging of living tissue while keeping photo damage to a minimum [6–8].

Quantum optics has long been anchored in the spectral domain because Continuous Wave (CW) single-frequency lasers pre-dated reliable ultrafast sources. In the canonical $\chi^{(2)}$ process of Spontaneous Parametric Down-Conversion (SPDC), vacuum fluctuations split each CW pump photon into a lower-energy signal–idler pair, producing states with narrow linewidths, well-defined frequencies, and long coherence times [9]. Studies therefore centered on metrics such as wavelength correlations, phase-matching bandwidth, and spectral line-shape. Yet CW pumping delivers only megahertz-scale pair rates at most [10–12], limited bandwidth, and modest brightness, far from ideal for noisy, real-world applications. Further, the signal–idler biphotons are strongly frequency-anti-correlated [13]: detecting or filtering one photon fixes its twin's spectrum, cutting heralding efficiency and complicating experiments that demand indistinguishable pairs.

Time-domain quantum optics flips the traditional frequency-first view. It champions ultrashort pulses, tens to hundreds of femtoseconds long, as the primary resource [14]. The goal is to generate, manipulate, and measure quantum states whose defining features live in sub-picosecond time windows and multi-terahertz spectral spreads.

The shift to time-domain quantum optics became both feasible and practical once two enabling technologies matured. Ultrafast pump sources like mode-locked femtosecond fiber lasers now deliver sub-100 fs pulses at tens to hundreds of megahertz repetition rates [15, 16], combining Watt level average power with gigawatt-scale peak power. Such high instantaneous intensities dramatically increase the nonlinear interaction strength within even sub-millimeter samples. In parallel, engineered non-linear media such as periodically poled, quasi-phase-matched lithium niobate (PPLN) and potassium titanyl phosphate (PPKTP)

can be fabricated with user-defined poling periods, duty cycles, and apodisation profiles. These design freedoms flatten and broaden the phase-matching response, allowing a single femtosecond pump to satisfy energy–momentum conservation over tens of terahertz [17]. Waveguide implementation have further boosted the effective nonlinearity by orders of magnitude [18]. When femtosecond pulses drive SPDC in such a medium, the pair-production rate can leap from the megahertz realm of CW pumping to the gigahertz regime, equivalent to $\approx 10\,\mu\mathrm{J}$ of energy per pulse converted into biphotons [19].

Crucially, if the joint biphoton spectrum can be engineered to be both spectrally degenerate (same central frequency,) and produced under type-II phase matching such that the signal and idler exit in orthogonal polarizations, the output will be spectrally indistinguishable but separable entangled twin beams. Such bright, broadband sources of nonclassical light could unlock the generation of novel high information quantum states. For example, intensity post-conditioning schemes propose to continuously sample the idler arm's pulse-to-pulse energy and reject shots whose intensity lies outside a predefined window. The retained signal pulses then exhibit sub-Poissonian intensity noise, ideal for quantum-enhanced metrology [20].

Several intertwined challenges still hamper bright, pulsed, type-II SPDC sources. First, ultrashort pulses are inherently fragile: even a few millimeters of optics or nonlinear crystal introduce material dispersion, group-velocity mismatch, and pulse-front tilt that blur the signal-idler joint spectrum. This in turn erodes separability and conversion efficiency [21]. Precise dispersion engineering, chirped poling, aperiodic quasi-phase matching, and external pre-chirping, must therefore be paired with in-situ diagnostics capable of resolving sub-picosecond structures.

Second, theoretical models lag behind. Focusing effects in bulk SPDC remain only partially modeled [22], and the pulsed regime adds extra dimensions: temporal walk-off, pump-chirp and spatial–spectral coupling that existing formalisms treat only approximately [23]. Classical pump descriptors such as the time-bandwidth product reduce the rich spectro-temporal field to a single number and miss the high-order phase and modal structures that drive nonlinear interactions. What is needed is a framework that captures the full joint amplitude and phase of both pump and biphoton fields and quantifies the number of independent spectro-temporal channels participating in the interaction. Developing these advanced models will be critical to push pulsed SPDC sources from laboratory systems into robust bright sources for quantum-enhanced metrology.

1.1 Research Objectives

This thesis therefore pursues three intertwined objectives. First, the realization of a dispersion-managed, low-noise femtosecond pump: a fiber-based laser chain delivering sub-100 fs pulses with gigawatt-scale peak power, $< 1\%$ pulse-to-pulse energy jitter, and a flat spectral phase across a $\sim$20 THz bandwidth. Careful consideration of the system dispersion, integration of bulk-optic compressors, and active diagnostic tools will enable the suppression of higher-order dispersion so that the pump itself occupies a single, high-purity spectro-temporal mode.

Second, the work will provide a proof of concept for bright, degenerate type-II SPDC by coupling this pump into a periodically poled lithium-niobate crystal engineered for broadband, collinear phase matching at 1560 nm. The target is to exceed megahertz-level pair-production rates while maintaining spectral degeneracy and orthogonal polarizations.

Third, a comprehensive characterization framework will be developed to extract the full joint amplitude and phase of both pump and biphoton fields. This toolkit will report the effective spectro-temporal mode count of the pump and the SPDC state, quantify modal overlap in non-linear interactions, and reveal residual correlations after dispersion management thereby establishing clear performance benchmarks for quantum-enhanced metrology.

1.2 Thesis Outline

The thesis opens in Chapter 2 with a survey of the literature on bright spontaneous-parametric-down-conversion (SPDC) sources pumped by femtosecond lasers. After retracing the historical dominance of continuous-wave systems, the chapter compares modern strategies, such as waveguide confinement, apodized quasi-phase matching, and dispersion engineering, that have pushed pair rates into the gigahertz regime while suppressing spectral entanglement. This review establishes the performance benchmarks and practical obstacles that motivate the experimental work that follows.

Chapter 3 introduces the analytical backbone of the project: a chronocyclic-Wigner formalism combined with singular-value decomposition to determine the modal composition of a source. The chapter first derives the framework mathematically, applies it to phase-modulated frequency combs, then presents an experimental retrieval protocol that reconstructs the joint temporal–spectral field of any ultrafast optical state. Crucially, the formalism delivers a basis-independent Schmidt-mode count that links the number of usable spectro-temporal modes in the pump to those in the down-converted biphotons.

Chapter 4 turns to the heart of the hardware: the dispersion-managed, mode-locked erbium-

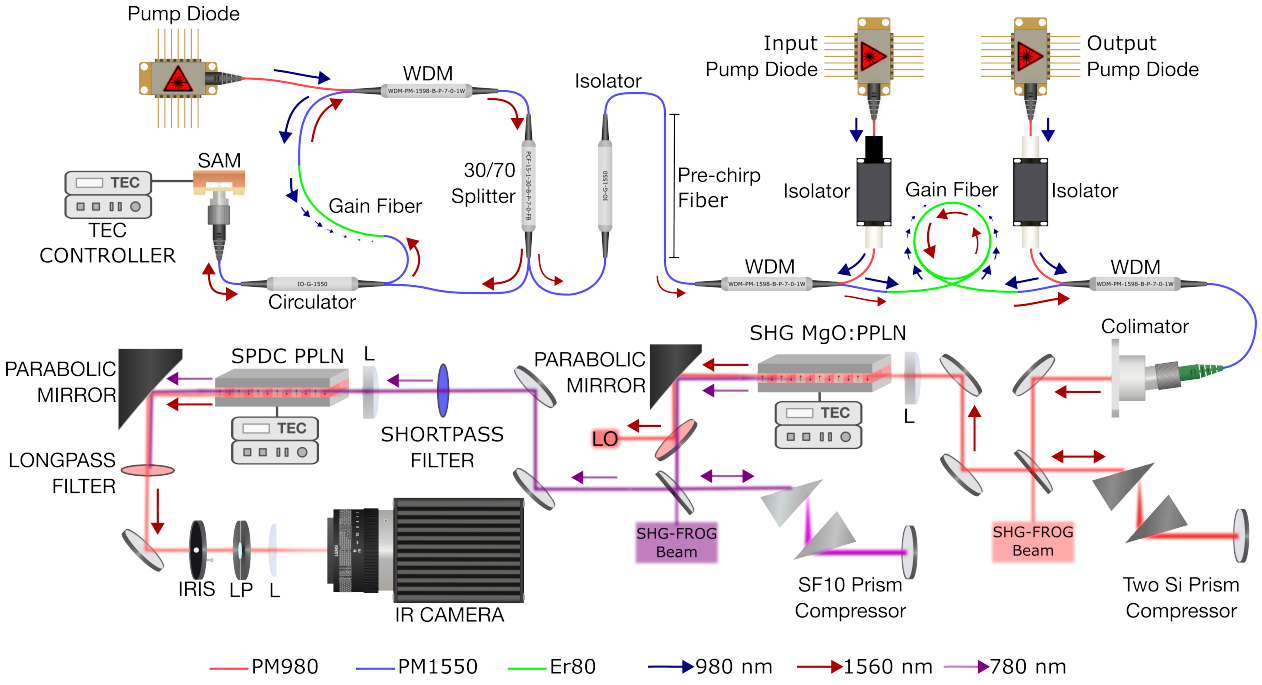

Figure 1.1 Experimental platform developed in this thesis. The top panel depicts the dispersion-managed, amplified mode-locked erbium-doped fiber laser (Chapter 4), including its pump diodes, gain fiber, Saturable-Absorber Mirror (SAM), isolators, and pre-chirp stage. The lower-right branch shows frequency-doubling in an MgO:PPLN crystal (also Chapter 4), where the 1560 nm pulses are compressed and up-converted to 780 nm to seed the Spontaneous Parametric Down-Conversion (SPDC) experiments. The lower-left branch highlights the broadband, degenerate type-II SPDC stage PPLN, imaged onto an infrared camera for the proof-of-concept study (Chapter 5). Throughout the system, colored fibers and free-space paths trace the wavelength coding used in subsequent diagrams (PM980 blue, PM1550 green, 980 nm navy, 1560 nm purple, 780 nm red). Chapter 3 employs the chronocyclic-Wigner/SVD formalism to quantify the spectro-temporal mode count of both the femtosecond pump and the biphotons generated at every stage illustrated.

doped fiber laser that provides ∼100 fs pulses at 1560 nm, and the downstream second-harmonic generation stage in MgO-doped PPLN that doubles the frequency to 780 nm. Detailed descriptions of cavity design, saturable-absorber dynamics, and active dispersion compensation are followed by pulse-characterization results that verify gigawatt-scale peak power and $< 1\%$ pulse-to-pulse jitter.

Chapter 5 delivers the proof-of-concept demonstration of bright, degenerate type-II SPDC. The chapter presents infrared-camera images and flux estimates that support megahertz-level pair production. Although sub-Poissonian statistics are not yet measured, the experiment validates polarization separation, and pump-to-pair brightness transfer, prerequisites for subsequent noise-reduction protocols.

Finally, Chapter 6 synthesizes the theoretical and experimental findings, evaluates remaining challenges and charts a path toward fully deployable, quantum-enhanced metrology systems.

CHAPTER 2 LITERATURE REVIEW

Spontaneous Parametric Down-Conversion (SPDC) has established itself as a mainstay for laboratory and field deployable sources of non-classical light. In this $\chi^{(2)}$ process a pump photon at frequency ω_p is annihilated inside a nonlinear crystal, giving rise to a pair of lower–energy "signal" and "idler" photons whose joint quantum state can exhibit strong entanglement in polarization, time–frequency, or spatial-mode degrees of freedom. Of the three phase-matching classes; type-0 (all fields co-polarized), type-I (signal/idler co-polarized and orthogonal to the pump), and type-II (signal and idler cross-polarized), the type-II degenerate configuration ($\omega_s \simeq \omega_i \simeq \omega_p/2$) is uniquely valuable for quantum-metrology. It produces polarization-entangled twin beams directly from the crystal, eliminating interferometric post-processing and furnishing a robust resource for sub-shot-noise intensity and phase estimation, entanglement-enhanced interferometry, and other precision-measurement protocols [24–26].

Over the past three decades the focus has shifted from merely observing entanglement to engineering photon-pair sources that are bright, spectrally pure, and compatible with modern photonic-quantum platforms. A source is typically labeled bright once it delivers 10^6 pairs/s/mW, into a single spatial mode, or under a more objective metric, a spectral brightness of $\gtrsim 10^3$ pairs/s/mW/nm [27–29]. Practical usefulness, however, is usually determined by six intertwined figures of merit [30]. High spectral purity ($\gtrsim 0.9$) ensures factorable and separable joint spectra states that have photon number entanglement when heralded. Heralding efficiency is the probability of detecting (or coupling) one photon conditioned on its twin; critical for scaling to multi-photon conditioning experiments. Spectral brightness, in pairs/s/mW/nm sets raw data-rate ceilings. Collection efficiency or fiber-coupling loss governs the detected rather than internal pair flux. Finally, two-photon interference visibility, e.g. Hong–Ou–Mandel visibilities > 0.90, certifies that independent photons are indistinguishable in all degrees of freedom, and state fidelities (> 0.95), the overlap with a target state, prove that the desired entanglement survives propagation and filtering. High visibility and fidelity are where brightness meets quality: even a megahertz-level source is of limited value if residual distinguishability drags visibility below ≈ 0.85 or if state fidelity falls under fault-tolerance thresholds. Experiments such as the femtosecond-pumped Periodically Poled Potassium Titanyl Phosphate (PPKTP) Sagnac source of Kim et al. [31] and the ultrabright CW pumped PPKTP of Park et al. [29] demonstrate that careful dispersion engineering and mode matching can achieve pair rates above 1 MHz/mW while maintaining Hong–Ou–Mandel visibilities ≈ 0.95 and Bell-state fidelities ≥ 0.97; proving that brightness, purity, visibility, and fidelity need not be traded off but can be co-optimized to deliver bright, degenerate, and

nearly separable quantum states.

While CW pumping simplifies phase-matching and naturally yields narrowband photons, the emergence of ultrafast lasers has motivated a pivot to femtosecond-pulsed SPDC. Pulsed pumping offers high peak intensities (boosting gain and hence brightness), intrinsic timing information that aligns with pump–probe spectroscopy [32] and quantum sensing protocols [33], and compatibility with time-bin multiplexing schemes [34]. The drawback is broader phasematching bandwidths and stronger time–frequency entanglement, which, if unmanaged, reduce heralded-photon purity. The work of Mosley [35] demonstrated that careful group-velocity-matching in PPKTP could reconcile femtosecond durations with near-factorable joint spectra, marking a turning point in pulsed type-II SPDC engineering.

This review traces the field's evolution thematically. It begins with CW-pumped type-II SPDC, from the first Bell-tests to today's record-bright, fiber-coupled sources in Sagnac interferometers and nanophotonic waveguides. Next, it explains why femtosecond pumping was adopted, summarizing high-gain type-0/-I SPDC to frame brightness limits and nonlinear challenges. The core of the review examines bright, femtosecond, degenerate type-II SPDC: early bulk results, hurdles from spatial walk-off and GVM, and the transformative impact of quasi-phase-matching in PPKTP, PPLN, and thin-film platforms. Finally, it catalogs implementations; bulk crystals, ridge waveguides, periodically poled fibers, and chip-scale resonators, emphasizing the brightness–purity–integration trade-offs. These advances map a rapid arc, from kilohertz pair rates in centimeter-scale bulk crystals to multi-gigahertz, sub-picosecond entangled streams from chip-level devices. Control of the underlying design and material strategies is now key to pushing brightness and purity into the deterministic, multiplexed regime required for next-generation quantum metrology.

The modern era of polarization-entangled photon sources began when Kwiat et al. showed that a single 2 mm Beta Barium Borate (BBO) crystal, pumped by a 351 nm argon-ion CW laser, could produce high-visibility (97%) type-II, degenerate SPDC without post-selection [36]; their set-up violated Bell's inequality by 100σ in under 5 minutes, establishing type-II SPDC as a scalable entanglement source. Four years later, the same group introduced a two-crystal sandwich geometry that co-axially superposed the ordinary and extraordinary down-conversion cones [27]. Branded an "ultrabright" source, it delivered $> 10\times$ higher detected pair-rate per milliwatt than the 1995 experiment, around 10^3 pairs/s/mW, and relaxed spatial-mode filtering requirements.

Further increases in brightness came with quasi-phase-matched bulk crystals. Replacing birefringent BBO with PPKTP suppressed spatial walk-off and enabled centimeter-long interaction lengths under relaxed pump focusing. A representative milestone is Jeong et al.,

who pumped a 10 mm PPKTP crystal with a 405 nm CW diode laser and reported 7×10^3 pairs/s/mW into single-mode fiber (99% fidelity) and 9×10^4 pairs/s/mW into multimode fiber [37]. Subsequent variants exploited non-collinear phase-matching or dual-wavelength pumping to push detected rates above 10^5 pairs/s/mW while preserving $> 95\%$ entanglement visibility [12].

Novel pumping schemes such as embedding the crystal inside a polarization-Sagnac interferometer to eliminate the long-term phase drift that plagued early bulk arrangements, has also pushed brightness by allowing simultaneous collection of the $|\mathrm{HH}\rangle$ and $|\mathrm{VV}\rangle$ amplitudes. A current benchmark for fiber-coupled brightness is by Park et al. [29], a 30 mm PPKTP Sagnac source that delivers a spectral brightness of 2.0 MHz/mW/nm ($\approx 2 \times 10^6$ pairs/s/mW at 1 nm bandwidth) with a 97.8 % Bell-state fidelity, an order-of-magnitude jump over pre-2020 reports. Careful Gaussian spatial mode matching accounts for the dramatic improvement, highlighting the importance of pump and collection-waist optimization.

Although bulk optics still hold the absolute-brightness record, integrated platforms are rapidly closing the gap. Kim et al. [38] monolithically combined a multimode interferometer, two PPLN waveguides, and a polarization splitter–rotator on 4 cm^2 of X-cut thin-film $LiNbO_3$. Driven by a 774 nm CW pump, the chip yields 5.1×10^8 pairs/s/mW (purity ≈ 0.90, fidelity ≈ 0.94), one of the brightest integrated type-II source to date. Kellner et al. [39] introduced the first counter-propagating type-II SPDC on lithium-niobate-on-insulator, generating spectrally uncorrelated pairs with 92 % purity without filtering; crucial for deterministic on-chip multi-photon interference. Cheng et al. demonstrated a hybrid Si_xN_y PPLN waveguide operating in a cascaded Second Harmonic Generation (SHG)–SPDC scheme, delivering 2.9×10^7 pairs/s/mW of self-referenced photons.

Over three decades, CW-pumped type-II SPDC has climbed from kilohertz pair rates in 2 mm BBO to MHz mW^{-1} in centimeter-scale poled crystals, and on thin-film $LiNbO_3$ on-insulator chips, to nearly GHz mW^{-1}. Early ridge-waveguide PPLN/PPKTP devices (2008–2020) had already matched bulk brightness at the milliWatt level; the newest thin-film platforms now erase the remaining two-order gap while adding fiber pigtails, thermo-electric stabilization, and electro-optic tuning. Enabled by quasi-phase matching (removing spatial walk-off), self-referenced Sagnac geometries (passive phase stability), and high-confinement waveguides (strong $\chi^{(2)}$ with preserved polarization), this progression establishes the brightness–purity benchmark against which femtosecond-pumped sources must be judged.

As mentioned, the switch from CW to femtosecond pumping was driven by three practical gains. First, peak power: a 100 fs, 80 MHz train packs $\geq 10^5 \times$the peak intensity of a CW beam with the same average power, driving the $\chi^{(2)}$ interaction into high gain and boosting

pair rates from kHz to multi-GHz. Second, intrinsic timing: the 10–12ns pulse spacing gates coincidences, suppresses dark counts, and syncs seamlessly with pump–probe or clock-distribution schemes. Third, system compatibility: ultrafast lasers already underpin several modern sensing technologies. Seeding SPDC with the same source simplifies integration and stabilization across quantum-photonic experiment on attosecond spectroscopy [40], optical frequency combs [41] and nonlinear microscopy [42].

Femtosecond pumping, however, changes the phasematching problem qualitatively. Ultrashort pumps widen the spectrum by terahertz, putting group-velocity mismatch on center stage: unless $v_{g,p} = v_{g,s} = v_{g,i}$, strong frequency correlations erode heralded purity. Keller & Rubin's model [43] showed that bulk BBO or KDP cannot yield factorable femtosecond biphotons without pump or material dispersion engineering. Spatial walk-off adds another handicap for birefringent, non-collinear geometries, restricting crystal length and pump-waist optimization. High peak powers also push sources into the high-gain regime, where pump depletion, self-/cross-phase modulation, and stimulated emission reshape the spectrum.

Before turning to type-II sources, it is useful to recall milestones in other phase-matching classes that set the current ceiling for brightness and bandwidth achievable by dispersion engineering.

Triginer et al. quantified the macroscopic SPDC regime by using cascaded stimulated emission to chart gain up to ≈ 60 pairs per pulse [44]. In parallel, dispersion-engineered thin-film $LiNbO_3$ ridges have since pushed performance further, yielding 17 THz-wide biphoton spectra at 2.1 µm with sub-cycle correlations and 8.1 GHz mW^{-1} brightness, two orders of magnitude beyond the best CW sources [45]. The term bright squeezed vacuum was coined in a type-I, 3 mm BBO experiment at 400 nm, which produced $\sim 10^6$ photons per pulse and revealed quantum correlations far beyond the single-photon regime [46]. Subsequent femtosecond-pumped, double-pass PPLN sources extended this to $> 10^6$ photons per pulse [47]. Most recently, bright squeezed vacuum has been harnessed to drive solid-state high-harmonic generation, producing XUV light more efficiently than classical beams of equal mean intensity and underscoring femtosecond SPDC as a gateway to strong-field quantum photonics [48].

Whilst ultrafast sources are common type-0 and type-I SPDC research, the dedicated literature on femtosecond-pumped, degenerate type-II sources remains sparse. The papers below stand out as the most complete experimental demonstrations to date.

Early interferometric work by Kim et al. demonstrated that the poor two-photon visibility long associated with femtosecond-pumped, type-II SPDC in thick BBO crystals could be fully recovered [49]: by placing the crystal pair inside a Mach–Zehnder interferometer, they erased the arrival-time information that distinguishes the $|\mathrm{HV}\rangle$ and $|\mathrm{VH}\rangle$ amplitudes,

yielding high-fidelity Bell states without resorting to narrowband filters or sub-millimetre crystals. A decade later, Eckstein et al. pushed the concept from proof-of-principle to practical brightness: a ∼250 fs pulse train driving a 10 mm PPKTP waveguide produced heralded photons with an effective spectral-mode count $K_{\mathrm{Q}} = 1.05$ without any additional filtering, at detected rates of roughly 19×10^6 pairs/s. By spectrally shaping the pump, exploiting quasi-phase-matching to minimize signal–idler Group Velocity Mismatch (GVM), and using a waveguide geometry to eliminate spatial walk-off, the experiment proved that femtosecond bandwidths need not preclude high-quality, single-mode polarization entanglement [50].

Yet the demonstrations also laid bare the core obstacles predicted by Keller & Rubin [43]: terahertz pump bandwidth inflating the Schmidt number through residual GVM, the need to work with low pump powers to avoid self-phase modulation, etc. The lever for overcoming those liabilities is currently a combination of quasi-phase-matching and wavelength-tuning for intrinsic GVM. Systematic surveys of KTP-family isomorphs by Laudenbach et al. mapped dozens of new GVM windows from 600 nm to 2 µm [51], widening the materials palette, while recent chirped crystals have theoretically stretched the phase-matching bandwidth toward the single-cycle regime without sacrificing spectral purity [52].

Weston et al. engineered a factorable source that simultaneously delivers high heralding efficiency, near-unit purity, and Bell-state fidelity in the telecom band [53]. Using a 170 fs pump centred at 785 nm to drive a 2 mm PPKTP crystal (poling period 46.15 µm), they met the GVM condition for degenerate emission around 1570 nm. Matching the crystal length to the pump bandwidth (5.35 nm) produced a nearly circular joint spectral amplitude, and Hong–Ou–Mandel interference between independent sources reached $(100 \pm 5)\%$ visibility, direct evidence of single-mode purity.

Jin et al. pushed the same GVM principle to wide tunability. With 2 ps Ti:sapphire pulses and a 30 mm PPKTP crystal they reported Schmidt numbers of 1.01–1.04 at 1565 nm, 1584 nm, and 1655 nm, maintaining spectral purity above 0.81 across the entire S-, C-, L- and U-bands [54]. Although the pump is picosecond rather than femtosecond, the result illustrates how the GVM window in KTP can be exploited for broadband telecom operation without sacrificing purity.

Building on that platform, Jin et al. inserted the 30 mm GVM-PPKTP crystal into a bidirectionally pumped Sagnac loop. Picosecond pulses (792 nm, 76 MHz) generated degenerate 1584 nm pairs with Bell state fidelities of 0.981 (for $|\psi^-\rangle$) and 0.980 (for $|\psi^+\rangle$), detected by high-efficiency superconducting nanowire single-photon detector [55].

An earlier benchmark for pulsed Sagnac operation is Kuzucu & Wong. Driven by 50 ps, 390 nm pump pulses, their 10 mm PPKTP Sagnac source produced 0.01 entangled pair per

pulse in a 0.15 nm bandwidth at 780.7 nm with only 1 mW average power [31]. At low generation probability they measured 99% two-photon-interference visibility, and a tomography-verified singlet fidelity of 98.9%. Although narrow-band and visible-wavelength, this work established the Sagnac loop as a robust architecture for high-quality pulsed type-II entanglement.

Although these sources deliver high-quality states, their detected pair flux still falls short of the high brightness routinely attained in femtosecond-pumped type-0 and type-I SPDC. The short-fall is largely intrinsic: the effective nonlinear tensor element for type-II interactions is smaller, and the orthogonal polarizations reduce spatial overlap, so conversion efficiency remains closer to the CW benchmark than to the ultrabright pulsed type-0/-I regime. Nevertheless, the papers reviewed here show that by exploiting group-velocity matching in engineered media, Schmidt numbers of ≈ 1, Bell-state fidelities greater than 0.98, and multi-MHz detected pair rates per milliwatt are achievable.

The body of work surveyed in this review shows that dispersion-engineered, quasi-phase-matched media can reconcile femtosecond pumping with high-fidelity type-II entanglement, yet brightness remains constrained by the intrinsically lower conversion efficiency of type-II interactions. A natural next frontier is therefore to raise flux without sacrificing purity, through strategies such as shortening crystals to suppress walk-off while boosting nonlinearity with higher d_{eff} materials, deploying waveguide or nanophotonic confinement to enhance pump intensity, and incorporating resonant or cavity-enhanced geometries that recycle the pump to amplify the down-converted fields.

In this thesis we pursue the first of these avenues: a short, group-velocity-matched PPLN crystal exploiting the large d_{31} coefficient (compared to other media) of $LiNbO_3$ to offset the reduced interaction length. The goal is to deliver CW level pair flux while retaining the ultrafast timing and near-single-mode purity established by earlier PPKTP demonstrations, thereby moving type-II femtosecond SPDC closer to the brightness benchmark set by type-0 and type-I sources.

CHAPTER 3 SPECTRO-TEMPORAL MODE ANALYSIS VIA SINGULAR VALUE DECOMPOSITION OF THE CHRONOCYCLIC WIGNER FUNCTION

This chapter introduces the chronocyclic Wigner-function framework [56], which jointly characterizes optical signals in the spectral and temporal domain. Building on its quantum counterpart, key properties of the chronocyclic Wigner function are derived and a compact measure of spectro-temporal purity is defined: the chronocyclic Schmidt number K_{C}, obtained by applying singular-value decomposition to a discretized version of the Wigner distribution. This Singular Value Decomposition (SVD)-based description, an original contribution of this work, is shown to faithfully reproduce the field's statistics, confirming K_{C} as a rigorous, mode-agnostic metric for joint time–frequency characterization.

This method is first validated on simulated frequency combs whose spectral phases encode first-, second-, and third-order dispersion, as well as Self Phase Modulation (SPM). Next, an experimental platform built around an in-house Second Harmonic Generation Frequency-Resolved Optical Gating (SHG-FROG) [57] setup that enables full chronocyclic Wigner reconstruction of real pulses is described. Finally, the link between K_{C} and the Schmidt number describing spectral entanglement in a biphoton SPDC state is established.

3.1 Chronocyclic Wigner Function and Its SVD

Intuition on the chronocyclic Wigner function can be gained by looking at the original quantum Wigner function. The development of this function was spurred by Dirac's insight on the link between quantum commutators and classical Poisson brackets, $[\hat{q}, \hat{p}] = i\hbar\{q, p\}$. Here, the canonical variables q and p are dynamical functions in phase space governed by Hamilton's equation, and $\hat{q}$ and $\hat{p}$ their corresponding quantized operator forms. This link suggested the possibility of expressing quantum states directly in phase space, the natural playground of statistical mechanics. Whereas classical ensembles and their time evolution are described by true probability densities $\rho(q, p, t)$, quantum systems are specified by wavefunctions or, more generally, density operators $\hat{\rho}$. The question was therefore posed: can one construct a phase-space representation of $\hat{\rho}$ that preserves the full quantum content? No mapping yields a strictly positive, fully faithful probability density, yet the Wigner function, a quasi-probability distribution that permits negativity, has proved to be an effective bridge between operator formalism and phase-space, and its usefulness has only expanded since its original proposal. This is worth mentioning as like its quantum analog, the chronocyclic

Wigner function introduced in (3.5) is not itself a physical observable, but it is a powerful tool for extracting experimentally testable quantities such as instantaneous frequency, group delay, and spectro-temporal mode content.

Although the phase-space distribution now known as the Wigner function bears Eugene Wigner's name, it was independently derived in several different contexts. Wigner himself first proposed it, although without any justification, to account for quantum mechanical corrections to thermodynamic equilibrium. For a quantum state described by a density operator $\hat{\rho}(q, q')$ in the position space with the dynamical position function $q(x)$, or $\hat{\rho}'(p, p')$ in momentum space, it reads

$$\begin{aligned} W(q,p) &= \frac{1}{2\pi\hbar}\int_{-\infty}^{\infty} d\Delta x\, e^{-\frac{i}{\hbar}p\Delta x}\hat{\rho}\left(q+\frac{\Delta x}{2}, q-\frac{\Delta x}{2}\right) \\ &= \frac{1}{2\pi\hbar}\int_{-\infty}^{\infty} d\Delta p\, e^{\frac{i}{\hbar}x\Delta p}\hat{\rho}'\left(p+\frac{\Delta p}{2}, p-\frac{\Delta p}{2}\right). \end{aligned} \tag{3.1}$$

Casting the two-point amplitude q in terms of center and difference coordinate variables, $q = (x+x')/2$, and $\Delta x = x - x'$, with similar definitions for p and Δp, three useful perspectives emerge [58]. First, the kernel $\rho(q + \Delta x/2,\, q - \Delta x/2)$ is simply the density matrix viewed in a coordinate frame rotated by 45° in the (x, x') plane. Moving along q follows the diagonal of the original matrix (average position), while varying Δx probes the off-diagonal terms about q. The amplitude of Δx quantifies the strength of the coherence across two coordinate points. Second, the Wigner function is obtained by a Fourier transform of this rotated kernel with respect to Δx. Momentum p thus plays the role of the conjugate variable to the separation Δx; high-frequency oscillations in the off-diagonals translate into large-momentum structure in $W(q, p)$. Third, because the position and momentum wave-functions are related by a single Fourier transform, the density matrix in the two bases, $\hat{\rho}(q, q')$ and $\hat{\rho}'(p, p')$, are connected by a double Fourier transform. Rotating the coordinate-space density matrix by 45° into center and difference coordinates and then performing an inverse Fourier transform over the relative coordinate leads directly to the second form of (3.1). In this way the Wigner function lays a phase-space portrait that treats the two conjugate variables symmetrically, revealing coherence and correlation features that remain hidden in either marginal alone.

Just as position and momentum wave-functions are related by a Fourier transform, the temporal envelope of an optical field, $E(t)$, and its spectrum, $\tilde{E}(\omega) = \mathcal{F}[E(t)]$, form a conjugate pair. The (t, ω) plane lacks the symplectic structure of a true Hamiltonian phase space, yet it forms a pseudo-phase-space known as chronocyclic space. The chronocyclic Wigner function is constructed by applying the same "rotate-and-Fourier" recipe used for the quantum

Wigner distribution, starting from the two-time field correlation function,

$$\Gamma(t_1, t_2) = \langle E^*(t_1)E(t_2)\rangle\,. \tag{3.2}$$

Structurally, $\Gamma(t_1, t_2)$ is a Hermitian, positive-semidefinite kernel on time, like a "density matrix" for first-order coherence; by contrast, the quantum density matrix $\hat{\rho}$ in 3.1 is a unit-trace operator encoding the full many-photon state. For quantum states with a positive Wigner representation (e.g. coherent or thermal light), the normally ordered quantum two-time correlation function reduces to $\Gamma(t_1, t_2)$. However, $\Gamma(t_1, t_2)$ captures only first-order statistics and reconstructs the field or state fully only for deterministic or Gaussian statistics, whereas $\hat{\rho}$ contains higher-order correlations unavailable from $\Gamma(t_1, t_2)$ alone. Introducing the center time $t = (t+t')/2$ and the delay $\Delta t = t-t'$, one defines the centered correlation function

$$C(t, \Delta t) = \langle E(t + \frac{1}{2}\Delta t)E^*(t - \frac{1}{2}\Delta t)\rangle. \tag{3.3}$$

A double Fourier transform, first with respect to t, then with respect to Δt, yields the two-frequency correlation

$$\tilde{C}(\omega, \Delta\omega) = \langle \tilde{E}(\omega + \frac{1}{2}\Delta\omega)\tilde{E}^*(\omega - \frac{1}{2}\Delta\omega)\rangle, \tag{3.4}$$

where $\Delta\omega$ is the frequency difference. Finally, an inverse Fourier transform over $\Delta\omega$, or a Fourier transform over Δt, gives the chronocyclic Wigner function

$$\begin{aligned} W_C(t, \omega) &= \frac{1}{\sqrt{2\pi}} \int_{-\infty}^{\infty} d\Delta\omega\, \tilde{C}(\omega, \Delta\omega) e^{-i\Delta\omega t} \\ &= \frac{1}{\sqrt{2\pi}} \int_{-\infty}^{\infty} d\Delta\omega\, \langle \tilde{E}(\omega + \frac{1}{2}\Delta\omega)\tilde{E}^*(\omega - \frac{1}{2}\Delta\omega)\rangle e^{-i\Delta\omega t}, \\ \text{or} \qquad W_C(t, \omega) &= \frac{1}{\sqrt{2\pi}} \int_{-\infty}^{\infty} d\Delta t\, \langle E(t + \frac{1}{2}\Delta t)E^*(t - \frac{1}{2}\Delta t)\rangle e^{i\omega\Delta t}. \end{aligned} \tag{3.5}$$

Note that the chronocyclic Wigner function of a single optical pulse can also be constructed without taking the averages. Applying some of the insight gained from the quantum Wigner function, in the chronocyclic picture the "density matrix" is the two-time field correlation $\Gamma(t_1, t_2)$. Scanning along the "diagonal" term t tracks the intensity at the mean time of arrival. Varying the "off-diagonal" term Δt measures how strongly two temporal points correlate. Large values of Δt with non-zero correlation indicate long-range temporal coherence, something expected in a well-defined pulse train. The chronocyclic Wigner function $W_C(t, \omega)$ is obtained by a Fourier transform of the rotated kernel with respect to the relative coordi-

nate Δt. The conjugate variable ω therefore encodes how rapidly the field oscillates across that delay. Rapid, high-frequency structures in the off-diagonals of Γ maps onto broad-band features in W_{C}; conversely, smooth off-diagonal terms correspond to a narrow spectral distribution. The resulting Wigner surface provides a joint map of when the energy resides (the t axis) and how fast it oscillates there (the ω axis), revealing correlations that are not readily apparent when looking at the temporal nor spectral intensity alone.

Three key properties of the Wigner function can also be applied to its chronocyclic analog [59]. The first is the inner product rule, which for quantum states $\hat{\rho}_1, \hat{\rho}_2$ reads $\mathrm{Tr}(\hat{\rho}_1\hat{\rho}_2) = 2\pi\hbar \iint W_{\rho_1} W_{\rho_2}\, dq\, dp$. For two deterministic optical fields $E_1(t)$ and $E_2(t)$ with their chronocyclic Wigner functions defined as

$$W_C(t,\omega) = \frac{1}{2\pi}\int_{-\infty}^{\infty} d\Delta t\, E_k\Big(t+\frac{1}{2}\Delta t\Big)\; E_k^*\Big(t-\frac{1}{2}\Delta t\Big)\, e^{-i\omega\Delta t}, \qquad k=1,2, \tag{3.6}$$

the inner-product identity is

$$\iint_{-\infty}^{\infty} dt\, d\omega\; W_1(t,\omega)\, W_2(t,\omega) \;=\; \frac{1}{2\pi}\Big|\langle E_1|E_2\rangle\Big|^2 \tag{3.7}$$

where the usual field overlap is

$$\langle E_1|E_2\rangle \;=\; \int_{-\infty}^{\infty} E_1(t)\, E_2^*(t)\, dt \;=\; \frac{1}{2\pi}\int_{-\infty}^{\infty} \tilde{E}_1(\omega)\, \tilde{E}_2^*(\omega)\, d\omega. \tag{3.8}$$

The chronocyclic inner-product identity links field overlaps to Wigner overlaps. For a single pulse $E_1 = E_2$, $\iint W^2\, dt\, d\omega = \frac{1}{2\pi}\Big(\int |E(t)|^2\, dt\Big)^2$, which is simply the pulse energy squared. If the mixed integral $\iint W_1 W_2\, dt\, d\omega$ vanishes, the two pulses are orthogonal. By these projection rules, pulse overlaps and orthogonality can be evaluated directly in (t,ω) space, providing the mathematical footing for mode-analysis via SVD of the discrete Wigner distribution.

Second, the chronocyclic Wigner function also inherits the Radon-transform, or projection property of its quantum analog. For any direction in the (t,ω) plane specified by real coefficients (a,b) (with $a^2+b^2=1$ for convenience), define the rotated coordinate $\chi = a\,t + b\,\omega$. Integrating W_C along the line orthogonal to this direction gives

$$P_{a,b}(\chi) = \iint W_C(t,\omega)\, \delta\Big(\chi - at - b\omega\Big)\, dt\, d\omega = \frac{1}{2\pi}\Big|\mathcal{E}_{a,b}(\chi)\Big|^2, \tag{3.9}$$

where $\mathcal{E}_{a,b}(\chi)$ is the field obtained after a fractional Fourier rotation by an angle $\theta = \arctan(b/a)$. Thus, the one-dimensional marginal $P_{a,b}(\chi)$ is the intensity distribution of the "quadrature" observable $a\,t + b\,\omega$. Two familiar special cases are readily discerned:

$P_{1,0}(t) = |E(t)|^2$ recovers the temporal power profile, and $P_{0,1}(\omega) = \frac{1}{2\pi}|\tilde{E}(\omega)|^2$ produces the optical spectrum. Intermediate angles correspond to analyzing the pulse after linear dispersive propagation or time-lens operations. Because every such projection is experimentally accessible with passive optics, recording a sufficient set of $P_{a,b}(\chi)$ enables full tomographic reconstruction of $W_C(t,\omega)$, enabling the retrieval of optical pulses [60] and mirroring quadrature tomography in quantum phase space.

The third important property, a direct corollary of the projection property is its normalization condition: integrating the chronocyclic Wigner function over the entire (t,ω) plane returns the total pulse energy. Indeed,

$$\iint_{-\infty}^{\infty} W_C(t,\omega)\,dt\,d\omega \;=\; \int_{-\infty}^{\infty}\Big(\int_{-\infty}^{\infty} W_C(t,\omega)\,d\omega\Big)\,dt \;=\; \int_{-\infty}^{\infty}|E(t)|^2\,dt \;=\; U, \tag{3.10}$$

where U is the pulse energy (or simply 1 if the field is energy-normalized). Because the frequency marginal $\int W_C\,dt$ equals the spectral intensity $|\tilde{E}(\omega)|^2$, the double integral necessarily converges to the same value as the energy obtained from the temporal envelope, $U = (2\pi)^{-1}\int|\tilde{E}(\omega)|^2 d\omega$. Thus the chronocyclic Wigner distribution is properly normalized: its total "mass" equals the physical energy carried by the optical field.

It is also worth mentioning that for a field $E(t) = |E(t)|e^{i\phi_t(t)}$ (and $\tilde{E}(\omega) = |\tilde{E}(\omega)|e^{i\phi_\omega(\omega)}$), the chronocyclic Wigner function gives direct moment formulas for the local phase slopes. Its first spectral moment at fixed t yields the instantaneous frequency

$$\omega_{\text{inst}}(t) = \frac{\displaystyle\int_{-\infty}^{\infty}\omega\,W_C(t,\omega)\,d\omega}{\displaystyle\int_{-\infty}^{\infty}W_C(t,\omega)\,d\omega} = \frac{d\phi_t(t)}{dt}, \tag{3.11}$$

while its first temporal moment at fixed ω gives the group delay

$$t_{\text{gr}}(\omega) = \frac{\displaystyle\int_{-\infty}^{\infty} t\,W_C(t,\omega)\,dt}{\displaystyle\int_{-\infty}^{\infty}W_C(t,\omega)\,dt} = \frac{d\phi_\omega(\omega)}{d\omega}. \tag{3.12}$$

In other words, the centroids of the Wigner distribution along ω and t directly return the temporal and spectral phase derivatives.

To apply an SVD to the chronocyclic Wigner function, it is first discretized into matrix form. N_t temporal samples $t_m = m\Delta t$ and N_ω spectral samples $\omega_n = n\Delta\omega$ are selected, choosing Δt and $\Delta\omega$ such that $\Delta t\,\Delta\omega < 2\pi/(N_t N_\omega)$ to satisfy the Nyquist criteria. Numerically evaluating (3.5) on this grid can be efficiently performed via FFT-based convolution and

yields the array

$$W_{mn} = W_C(t_m, \omega_n), \qquad m = 0 \dots N_t - 1,\ n = 0 \dots N_\omega - 1. \tag{3.13}$$

For a finite-energy field the continuous Wigner distribution integrates to the pulse energy U, so the discrete array is rescaled to unit "mass",

$$\mathbf{W}_{mn} = \frac{W_{mn}}{\sum_{m=0}^{N_t-1} \sum_{n=0}^{N_\omega-1} W_{mn}}, \qquad \sum_{m,n} \mathbf{W}_{mn} = 1. \tag{3.14}$$

The matrix $\mathbf{W} \in \mathbb{R}^{N_t \times N_\omega}$ is now ready for singular-value decomposition.

With the chronocyclic Wigner distribution discretized as a normalized $N_t \times N_\omega$ matrix $\mathbf{W}$, it is factored via a singular-value decomposition,

$$\mathbf{W} = \mathbf{U}\,\mathbf{\Sigma}\,\mathbf{V}^\dagger, \qquad \mathbf{\Sigma} = \mathrm{diag}(\sigma_1, \sigma_2, \dots, \sigma_r), \tag{3.15}$$

where the columns of $\mathbf{U}$ form an orthonormal basis of temporal modes $\mathbf{u}_k = \{\xi_k(t_m)\}$, the columns of $\mathbf{V}$ form an orthonormal basis of spectral modes $\mathbf{v}_k = \{\phi_k(\omega_n)\}$, and each singular value σ_k quantifies the weight of the corresponding mode pair. This is directly analogous to a Schmidt decomposition: the joint time–frequency structure is expressed as a sum of separable mode products, and the singular values indicate how much energy resides in each pair. Normalizing the weights as $p_k = \sigma_k / \sum_j \sigma_j$ (so that $\sum_k p_k = 1$) allows for the definition of an effective mode count, the chronocyclic Schmidt number,

$$K_{\mathrm{C}} = \frac{1}{\sum_k p_k^2} = \frac{\left(\sum_k \sigma_k\right)^2}{\sum_k \sigma_k^2}, \quad 1 \le K_{\mathrm{C}} \le r. \tag{3.16}$$

A value $K_{\mathrm{C}} = 1$ (only one non-zero σ_k) signifies a fully separable, transform-limited pulse occupying a single spectro-temporal mode, whereas $K_{\mathrm{C}} \gg 1$ points to a strongly multimode field with rich time–frequency correlations.

The SVD representation can be verified to be a faithful representation of the Wigner function by verifying that all three properties stipulated above also hold. First, it is normalized by construction. Next, for the inner product property, for two fields E_1, E_2 with normalized Wigner matrices $\mathbf{W}^{(1)}$ and $\mathbf{W}^{(2)}$, the continuous overlap becomes, using a discretized equivalent to (3.7),

$$\mathcal{I} = \Delta t\, \Delta\omega\, \mathrm{Tr}\left[\mathbf{W}^{(1)} \mathbf{W}^{(2)\top}\right]. \tag{3.17}$$

Performing an SVD on each matrix, $\mathbf{W}^{(k)} = \mathbf{U}^{(k)}\mathbf{\Sigma}^{(k)}\mathbf{V}^{(k)\top}$, the trace reduces to a weighted inner product of their singular spectra:

$$\mathcal{I} = \Delta t\,\Delta\omega\ \sum_j \sigma_j^{(1)}\sigma_j^{(2)}\Big(\mathbf{u}_j^{(1)}\cdot\mathbf{u}_j^{(2)}\Big)\Big(\mathbf{v}_j^{(1)}\cdot\mathbf{v}_j^{(2)}\Big). \tag{3.18}$$

Hence the familiar overlap of two optical fields translates into the pairwise overlap of their temporal and spectral Schmidt modes weighted by the singular values. When the two fields are identical, the trace collapses to $\sum_k \sigma_k^2$, the denominator that appears in the definition of K_{C}.

Finally, for the projection property, because each Schmidt term in the SVD is a separable outer product as observed in the explicit form of (3.15),

$$\mathbf{W}_{mn} = \sum_k \sigma_k\,\xi_k(t_m)\,\phi_k(\omega_n), \tag{3.19}$$

its projection is simply a sum of outer-product projections,

$$P_{a,b}(\chi) = \sum_k \sigma_k \Big[\int \xi_k(t)\,\delta(\chi - at - b\omega)\,dt\Big]\Big[\int \phi_k(\omega)\,d\omega\Big], \tag{3.20}$$

or an equivalent expression if one integrates first over ω. Thus each Schmidt pair contributes independently to any Radon slice, and the full projection is a weighted superposition of one-dimensional quadrature intensities of the individual modes. In practice this means that a single-mode pulse ($K_{\mathrm{C}} = 1$) has projections given by the intensity of one underlying mode; measuring a sufficient set of quadratures fully specifies the field. On the other hand, for a strongly multimode pulse ($K_{\mathrm{C}} \gg 1$), each measured quadrature projection is simply an incoherent sum of the individual mode intensities; performing full tomographic inversion separates these contributions and returns exactly the same Schmidt weights $\{\sigma_k\}$ that arise from the SVD of the chronocyclic Wigner function.

The SVD formalism provides a concise yet complete algebraic representation of the chronocyclic Wigner picture: its orthonormal modes preserve the Wigner function's normalization, its singular weights capture the inner-product structure, and their incoherent superposition reproduces every physical projection. In this way, the SVD faithfully encodes all the geometrical and probabilistic properties that make the Wigner framework so powerful.

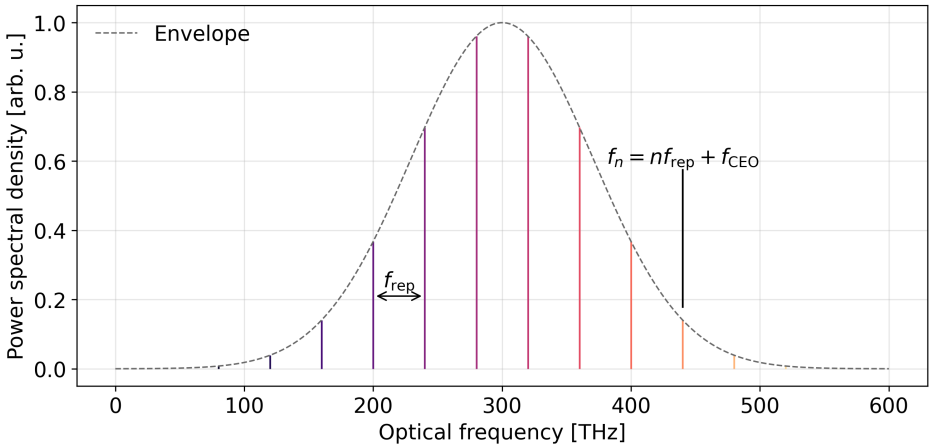

Figure 3.1 Schematic frequency comb. Vertical colored lines represent individual comb teeth spaced by the repetition rate f_{rep}; together they sit under a smooth spectral envelope (dashed). Each tooth satisfies $f_n = nf_{\text{rep}} + f_{\text{CEO}}$, where f_{CEO} is the carrier-offset frequency.

3.2 Numerical Validation on Simulated Frequency Combs

An optical frequency comb is a spectrum of evenly spaced, phase-locked lines (Figure 3.1); an optical ruler in frequency space [61]. Because their lines are phase-coherent over broad bandwidths, frequency combs underpin recent advances in [62]: optical clocks, precision spectroscopy, distance metrology, and coherent waveform synthesis applications, where controlling both the pulse-repetition rate f_{rep} and the Carrier–Envelope Offset (CEO) frequency f_{CEO} is essential. The most common way to generate such a comb is to operate a laser in the mode-locked regime. Instead of lasing at a single resonance, a mode-locked cavity supports many longitudinal modes whose phases are locked, producing a train of pulses in the time domain and, correspondingly, a comb of narrow lines in the frequency domain. As illustrated in Figure 3.1, the spacing of the lines equals f_{rep}, and their centers are displaced from exact harmonics by f_{CEO}. Denoting the slowly varying spectral envelope by $\tilde{A}(\omega)$, the complex field of an ideal, fully stabilized comb can be written as

$$\tilde{E}(\omega) = \tilde{A}(\omega) \sum_{n=-\infty}^{\infty} \delta\big(\omega - 2\pi f_n\big), \qquad f_n = nf_{\text{rep}} + f_{\text{CEO}}. \tag{3.21}$$

When the spectrum carries no more than a constant and a linear spectral-phase term $\phi(\omega) = \phi_0 + (\omega - \omega_0)\tau$ (the constant ϕ_0 sets the carrier-envelope offset and the slope τ gives a global time delay), the field is transform-limited. In this case every round-trip pulse has the same temporal shape, the time–bandwidth product is minimal, and the optical field factorizes into a single temporal waveform multiplied by a periodic comb of carrier cycles. If the

Wigner/SVD formalism is valid, the chronocyclic Wigner distribution should be separable, and its SVD should return one non-zero singular value, such that the chronocyclic Schmidt number $K_{\mathrm{C}} = 1$, confirming a single spectro-temporal mode.

Adding higher-order spectral phase, like group-delay dispersion, third-order dispersion, self-phase modulation, etc. should break this factorability. Energy should be redistributed among orthogonal pairs of temporal and spectral modes, leading to additional singular values appearing and K_{C} rising above unity. Similarly, if the carrier-envelope offset ϕ_0 jitters from pulse to pulse (rather than remaining constant), the pulse train is no longer identical shot-to-shot and the field again becomes multimode, which should push $K_{\mathrm{C}} > 1$.

Table 3.1 Pseudocode for synthesizing a model optical frequency comb. The routine defines the comb parameters (repetition rate, CEO offset, envelope widths, total 2π phase wraps, and desired dispersion orders), builds the list of tooth centers with per-tooth spectral phase, and sums Gaussian lines under a Gaussian envelope to produce the complex spectrum $\tilde{E}(\omega)$.

=== Comb parameters ===

define f_{rep}, f_{CEO}, f_{max}, σ_{tooth}, σ_{env}
define n_{wraps} # total 2π phase rotations
define orders = [1, 2, 3 . . .] # dispersion orders to include

---

=== Build frequency grid ===

for n **from** 1 **to floor**$(f_{max}/f_{\mathrm{rep}})$:
  $f_n = n * f_{\mathrm{rep}} + f_{\mathrm{CEO}}$ # center of n^{th} tooth
  $\theta_n = 2\pi * n_{\mathrm{wraps}} * (n - N/2)/N$ # define 1^{st} order phase
  $\phi_n = \Sigma_{\mathrm{order}}(\theta_n)^{\mathrm{order}}$ # add GDD, TOD, . . .

=== Assemble complex spectrum ===

$\tilde{E}(\omega) = \Sigma_n \exp[-(\omega - f_n)^2/(2\sigma^2_{\mathrm{tooth}}) + i\phi_n]$
$\tilde{E}(\omega)\ * = \exp[-(\omega - \omega_0)^2/(2\sigma^2_{\mathrm{env}})]$

To test the Wigner/SVD formalism, model frequency combs are synthesized with amplitude and phase that can be tuned independently. Each comb line is represented by a tooth with a Gaussian of width σ_{tooth} and is multiplied by a broad Gaussian envelope of width σ_{env}. Dispersive phase is introduced by letting the per-tooth phase scale as an integer power of a base "ramp" $\theta_n \propto n$. The ramp itself sets the total number of 2π phase wraps across the spectrum. The CEO is included as a uniform frequency shift. The procedure is captured in the pseudocode displayed in Table 3.1.

The resulting pair $(\omega, \tilde{E}(\omega))$ is passed to the chronocyclic-Wigner pipeline. By sweeping f_{CEO}, the number of wraps, and the highest dispersion order, the effect of each parameter on the spectro-temporal purity is quantified, expressed through the chronocyclic Schmidt number K_{C}.

The synthetic combs are calculated on a 2^8-point frequency grid. Each spectrum is centered at 300 THz ($\approx$ 1000 nm) and apodized with a 100 THz full-width-at-half-maximum Gaussian envelope. Individual teeth are spaced by 40 THz, orders of magnitude larger than the 1 GHz typical of real combs, but sufficiently coarse to keep the simulation computationally tractable while still sufficiently sampling adjacent lines on this grid. Every tooth is given a Gaussian line-width of 10 GHz.

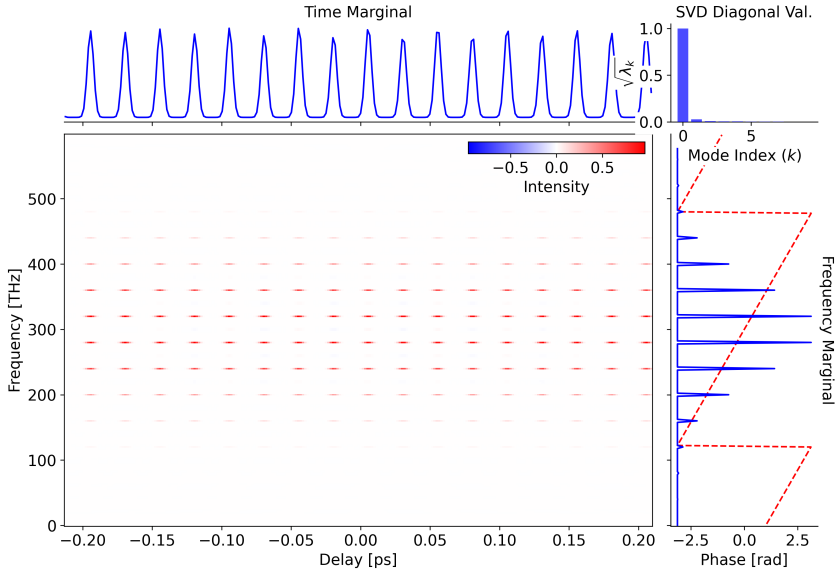

Figure 3.2 Simulated comb with a purely linear spectral phase. Main panel: chronocyclic Wigner distribution shows a periodic lattice of identical pulses; time marginal (top) confirms equal-shape pulses repeating at 25 fs, and frequency marginal (right, blue) lies under the imposed phase ramp (red dashed). The SVD bar-plot reveals a single dominant singular value, giving $K_{\mathrm{C}} \simeq 1$, consistent with a single spectro-temporal mode.

Figure 3.2 shows the result when a linear spectral phase of $\approx$ 10.5 rad is applied across the comb. In the time domain this produces a train of identical pulses repeating every 1/40 THz $\approx$ 25 fs; the envelope of each pulse retains the transform-limited width ($\approx$ 10 fs FWHM) because a pure linear phase merely shifts the waveform in time. The chronocyclic Schmidt number retrieved from the discretized Wigner–SVD analysis is $K_{\mathrm{C}} = 1.002$, the slight excess above unity arising from numerical round-off and finite grid size. This value,

and the identical result obtained when no phase is applied, confirms that first-order (linear) spectral phase leaves the comb in a single spectro-temporal mode, exactly as expected.

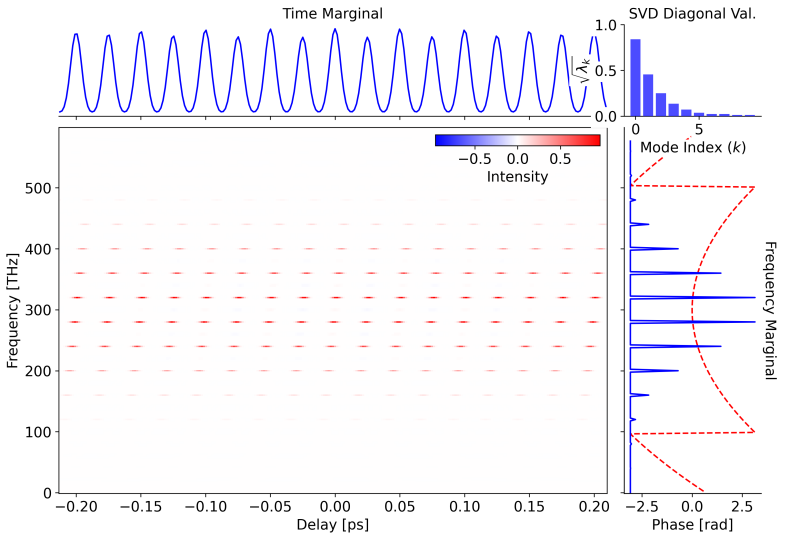

Figure 3.3 Frequency-comb response to quadratic spectral phase (GVD). A 7 rad second-order phase broadens each pulse (top trace) and shears the Wigner lattice (centre). Multiple SVD singular values appear (right), giving $K_C \approx 1.84$, while the red dashed curve shows the imposed parabolic phase across the comb teeth.

The other two frequency dependent dispersive terms that most strongly shape ultrafast pulses are GVD (a quadratic spectral phase) and TOD (a cubic spectral phase). Figures 3.3 and 3.4 illustrate their impact on the same model comb after applying total phase swings of 7 rad (GVD) and 36.5 rad (TOD), respectively. As expected, the quadratic phase stretches each pulse in the train, lowering its peak power and producing a smooth, chirped time–frequency tilt; in the chronocyclic Wigner map this appears as a linear shear of the off-diagonal lobes. By contrast, the cubic phase introduces wavelength-dependent group delay curvature: the central comb lines are delayed relative to the wings, generating asymmetric satellite pulses on either side of the main peak. The corresponding Wigner distribution shows a characteristic "C-bend", and because opposing frequency components interfere out of phase, regions of negative amplitude, a hallmark of non-Gaussian structure and a direct signature of TOD-induced temporal interference. Both patterns match the textbook Wigner functions of Gaussian pulses carrying pure quadratic or cubic phases [63].

Figure 3.5 compares how the chronocyclic Schmidt number K_C grows with phase swing for dispersion orders 1–5. A clear pattern emerges: even orders (2, 4, ...) drive K_C up more rapidly than the neighboring odd orders (1, 3, 5). The trend is not a trivial consequence of

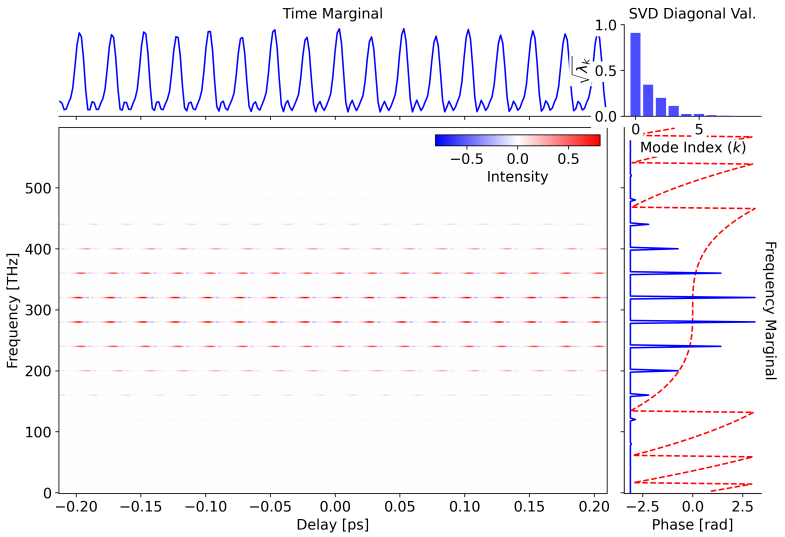

Figure 3.4 Frequency-comb response to cubic spectral phase (TOD). Applying a 36.5 rad third-order phase generates asymmetric satellite structure in each pulse (top trace) and produces an "C-shaped" Wigner lattice with alternating negative lobes (centre). The broader singular-value spectrum on the right corresponds to $K_{\mathrm{C}} \approx 1.43$. The dashed red curve shows the imposed cubic phase across the comb teeth.

the scaling of the phase coefficients with bandwidth since the fourth-order curve lies above the third-order one even though its coefficient is almost an order of magnitude smaller. A deeper symmetry argument is required.

For a comb whose amplitude envelope $\tilde{A}(\omega)$ is symmetric about its center frequency ω_0, the first non-vanishing contribution to broadening the pulse width characterized here by the Root Mean Square (RMS) pulse width $\langle t^2 \rangle$ comes from the mean-square group delay $[\phi'(\omega)]^2$ (see derivation in Annex A),

$$\langle t^2 \rangle \propto \int |\tilde{A}(\omega)|^2 \, [\phi'(\omega)]^2 \, d\omega \tag{3.22}$$

because the odd moment of $\phi' \propto (\omega - \omega_0)$ integrate to zero. Even-order dispersion adds terms proportional to $(\omega - \omega_0)^{2m}$ whose square survives the integral and increases $\langle \tau^2 \rangle$ directly, spreading energy over a wider delay range and populating additional Schmidt pairs. Odd-order dispersion, by contrast, produces an antisymmetric $\phi'(\omega)$ whose positive and negative slopes largely cancel in $[\phi'(\omega)]^2$; its main effect is to skew or split each pulse, but without the same net broadening. In the Wigner picture, even-order terms impose a monotonic shear that decorrelates time and frequency over the entire comb, whereas odd-order terms fold the lattice in opposite directions on either side of ω_0, creating local interference that only

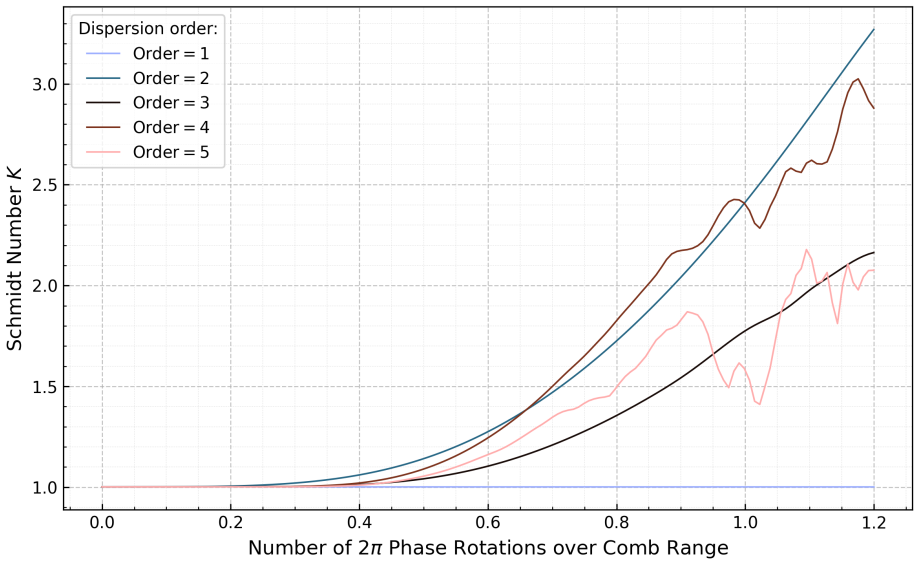

Figure 3.5 Spectro-temporal purity versus applied phase. Schmidt number K of a simulated frequency comb as a function of the total spectral-phase swing (expressed in multiples of 2π) for successive dispersion orders. First-order (constant group delay) leaves the comb single-mode ($K = 1$), whereas higher-order dispersion gradually increases multimodeness; fourth- and fifth-order terms introduce irregular oscillations because of multiple stationary-phase points across the spectrum.

modestly increases the overall mode count. The result is the systematic hierarchy seen in the figure: for a fixed phase excursion, even powers contribute more strongly to multimodeness than odd powers.

Before closing the numerical survey of frequency combs, the effect of SPM is examined [64]. This mechanism is the nonlinear workhorse for spectral broadening in mode-locked lasers [65] and frequency-comb generators [66]. Directly modeling SPM in a comb requires solving the nonlinear Schrödinger equation for thousands of teeth, but the essential physics can be captured with a single Gaussian pulse. Figure 3.6 shows the chronocyclic Wigner map after imprinting a cosine-shaped instantaneous phase of $9 * |E(t)|^2$.

Several SPM signatures are evident. In time, the Wigner distribution follows the applied phase, producing the characteristic "S" pattern: red-shifted components appear on the leading edge while blue-shifted components accumulate on the trailing edge. The temporal intensity (top panel) is no longer symmetric, the front half of the pulse stretches while the back half compresses. In frequency (right panel) the spectrum broadens and develops multiple lobes, mirroring the well-known SPM "splitting" measured in experiments. These new lobes correspond to additional orthogonal Schmidt pairs; the singular-value histogram confirms a

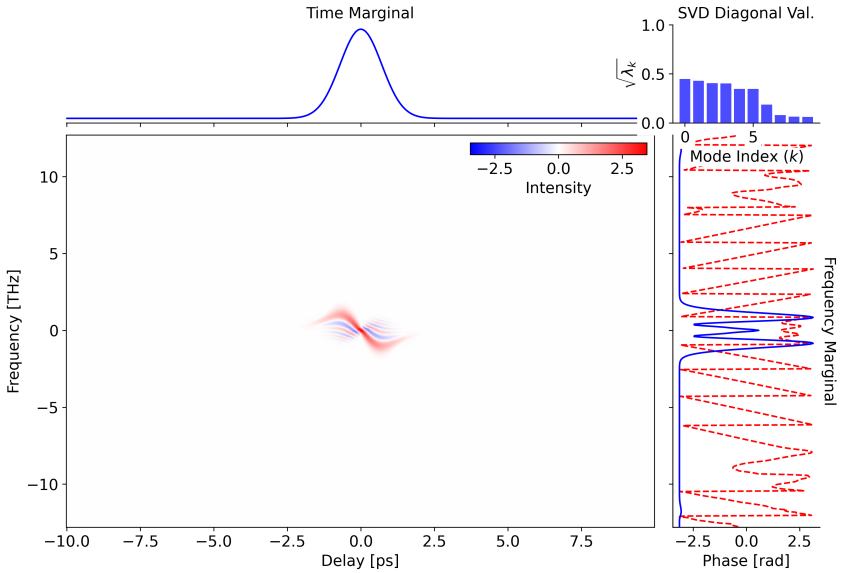

Figure 3.6 Gaussian pulse after self-phase modulation (SPM). A transform-limited Gaussian is subjected to strong instantaneous self-phase modulation, yielding a broadened, chirped time marginal (top) and an "S-shaped" chronocyclic Wigner distribution (center) that reflects the symmetric up- and down-frequency sweep across the pulse. The imposed nonlinear phase (right, dashed) drives energy into multiple spectro-temporal Schmidt pairs; the SVD spectrum reveals numerous significant singular values, with $K_C \gg 1$.

substantial increase in multimodeness, with $K_C \simeq 6.4$.

For an actual frequency comb, SPM applied in a highly nonlinear fiber or photonic chip would act on every pulse in the train, replicating this broaden-and-split behavior for each tooth and pushing the comb's overall Schmidt number up by the same mechanism. Thus, while SPM is invaluable for creating octave-spanning combs, it inevitably multiplies the number of occupied spectro-temporal modes unless balanced with another non-linear process.

In this work, the chronocyclic Wigner function is used as a classical pre-diagnostic of the time–frequency mode structure. A desideratum when applied to experimentally retrieved pulses (Section 3.3) is that it be deliberately "boring": its SVD should ideally yield a single, separable lobe at the Fourier limit (no tilt/shear, no interference fringes), i.e. one spectro-temporal mode. Unlike the quantum Wigner function, where negativity or squeezing indicate nonclassical resources, the chronocyclic Wigner function is not a nonclassicality witness; rather, as discussed in Section 3.4, here it serves to flag features that can degrade the single-mode character of the eventual quantum output. That said, it has the potential to reveal nontrivial classical structure such as sub-Planckian lattices from multi-pulse or

phase-structured fields [67].

3.3 Experimental Retrieval

Recovering a full chronocyclic Wigner distribution from an experimental frequency comb demands knowledge of the complex electric field $E(t) = |E(t)|e^{i\phi_t(t)}$; that is, both the slowly varying envelope and the rapidly oscillating carrier. In principle one must measure the CEO phase that shifts every comb tooth by f_{CEO}; doing so requires an f–$2f$ interferometer or similar CEO-locking schemes [68, 69]. These types of measurement setups can be quite complex to implement.

Fortunately, the CW Schmidt number is insensitive to an overall carrier phase: it depends only on the envelope and on relative spectral phase variations. Hence a practical approximation is to reconstruct those two quantities on a shot-to-shot basis and ignore the unknown global CEO shift. Second Harmonic Generation Frequency-Resolved Optical Gating (SHG-FROG) provides exactly the required information [57]. A single SHG-FROG trace yields both the spectral amplitude $|\tilde{E}(\omega)|$ (i.e. the comb envelope) and the spectral phase $\phi_\omega(\omega)$ or, equivalently, the time-domain envelope and instantaneous phase. From these, one can compute an accurate Wigner function modulo the constant CEO term and extract K_{C} with good fidelity, sidestepping the need for full CEO measurement while still capturing the spectro-temporal mode structure of the pulses.

SHG-FROG is a self-gating technique: the pulse under test serves as both the probe and the gate in a $\chi^{(2)}$ (sum-frequency) interaction. When two replicas of the pulse overlap in a nonlinear crystal with a relative delay τ, the crystal emits the waveform

$$E_{\mathrm{SHG}}(t, \tau) \propto E(t)\, E(t - \tau), \tag{3.23}$$

and the spectrometer records its intensity spectrum $|\mathcal{F}\{E(t)E(t-\tau)\}|^2$. Sweeping τ across the pulse duration yields a two-dimensional trace, the SHG-FROG spectrogram, that is mathematically the Fourier transform of the gated field versus delay. Because the same pulse gates itself, the trace is symmetric in τ, which introduces a trivial time-reversal ambiguity; in practice this is resolved by empirically estimating the phase sign or adding known dispersion in the system. Compared with third-order FROG variants (e.g. transient-grating or self-diffraction FROG), the χ^2 process offers far higher conversion efficiency, so SHG-FROG remains sensitive at lower pulse energies.

Figure 3.7 shows the built in-house SHG-FROG system, which can characterize pulses at both 1560 nm and their frequency-doubled counterparts at 780 nm. Broadband, low-GDD

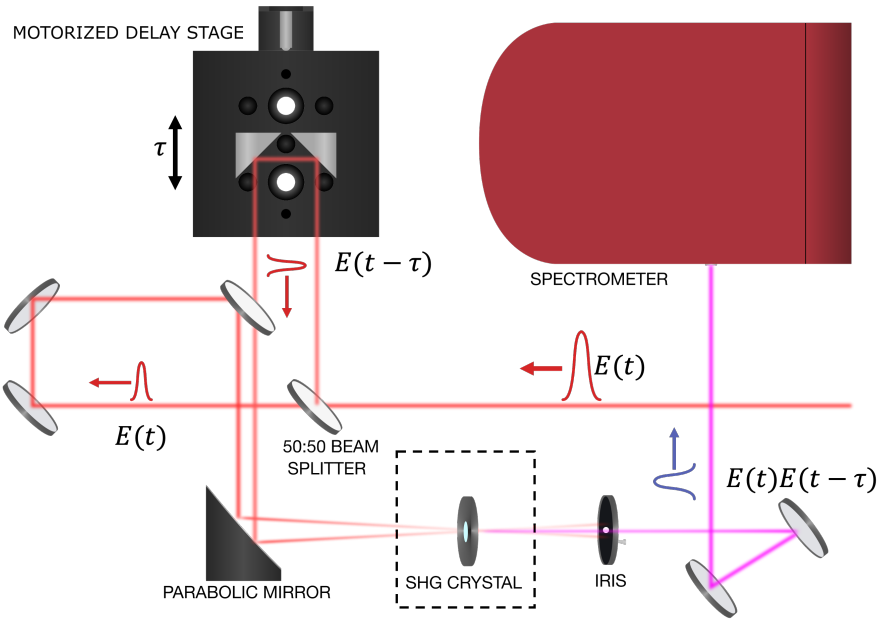

Figure 3.7 Second-harmonic FROG setup. A beam splitter splits the input pulse into a respective fixed delay and a variable-delay Michelson arm; the two replicas are recombined and focused non-collinearly into a thin nonlinear crystal, where they generate a second-harmonic signal (magenta). The up-converted light is focused in a spectrometer with a concave mirror and the signal recorded, producing a wavelength-resolved intensity versus delay FROG trace from which the pulse's amplitude and phase are retrieved.

silver mirrors and beam-spliters steer the beam to a removable thin-film BBO crystal; swapping between two angle-polished crystals, one phase-matched for Sum-Frequency Generation (SFG) at 1560 nm, the other for 780 nm, lets the same optics train serve either wavelength. Downstream optics and detectors are changed as a set: silver mirrors and a Thorlabs CCD spectrometer for the C-band, aluminium mirrors and a Qe65 spectrometer for the visible. Temporal alignment into the non-linear crystal can be simplified by using a camera that is nominally blind at the pump wavelength (e.g. a CMOS camera for 1560 nm). At sufficient intensity, the sensor exhibits two-photon absorption, producing a bright intensity spike only when the two replicas are spatially co-focused and temporally overlapped. Final pulse reconstruction from the recorded spectrograms is carried out with the Common Pulse Retrieval Algorithm (COPRA) [70]. The system was validated at each wavelength on a commercial mode-locked laser system with a known pulse width.

3.4 Bridging Chronocyclic and Biphoton Schmidt Numbers

In the section that follows, the pump-centric chronocyclic intuition developed above is translated into the language of biphoton entanglement. Readers versed in quantum optics will recognize that the SVD applied to the chronocyclic Wigner function is mathematically identical to the Schmidt decomposition used for SPDC biphoton states. Starting from the spectral Schmidt expansion of the Joint Spectral Amplitude (JSA) (Section 3.4.1), the chronocyclic Schmidt number K_{C} is retrieved from the total biphoton Schmidt number K_Q (Section 3.4.2). The take away is a compact design rule: by tailoring the pump envelope and phase-matching function so that K_{C} approaches unity, one simultaneously drives K_Q toward one, thereby suppressing both spectral and temporal correlations.

3.4.1 Biphoton Schmidt Number

A central design requirement for the bright-pair source is that the generated biphoton state be spectrally uncorrelated, i.e. factorable in the signal and idler frequencies. Spectral correlations are fully encoded in the Joint Spectral Amplitude (JSA) $f(\omega_s, \omega_i)$, which appears in the two-photon component of the SPDC output state. For Type-II, collinear SPDC pumped by an ultrashort pulse, the state can be written (retaining only the single-pair term and omitting the vacuum and higher-order contributions that are negligible in the low-gain regime) as [71]

$$|\Psi\rangle = \iint d\omega_s \, d\omega_i \; f(\omega_s, \omega_i) \, \hat{a}_s^\dagger(\omega_s) \, \hat{a}_i^\dagger(\omega_i) |0, 0\rangle. \tag{3.24}$$

Energy conservation couples the two frequencies through their sum, while phase matching couples them through their difference. Accordingly the JSA factorizes into a product of the pump spectral envelope and the phase-matching function:

$$f(\omega_s, \omega_i) \;\approx\; E_p(\omega_s + \omega_i) \, \Phi(\omega_s, \omega_i). \tag{3.25}$$

To build intuition for the geometry of the JSA, and without affecting the subsequent Schmidt-number argument, the pump spectral envelope is modeled as a Gaussian

$$E_p(\omega_s + \omega_i) = \exp\left[-\frac{(\Omega_s + \Omega_i)^2}{2\sigma_p^2} \right], \tag{3.26}$$

whose full width at half-maximum is $2\sqrt{2\ln 2}\,\sigma_p$. Here $\Omega_j = \omega_j - \omega_{0,j}$ denotes the frequency detuning of mode $j \in \{s, i\}$ from its carrier $\omega_{0,j}$. Because this envelope depends only on the frequency sum, its contours run along $\omega_s + \omega_i = \text{const}$; in the (ω_s, ω_i) plane it therefore fills

an anti-diagonal stripe (Figure 3.8, left).

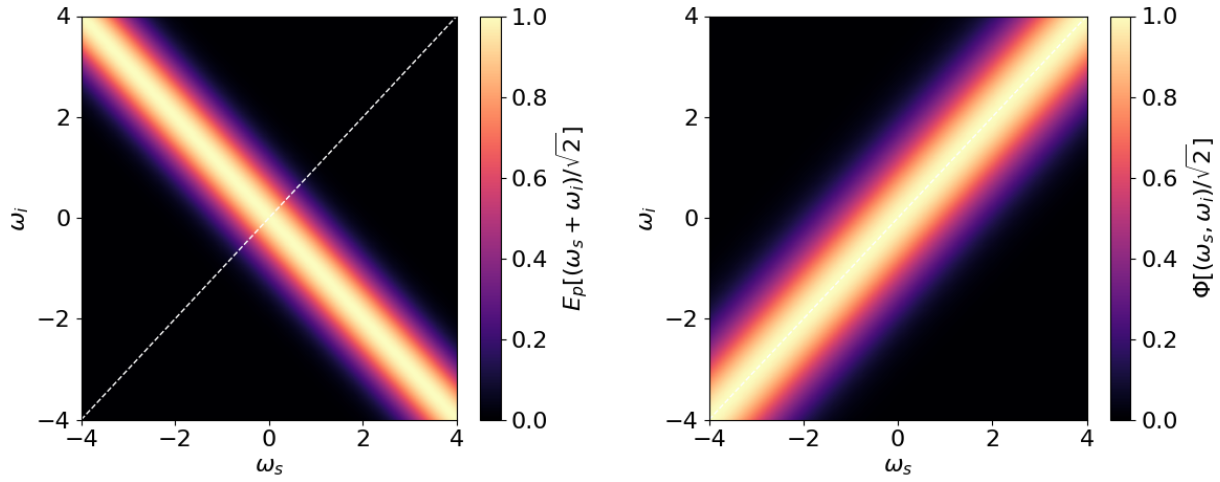

Figure 3.8 Left: Gaussian pump spectral envelope $E_p[(\omega_s + \omega_i)/\sqrt{2}]$ plotted in the (ω_s, ω_i) plane. Because it depends only on the frequency sum, the high-intensity region forms an anti-diagonal stripe (slope -1); the white dashed line marks the $\omega_s = \omega_i$ diagonal for reference. Right: Gaussian phase-matching function $\Phi[(\omega_s - \omega_i)/\sqrt{2}]$. Here the intensity ridge lies along the main diagonal (slope $+1$), reflecting its dependence on the signal–idler detuning. Under symmetric group-velocity matching these two envelopes are orthogonal, a prerequisite for engineering a factorable joint spectral amplitude.

The Phase Matching Function (PMF) for a bulk $\chi^{(2)}$ crystal of length L is, in general [72],

$$\Phi(\omega_s, \omega_i) = \int_0^L dz\, P(z)\, e^{i\Delta k(\omega_s,\omega_i)z}, \tag{3.27}$$

where $\Delta k = k_p(\omega_s + \omega_i) - k_i(\omega_i) - k_s(\omega_s)$ is the phase mismatch, $k_j(\omega) = \omega n_j(\omega)/c$ is the wavenumber, and $P(z) = \chi^{(2)}(z)/\chi_0^{(2)}$ is the normalized nonlinear profile. Under typical approximations this integral reduces to a sinc function as in Section 4.3; for analytic simplicity it is replaced here with an equivalent Gaussian, a choice that also does not alter the subsequent Schmidt-number argument.

Expanding each wavenumber to first order about its carrier, $k_j(\omega) = k_j(\omega_{0,j}) + v_j^{-1}\Omega_j$, where $v_j^{-1} = (d\omega/dk_j)_{\omega_{0,j}}$ is the inverse group velocity, the mismatch becomes

$$\Delta k = \Delta k_0 + (v_p^{-1} - v_i^{-1})\Omega_i + (v_p^{-1} - v_s^{-1})\Omega_s, \tag{3.28}$$

with $\Delta k_0 = k_p(\omega_{0,s} + \omega_{0,i}) - k_s(\omega_{0,s}) - k_i(\omega_{0,i})$. The difference between the group velocities

sets the angle θ between the PMF and the pump envelope:

$$\tan\theta = -\frac{v_p^{-1} - v_s^{-1}}{v_p^{-1} - v_i^{-1}}. \tag{3.29}$$

Engineering the crystal so that it satisfies the symmetric group-velocity-matching condition $v_p^{-1} = v_s^{-1} + v_i^{-1}$ forces $\theta = 90°$, i.e. the PMF is perpendicular to the pump stripe. Approximating the PMF by a Gaussian of width σ_{PMF},

$$\Phi(\omega_s, \omega_i) = \exp\left[-\frac{(\Omega_s - \Omega_i)^2}{2\sigma_{\text{PMF}}^2}\right], \tag{3.30}$$

one obtains the diagonal ridge plotted in Figure 3.8 (right). This orthogonality between the anti-diagonal pump envelope and the diagonal PMF underpins the later separation of pump and crystal contributions in the Schmidt decomposition and, ultimately, the design of spectrally uncorrelated (factorable) biphoton states.

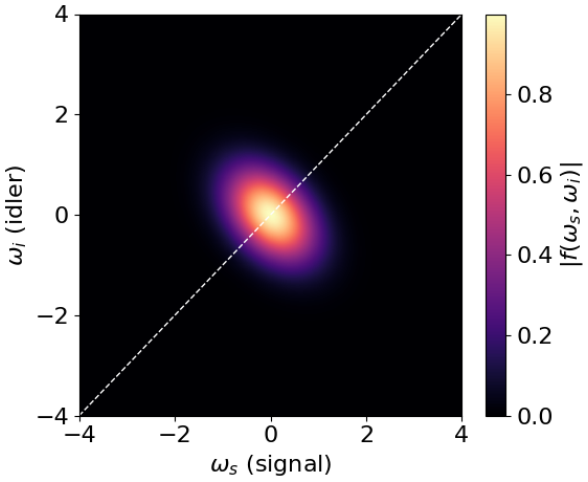

Figure 3.9 Simulated joint spectral amplitude $|f(\omega_s, \omega_i)|$. The elliptical, slightly tilted blob indicates residual signal-idler frequency correlations; perfect factorability would appear as a circular spot aligned with the axes. The dashed white line marks the $\omega_s = \omega_i$ diagonal.

Overlaying the two envelopes in Figure 3.8 and multiplying them point-wise produces the JSA plotted in Figure 3.9. The resulting map is an ellipse (under the double Gaussian approximation) whose tilt (set by the group-velocity mismatch) and eccentricity (set by the relative bandwidths) quantify the residual frequency-frequency correlations: the more elongated or tilted the ellipse, the larger the spectral entanglement. Richer pump spectra or non-Gaussian phase-matching profiles generate intricate JSA maps whose shape also characterize spectral

entanglement. The most common way to turn the JSA representation into a number to quantify spectral entanglement is the Schmidt (singular-value) decomposition [73, 74]

$$f(\omega_s, \omega_i) = \sum_k \sqrt{\lambda_k}\; u_k(\omega_s)\, v_k(\omega_i), \tag{3.31}$$

where the orthonormal mode functions $\{u_k\}$ and $\{v_k\}$ live, respectively, in the signal and idler Hilbert spaces and the non-negative coefficients $\{\lambda_k\}$ satisfy $\sum_k \lambda_k = 1$. The Schmidt coefficients themselves fold into the entanglement metric called here the biphoton Schmidt number

$$K_Q = \frac{1}{\sum_k \lambda_k^2}, \tag{3.32}$$

which ranges from $K_Q = 1$ for a perfectly factorable (spectrally uncorrelated) state to $K_Q \gg 1$ for highly entangled pairs. Operationally, $1/K_Q$ equals the spectral purity of a heralded single photon, so driving K_Q toward unity is tantamount to engineering near-transform-limited, high-purity heralds. Substituting the expansion (3.31) back into the state integral ((3.24)) factorizes the biphoton state itself,

$$|\Psi\rangle = \sum_k \sqrt{\lambda_k}\, |u_k\rangle_s \otimes |v_k\rangle_i \quad , \quad |u_k\rangle_s = \int d\omega\; u_k(\omega)|\omega\rangle_s \quad , \quad |v_k\rangle_i = \int d\omega\; v_k(\omega)|\omega\rangle_i \tag{3.33}$$

making it clear that only one non-zero Schmidt coefficient ($\lambda_0 = 1$) guarantees a spectrally factorable pair. The same coefficients control the joint temporal amplitude, the double Fourier transform of the JSA, so spectral and temporal entanglement are two sides of the same coin.

3.4.2 Chronocyclic Schmidt Number Extraction

To cleanly separate pump-related and crystal-related contributions hidden inside K_Q, start by rotating the signal–idler frequency plane into the orthogonal sum–difference coordinates

$$\Sigma = \frac{\omega_s + \omega_i}{\sqrt{2}}, \qquad \Delta = \frac{\omega_s - \omega_i}{\sqrt{2}}. \tag{3.34}$$

In these new coordinates, the rotated JSA shown in Figure 3.10 can be written as

$$f(\Sigma, \Delta) = E_{\mathrm{p}}(\sqrt{2}\,\Sigma)\; \Phi(\Sigma, \Delta). \tag{3.35}$$

For a sufficiently short crystal engineered to satisfy symmetric group-velocity matching, the

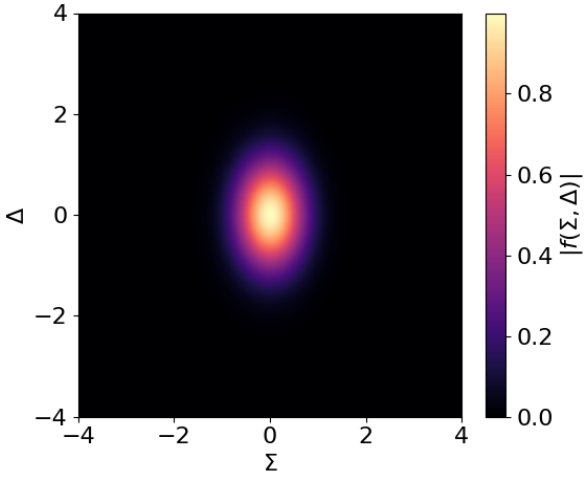

Figure 3.10 Simulated joint spectral amplitude $|f(\Sigma, \Delta)|$ generated by the pump function and PMF plotted in Figure 3.8 after rotation into the sum–difference basis (Σ, Δ). The near-circular spot, elongated only along Δ, highlights how pump bandwidth and phase-matching width decouple, making the JSA close to a separable product of independent Σ and Δ envelopes.

phase-matching envelope is essentially flat along the sum-frequency axis Σ while remaining tightly confined in the detuning coordinate Δ. In the (Σ, Δ) frame this appears as a narrow, nearly vertical ridge (the diagonal in the (ω_s, ω_i) plane as seen on the right in Figure 3.8), allowing the envelope to be treated as effectively one-dimensional:

$$\Phi(\Sigma, \Delta) \simeq \phi_0 \, \phi(\Delta), \tag{3.36}$$

with the constant ϕ_0 absorbing the residual, weak dependence on Σ. Hence the JSA factorizes into approximately separable Σ and Δ dependent terms along the rotated axes,

$$f(\Sigma, \Delta) \simeq g(\Sigma) \, h(\Delta), \qquad g(\Sigma) = \phi_0 E_{\mathrm{p}}(\sqrt{2}\,\Sigma). \tag{3.37}$$

Moving to a matrix representation, the JSA is discretized by sampling Σ on M points $\{\Sigma_m\}_{m=1}^{M}$ and Δ on N points $\{\Delta_n\}_{n=1}^{N}$,

$$F_{mn} = g_m \, h_n \quad \Longrightarrow \quad \mathbf{F} = g \otimes h^{\mathsf{T}}, \tag{3.38}$$

where $g \in \mathbb{C}^M$ and $h \in \mathbb{C}^N$ are column vectors and $\otimes$ denotes the outer (Kronecker) product. When both the pump envelope and the phase-matching function are engineered such that

the overall biphoton Schmidt number K_Q approaches unity, the discretized JSA matrix $\mathbf{F}$ is effectively rank-one. Its singular-value decomposition therefore reduces to

$$\mathbf{F} = \|g\| \, \|h\| \frac{g}{\|g\|} \frac{h^*}{\|h\|}, \tag{3.39}$$

with a single, non-zero singular value $\sigma_1 = \|g\| \, \|h\|$. In practice, however, the pump spectrum E_{p} can contain weak subsidiary modes and the PMF may not be perfectly separable. Their individual SVD spectra then contain multiple, but still rapidly decaying coefficients, denoted $\{a_k\}_{k=1}^{m}$ for the pump and $\{b_\ell\}_{\ell=1}^{n}$ for the phase matching.

The non-zero singular values of the Kronecker product $\mathbf{F}$ are simply the pairwise products $\{\sigma_{k\ell} = a_k b_\ell\}$. Defining the normalized weights

$$p_{k\ell} = \frac{\sigma_{k\ell}}{\sum_{i,j} \sigma_{ij}} = \frac{a_k b_\ell}{\sum_i a_i \sum_j b_j}. \tag{3.40}$$

the biphoton Schmidt number is

$$K_{\mathrm{Q}} = \frac{1}{\sum_{k,\ell} p_{k\ell}^2} = \left(\frac{1}{\sum_k a_k^2}\right)\left(\frac{1}{\sum_\ell b_\ell^2}\right) \equiv K_{\mathrm{C}} \, K_{\Phi}. \tag{3.41}$$

The two sets of singular values lead to two distinct contributions to the overall Schmidt number. The pump–related term, $K_{\mathrm{C}} = (\sum_k a_k^2)^{-1}$, measures the spectro-temporal multimodality of the driving field and is obtained directly from the Wigner–SVD analysis described in this chapter. The crystal-dependent term, $K_\Phi = (\sum_\ell b_\ell^2)^{-1}$, reflects only the shape of the phase-matching envelope and is therefore an intrinsic property of the nonlinear medium.

A natural question is why the Schmidt weights that appear in the biphoton number K_Q are the pump weights already extracted as K_{C}. The answer is that both analysis act on the same single-photon field operator, merely expressed in different bases. The chronocyclic picture treats the pump's Wigner kernel as a Hilbert–Schmidt operator on the time–frequency plane and diagonalizes it; this yields the eigenvalues $\{a_k\}$. In the SPDC picture, the very same pump envelope enters the JSA through the factor $E_p(\omega_s + \omega_i) = g(\Sigma)$. Switching from the Wigner representation to the purely spectral one involves only unitary transformations (Fourier on the delay coordinate and a 45° rotation to Σ); unitary maps preserve singular values. Consequently the SVD of $g(\Sigma)$ carries over unchanged into the Kronecker-product decomposition of the full JSA, so the coefficients $\{a_k\}$ re-emerge verbatim in K_Q. Physically, the pump can introduce no more and no fewer spectro-temporal modes in the pair-generation process than it already contains on its own.

To conclude, if the pump is genuinely single-mode ($K_{\mathrm{C}} = 1$) and the phase-matching function is perfectly separable ($K_{\Phi} = 1$), their product gives $K_Q = 1$; the biphoton state is then fully factorable and heralded photons emerge in a pure spectral mode. A modest quadratic chirp or residual SPM on the pump broadens adds only a few new Schmidt modes, so K_{C} remains close to unity and entanglement is essentially unaffected. By contrast, residual group-velocity mismatch in the crystal increases the width of Φ along the Σ direction, driving $K_{\Phi} > 1$. Even with a single-mode pump this lifts K_Q above one, re-introducing spectral correlations; mitigating strategies include shortening the crystal, adding compensatory pump chirp, or using apodized or chirped poling.

CHAPTER 4 FEMTOSECOND PUMP ENGINEERING

This chapter details the development of the pump source that drives the SPDC stage. It opens with the design and characterization of a custom, mode-locked femtosecond fiber laser operating in the telecom C-band. The laser is configured to operate in its second-order mode locking regime and delivers 1560 nm pulses at 228.7 mW average power and a 121.6 MHz repetition rate.

Next is described the free-space pulse-compression and Second Harmonic Generation (SHG) systems: the compressor shortens the pulse duration from 359.4 fs to 109.6 fs, after which a periodically poled waveguide doubles the frequency with 45.6 % conversion efficiency, yielding a 780 nm pump to drive SPDC with 91.11 mW average power and an 101.6 fs pulse width.

The chapter concludes by applying the chronocyclic-Wigner–based framework developed in section 3.1 for assessing temporal-mode purity of the emitted pulses. Using this approach, chronocyclic Schmidt numbers of $K_{\mathrm{C}} = 1.64$ for the fundamental beam and $K_{\mathrm{C}} = 1.18$ for its frequency-doubled counterpart are obtained.

4.1 Near Infrared Femtosecond Mode-Locked Amplified Fiber Laser

The choice of a mode-locked laser to seed the rest of system is essentially conditioned by the objective of the project. As outlined in section, to generate photon pairs confined to a single spectral mode, the seed itself must be in a single temporal mode (assuming proper phase matching in the non-linear media). This is the reciprocal of having photon pairs generated in a single temporal mode by an ideal CW seed in a single spectral mode. In the frequency comb picture, a mode-locked laser is the dual of a CW laser, where coherent oscillation of the longitudinal modes in the laser cavity confines the energy in a single temporal mode, that is, a pulse train where each pulse is in an identical mode. This is not inherent to other pulsed laser sources, such as Q-switching or external modulation, where the longitudinal modes of the cavity do not intrinsically feature a fixed phase relationship and therefore cannot readily deliver the single-mode quality needed to seed the rest of the system.

Mode-locking, and its optical fiber based implementation described in this work, also offers three decisive practical advantages for this source. First, it produces sub-picosecond pulses with peak powers several orders of magnitude higher than that attainable with Q-switching or gain-switched diodes. These high peak powers significantly boost the efficiency of $\chi^{(2)}$ interactions [75, 76], which is critical for efficient SHG [77], or entering the high-gain regime

of SPDC, where bright twin beams containing millions of photon pairs can be generated per pulse [44, 78]. Second, the hermetic fiber geometry also passively suppresses air currents and temperature drifts, yielding reduced timing jitter and relative-intensity noise figures, which must be low enough to preserve the quantum correlations of the generated photon pairs. Last but not least, it locks all frequency modes in phase, resulting in principle in a single mode in the time domain.

A fully fiber-integrated architecture also sets out a clear road-map for future upgrades. Once fiber-induced nonlinear distortions are properly mitigated, the oscillator output can be fusion-spliced directly into pigtailed waveguide chips, allowing both the SHG and SPDC stages to be implemented as compact, alignment-free modules with superior mode confinement and conversion efficiency. Such waveguide converters can deliver Watt-level average powers with single-pass SHG efficiencies exceeding 50% at 780 nm [79], providing an ideal pump for high-gain SPDC.

Finally, operating in the telecom C-band offers several decisive advantages for a bright quantum light source. Fused silica single-mode fibers reach their absolute loss minimum here, with the extremely common SMF-28e+ by Corning quoting losses $\leq 0.18\,\mathrm{dB\,km^{-1}}$ at 1550 nm. Kilometer-scale delivery of the generated photon pairs therefor introduces only negligible attenuation, preserving quantum correlations. The same window also coincides with the stimulated emission band of the ${}^4I_{13/2} \rightarrow^4 I_{15/2}$ transition of Er^{3+}, enabling compact mode-locked oscillators and amplifiers that routinely provide $>$ 40 dB small-signal gain across the 1530–1565 nm band [80]. Detector technology is equally mature; cooled InGaAs/InP avalanche photodiodes achieve 10–30 % quantum efficiency with low dark-count probabilities at 1550 nm [81], while state-of-the-art superconducting nanowire single-photon detectors now exceed 95 % system detection efficiency and sub-hertz dark-count rates [82]. Together, these factors minimize loss and noise throughout the pump-SHG-SPDC chain, making the C-band a practical and scalable spectral region for generating and characterizing bright entangled photon pairs.

The amplified C-band mode-locked femtosecond laser described below is an adaptation of earlier prototypes developed at Polytechnique Montréal by Laurent Rivard [83] and Alexis Labranche [84], and was fabricated and characterized in collaboration with Colin Dietrich [85].

4.1.1 Design

The fiber laser is organized into two fiber-integrated subsystems, as depicted in Figure 4.1. The Master Oscillator (MO) is a Semiconductor Saturable-Absorber Mirror (SESAM)-based, mode-locked, sigma-shaped cavity, where self-phase modulation balances with anomalous dis-

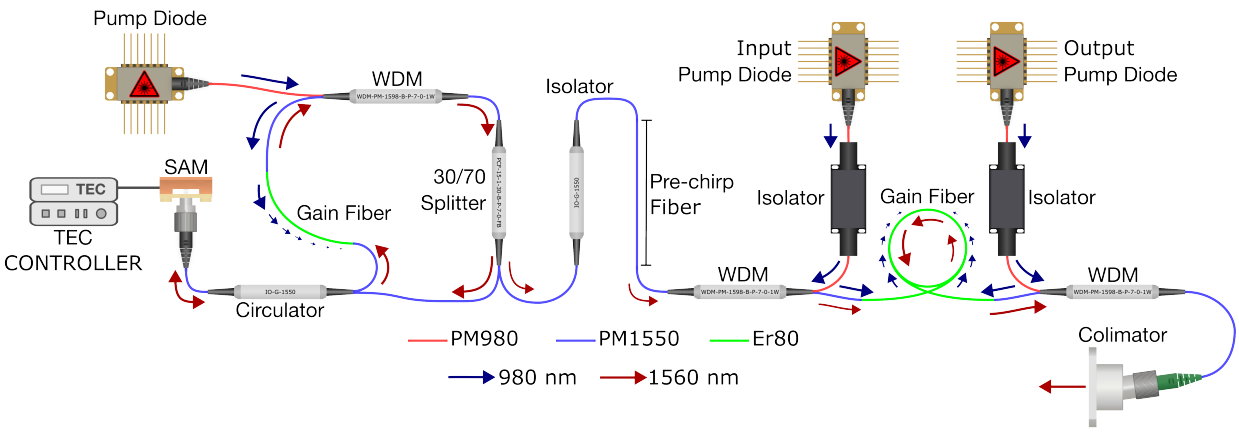

Figure 4.1 Mode-Locked Fiber Laser Layout. Left: 979 nm-pumped, SESAM-mode-locked sigma-shaped oscillator producing 1560 nm pulses. Right: Er-doped fiber amplifier with pre-chirp fiber and counter-propagating 979 nm pumps; amplified pulses exit a fiber collimator. Colour code: red fibers – PM980, blue fibers – PM1550, green fibers – Er80 gain fiber; blue arrows – 979 nm CW pump light, red arrows – 1560 nm signal pulses.

persion to produce femtosecond quasi-soliton pulses. The passive SESAM design confers two advantages: it is self-starting, because its intensity-dependent loss suppresses low-power noise while transmitting the high-power spikes that seed mode-locking, and it enables shorter pulses than are usually achievable with actively modulated schemes. Pulses exit the cavity and enter an Erbium-Doped Fiber Amplifier (EDFA) where, after a short pre-chirp, travel through an Er-doped gain section with normal dispersion. They evolve into parabolic self-similar waveforms, similaritons, another stable solution of the Generalized Nonlinear Schrödinger Equation (GNLSE). The EDFA simultaneously amplifies and compresses the similaritons. The pump and signal fibers (PM980 and PM1550-XP, Thorlabs) and all in-line components are polarization-maintaining, minimizing stress-induced birefringence and delivering high-energy pulses with a well-defined linear polarization, essential for optimal phase matching and conversion efficiency in both the SHG and SPDC stages. All fiber to fiber connections are spliced using a Vytran FFS-2000 system, again to minimize loss and increase stability. The design of each subsystem are detailed below.

In the MO, a current- and temperature-stabilised laser diode driver (CLD1015, Thorlabs) controls a 979 nm fiber Bragg grating-stabilised pump diode (1999CMB, 3SP Technologies). The continuous-wave pump is reflected by a PM 980/1550 nm Wavelength Division Multiplexer (WDM) (WDM-PM-1598-B-P-7-0-1W, AFW) into a 20 cm segment of highly Erbium-doped gain fiber (Er80-4/125-HD-PM, nLight). Because the WDM introduces the pump in the reverse direction, the 979 nm light counter-propagates with respect to the 1560 nm signal,

resulting in a slightly increased relative-intensity noise compared with co-propagating pumping [86], but avoiding the insertion loss of a symmetric coupler. Higher inter-cavity losses results in breakdown of mode-locking at lower output pulse energies. The cavity is closed by a Polarization Maintaining (PM) circulator (6015-3, Thorlabs), which couples the signal to and from the semiconductor SAM (SAM-1550-21-2ps-x, Batop), and a 30/70 tap-coupler (PCF-15-1-30-B-P-7-0-FB, AFW) that extracts 29% of the intracavity power and transmits 65% back into the cavity. An inline isolator (IO-G-1550, Thorlabs) shields the oscillator from back-reflections which could interfere with the mode-locking. The MO is anchored to a 3 cm-thick copper base plate that serves as a thermal reservoir, while the more temperature-sensitive SAM is mounted on a dedicated heat sink coupled to a Peltier module and actively held at 11 °C. This keeps the soliton-formation threshold, central wavelength, and pulse duration stable over extended operation.

Concluding on the design of the MO, the intracavity path consists of the aforementioned 20 cm of highly Er-doped fiber, with a refractive index $n_{\mathrm{Er}} = 1.46$, and ≈ 3.2 m of PM1550 fiber, of $n_{\mathrm{PM}} = 1.449$. Their combined optical length (4.94 m) sets the fundamental repetition rate to $f_{\mathrm{rep}} = c/(nL) = 60.8$ MHz, matching the measured 60.9 MHz. Using the published GVD values for these two fibers $D_{\mathrm{Er}} = +28.4 \times 10^3$ fs^2 m^{-1} and $D_{\mathrm{PM}} = -22.83 \times 10^3$ fs^2 m^{-1}, and adding the SAM's $\approx$500 fs^2 contribution, the net cavity Group Delay Dispersion (GDD) is

$$\mathrm{GDD} = 0.20\,\mathrm{m} \times D_{\mathrm{Er}} + 3.2\,\mathrm{m} \times D_{\mathrm{PM}} + 500\ \mathrm{fs}^2 = -6.69 \times 10^4\ \mathrm{fs}^2. \tag{4.1}$$

The large negative GDD shields the cavity from thermally induced length drifts, yet it also broadens the intracavity pulses, lowers their peak power, and has been shown to heighten timing jitter via the Gordon–Haus mechanism in similar mode-locked fiber laser architectures [87], where quantum-noise-driven frequency fluctuations accumulate non-linearly over successive round trips [88].

The EDFA employs a bidirectionally pumped architecture. A 1.1 m segment of highly Er-doped gain fiber, same as the one used in the master oscillator, is excited by two 979 nm continuous-wave pump diodes (1999CVB, 3SP Technologies), one co-propagating and one counter-propagating with respect to the signal. Each diode is driven by a current- and temperature-stabilized controller (CLD1015, Thorlabs) and can deliver up to 906 mW of optical power. Pump light is injected into the gain fiber via the same PM 980/1550 nm WDMs used in the oscillator, while high-power inline isolators (HPMI-98-01-N-L-Q-F-1-P, AFW) suppress deleterious back-reflections.

A chirped-pulse amplification scheme mitigates nonlinear distortions [89]: the oscillator out-

put first traverses 1.7 m of PM1550 fiber with anomalous dispersion, adding negative GDD that stretches the pulse and lowers its peak power before it reaches the gain fiber. Inside the Er-doped section, the normal dispersion provides positive GDD, partially recompressing the pulse as it is amplified. Downstream of the second WDM, the PM1550 lead is cut to a short 20 cm, just long enough to polish and connectorize it, to avoid re-stretching and additional self-phase modulation or detrimental intrapulse Raman scattering or TOD [84]. Finally, the output fiber is polished in house to an 8° angle, and packaged in an FC/APC connector to minimize Fresnel back reflections. The amplified beam is collimated with an aspheric lens (CM220-TMC, Thorlabs) for free-space propagation toward the pulse compressor and SHG stages.

4.1.2 Performance and characteristics

The performance of the pump laser cascades directly into every downstream stage; pulse compression, second harmonic generation and, ultimately, high-gain SPDC. Four fiber-laser characteristics tightly coupled to the performance of these stages are monitored in detail. First is the power response, both the average output and the per-pulse peak power—which sets the drive level for the χ^2 processes: second-harmonic conversion scales almost quadratically with peak intensity, while SPDC gain rises with average power. Equally important are the spectral and temporal profiles of the pulses. Near 100 fs, transform-limited waveforms maximize the instantaneous intensity and ensure that the pulse spectrum fits cleanly within the quasi-phase matching bandwidth of the non-linear effects used to drive the χ^2 effects; any residual chirp or higher-order spectral phase reduces overlap and lowers conversion efficiency. Finally, the laser's Relative Intensity Noise (RIN) dictates the noise floor in the generated twin beams: amplitude fluctuations at the pump are transferred to the photon-pair flux and ultimately limit heralding efficiency and squeezing measurements. The remainder of the section first measures power scaling, pulse shape, and spectral envelope at the master oscillator output, and then characterizes all four metrics, including the RIN, after the EDFA stage.

Master Oscillator

The two primary knobs that steer the master oscillator are the 979 nm pump-diode power, which sets the gain in the Er-doped fiber, and the SESAM temperature, which affects the intracavity loss. Figure 4.2 maps the MO mean output power versus pump-diode power for the two extreme SAM temperatures available in the setup, 10 °C (blue) and 45 °C (red). The pump diode, rated to 500 mW, launches 979 nm light into the Er-doped fiber; the SESAM, thermo-electrically stabilized between 5 °C and 45 °C, sets the effective loss inside the cavity.

Three distinct operating regimes appear. Below threshold, the intracavity gain in the Er fiber is still lower than the total loss of the cavity, no lasing occurs and the measured output remains at the detector noise floor. Once the stored inversion is high enough to bleach the SAM momentarily, bursts of energy exit the cavity as low-repetition, high-energy spikes. This is the Q-switching regime, and begins at ≈30 mW of absorbed pump power for the cold SAM and ≈45 mW for the hot SAM. A further increase in pump power self-starts femtosecond mode-locking: a stable, first-order soliton circulates in the cavity, giving a linear power–power slope and a clean RF spectrum (inset, left). At still higher pump levels the soliton destabilizes and breaks down, the cavity briefly re-enters a Q-switched state, and then locks again as a second-order soliton with twice the repetition rate (inset, right). For the cold SAM these transitions occur at 69 mW (first-order), 104 mW (breakdown), 111 mW (second-order) and 177 mW (second-order breakdown); the corresponding thresholds at 45 °C shift to 89 mW and 219 mW.

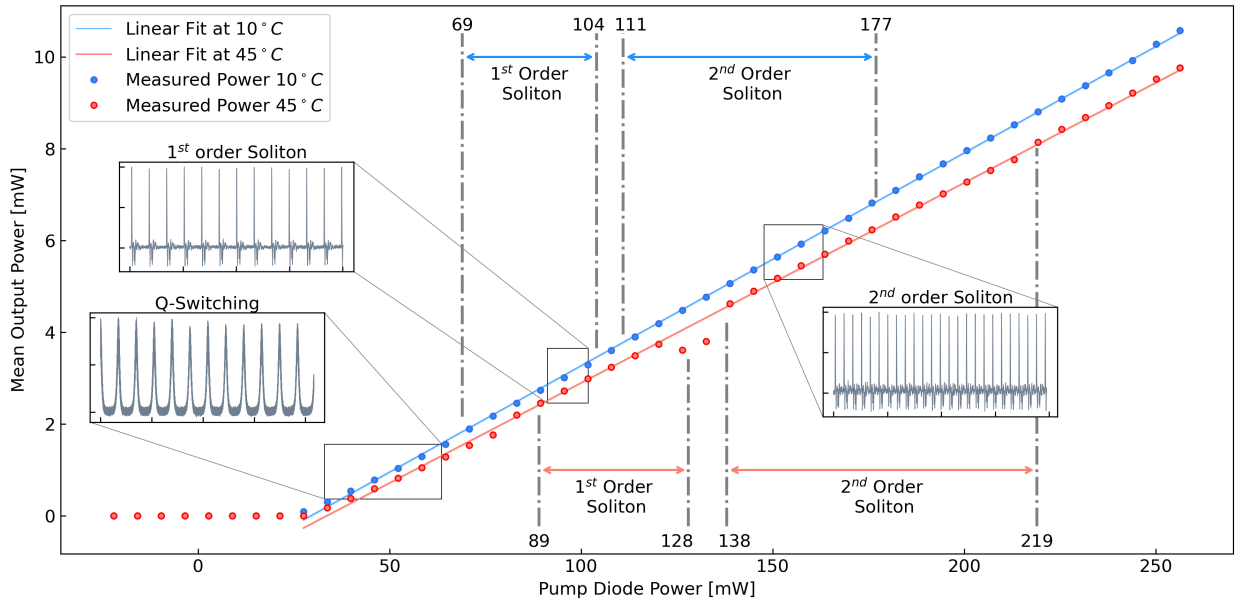

Figure 4.2 Master oscillator mean output power versus pump-diode power. Mean output power is plotted for two SAM temperatures: 10 °C (blue) and 45 °C (red). Solid points are measured data; thin lines are linear fits that reveal the slope efficiency of the cavity. Dash-dotted vertical lines label the transitions between the three operating regimes. Insets show oscilloscope traces characteristic of each regime: Q-switching just above threshold, fundamental (first-order) soliton mode-locking, and second-order soliton operation at higher pump powers. Numerical annotations (in mW) mark the pump-power boundaries between the regimes.

The temperature dependence stems from the SAM's reflectivity and saturation fluence: heat-

ing the absorber reduces its unsaturated reflectance and raises its saturation threshold, so more pump power is required to reach the net-gain condition [90]. Linear fits in Figure 4.2 show comparable slope efficiencies of 4.636×10^{-2} in the cold SAM case and 4.636×10^{-2} in the hot SAM case, confirming that temperature mainly shifts the lasing thresholds rather than altering the differential gain.

A closer look at the oscilloscope inset for the second-order regime reveals a slow, periodic modulation of the individual pulse peaks. This behavior is evidence of the soliton-energy quantization phenomenon: once the available intracavity energy exceeds the first-order soliton limit, the cavity does not produce a single, more energetic pulse but instead supports two identical solitons that propagate independently and maintain a fixed spacing. Because the detection window is not synchronized to that internal spacing, the two pulses interfere constructively and destructively in successive round-trip traces, giving the appearance of a "breathing" envelope in the peak-power plot. In general, the n^{th}-order regime accommodates n mutually balanced solitons that share the gain and loss in equilibrium [91, 92].

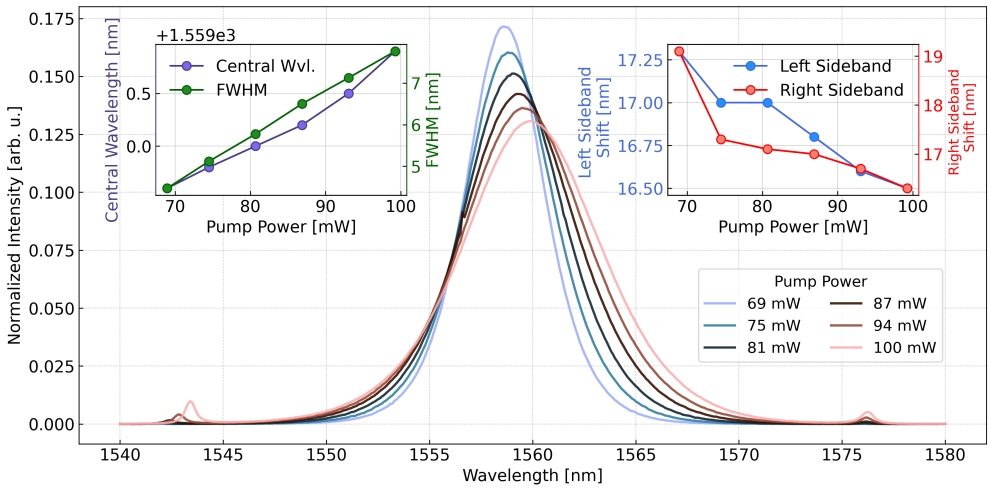

Figure 4.3 First-order soliton spectra for six increasing MO pump power (SAM at 10 °C). Main panel: normalized optical spectra recorded for absorbed pump powers between 69 to 100 mW. As the pump is raised the soliton broadens and its center wavelength drifts slightly towards higher wavelengths. Left inset: linear increase of spectral FWHM (green) from 4.8 nm to 7.6 nm, accompanied by an ≈ 1 nm red-shift of the center wavelength (purple). Right inset: positions of the Kelly sidebands on either side of the carrier; both sidebands move inwards with increasing pulse energy (see main text).

Pump-diode power not only sets the lasing threshold but also reshapes the spectra of the cavity solitons. Figure 4.3 (fundamental soliton) and Figure 4.4 (second-order soliton) show that raising the pump from the lower to the upper end of the operating range broadens the

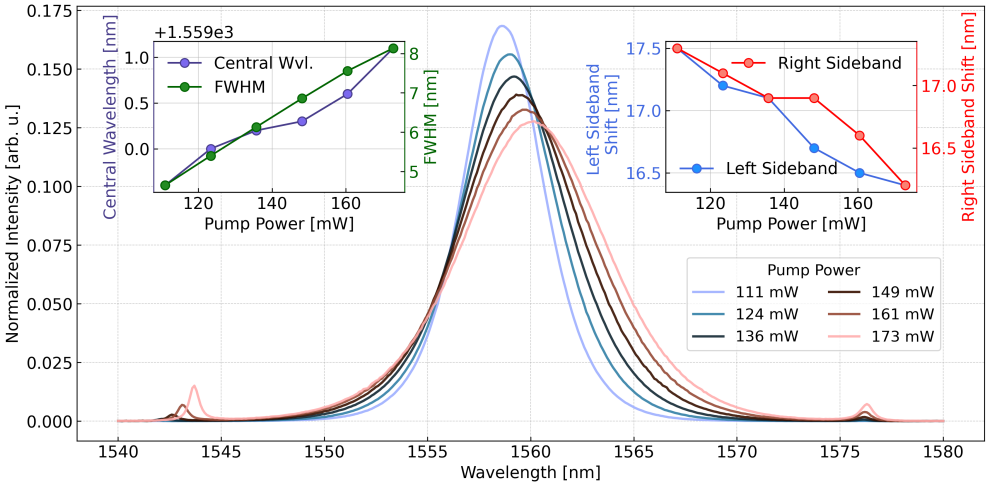

Figure 4.4 Second-order soliton spectra for six increasing MO pump power (SAM at 10 °C). Normalized output spectra for absorbed pump powers between 111 and 173 mW are shown in the main panel. As intracavity energy is raised, the spectrum broadens and shifts ≈ 1 nm toward longer wavelength, while a distinct pair of Kelly sidebands remains visible on both flanks. Left inset: the spectral FWHM climbs from 4.8 nm to 8.1 nm (green) and the center wavelength red-shifts by ≈ 1 nm (purple). Right inset: left- and right-hand sideband de-tunings contract toward the carrier as pulse energy increases but starting from a slightly smaller offset than in the first-order regime.

spectral Full Width at Half Maximum (FWHM) from roughly 5 nm to beyond 8 nm while simultaneously inducing a gradual red-shift of the central wavelength and a contraction of the Kelly sideband spacing (discussed in the next paragraph).

The broadening follows directly from the soliton "area theorem". For a fundamental soliton described by a solution to the cubic nonlinear Schrödinger equation, the pulse energy E_p and the pulses temporal full-width half-maximum lengths τ are linked by [93]

$$E_p = \frac{2|\beta_2|}{|\gamma|\tau}, \tag{4.2}$$

where γ is the nonlinear self-phase-modulation coefficient and β_2 is the anomalous group-velocity dispersion. Pumping harder increases the intracavity pulse energy E_p; (4.2) therefore requires τ to contract. By Fourier duality a shorter pulse necessarily maps onto a broader optical spectrum, exactly as observed.

Two subtler pump-dependent features are also apparent. First, the soliton centroid red-shifts by ≈ 0.8 nm (first-order) and ≈ 1.0 nm (second-order) over the measured range. This red-shift originates from soliton self-frequency shift [94] and thermally assisted saturable-absorber

dynamics: as the SAM converts a fraction of the circulating pulse energy into heat, it alters both its carrier density and effective refractive index, nudging the band-gap wavelength and thus the soliton spectral centroid toward lower photon energies [95].

The other effect is related to the sharp satellite peaks that bracket the main soliton envelope. These are known as Kelly sidebands and are the spectral fingerprints of quasi-solitons that circulate in a cavity with discrete, round-trip perturbations. Each lap through the resonator subjects the pulse to a fixed sequence of gain fiber, passive fiber, dispersion-compensating components and output coupling. This weak but periodic modulation acts like a distributed grating: whenever the accumulated phase slip between the soliton and a co-propagating dispersive wave hits an integer multiple of 2π, energy is resonantly transferred to the wave, producing sharp sidebands at the phase-matched frequencies [96].

Figure 4.3 and Figure 4.4 show that the sidebands move progressively closer to the carrier as the pump power rises. Kelly's original perturbation paper models this trend. For the N^{th} sideband, the wavelength offset with respect to the soliton center is [97, 98]

$$\Delta\lambda_N = \pm N \cdot \lambda_0 \sqrt{\frac{2N}{cDL} - 0.0787 \frac{\lambda_0^2}{(c\tau)^2}} \tag{4.3}$$

where λ_0 is the carrier wavelength, D the net cavity dispersion, L the cavity length and τ the soliton FWHM duration. Since pumping harder increases the intracavity energy and thus drives τ down, the second (negative) term under the square root grows and the overall offset $|\Delta\lambda_N|$ shrinks. The inward "march" of the Kelly sidebands is therefore a quantitative gauge of the shorter, higher-energy pulses obtained at elevated pump power, in full agreement with (4.3).

The recorded spectra provide two independent, all-optical gauges, of the pulse duration and, through the area theorem, of the intracavity energy without the need for high-energy diagnostics.

First, invoking the sech^2 Time Bandwidth Product (TBP) for a transform-limited soliton ($\Delta\nu\,\tau_{\text{FWHM}} \approx 0.315$), the measured 5–8 nm FWHM bandwidths translate to pulse widths that shrink from 571 fs to 329 fs as the pump is raised from 69 mW to 100 mW for the fundamental soliton, and from 549 fs (111 mW) to 334 fs (173 mW) for the second-order soliton. Substituting these τ values into (4.2) places the intracavity energies in the low-picojoule range, in line with expectations for fiber-based master oscillators.

Second, measuring the first-order Kelly-sideband offsets and applying (4.3) yields pulse widths of 521–322 fs for the fundamental and 587–312 fs for the second-order soliton. The two

methods agree to within ≈ 10 %, backing the quasi-soliton interpretation and providing an alternative to SHG-FROG when the pulse energy is too low for direct time-domain metrology at the master oscillator output.

Erbium-Doped Fiber Amplifier

The erbium-doped fiber amplifier has only two user-adjustable degrees of freedom; the drive currents of its two 979 nm pump diodes. In principle, trimming those currents lets one fine-tune the amplifier's spectro-temporal output via changes in gain saturation, self-phase modulation, and residual dispersion. In practice, however, the foremost requirement of this experiment is maximum average power to seed the downstream SHG stage and, ultimately, the SPDC source. A systematic sweep of pump-current combinations confirmed that the highest downstream power is obtained when the MO is operated in its second-order soliton regime and both EDFA pumps are driven at their full rated current (≈906 mW each). The remainder of this section therefore characterizes the amplifier's behavior as the MO output is varied while the EDFA pumps remain pinned to their maximum setting.

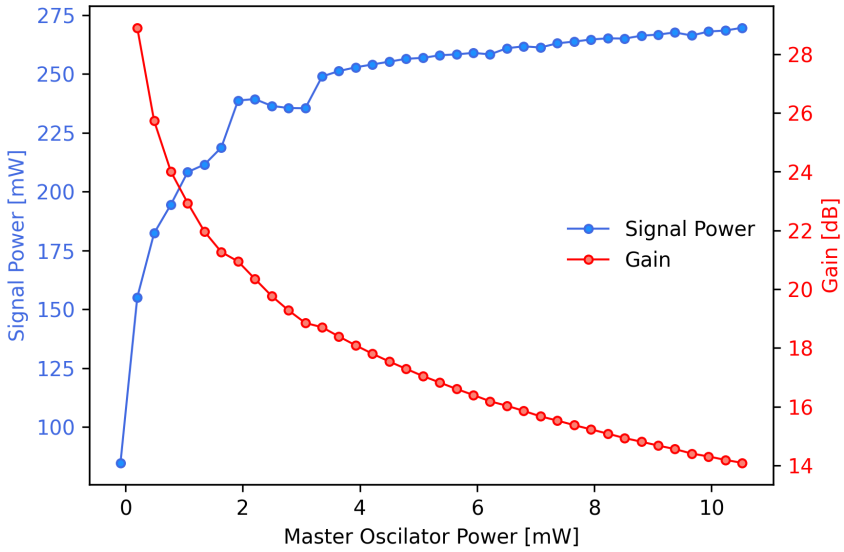

Figure 4.5 Net performance of the C-band EDFA when both 979 nm pump diodes are driven at their maximum current (906 mW each). The blue trace (left ordinate) shows the absolute signal power delivered by the amplifier as the MO input is stepped from 0 to 10 mW (first and second soliton), while the red trace (right ordinate) plots the corresponding optical gain in dB. The amplifier provides a small-signal gain of ≈ 29 dB and delivers >250 mW of output power, but exhibits the expected gain-saturation roll-off: as the MO power rises, the available inversion is depleted and the gain tapers to $\tilde{1}4$ dB at the highest tested input level, causing the output to level off around 270 mW.

Figure 4.5 plots the EDFA's output signal power (blue) and the corresponding net gain (red) MO input power. With the MO operating in the fundamental soliton regime (<4 mW input), the amplifier behaves like a classic small-signal device: the weak, sub-nanojoule pulses experience nearly the full population inversion and are boosted by $\sim$ 29 dB, driving the output to just below 250 mW. As the input is increased the stored-energy reservoir is depleted faster than it can be replenished, the gain saturates, and both the gain curve and the output power flatten.

Beyond $\approx$4 mW of MO power the laser self-adjusts into its second-order soliton state. Each cavity round trip now delivers twice the repetition rate but only half the pulse energy, so the instantaneous depletion of the EDFA inversion is reduced. The gain therefore recovers slightly, climbing a few dB, and the output tracks upward to $\sim$270 mW before tapering off again at the highest drive levels. This underscores the trade-off between pulse energy and repetition rate in power-scaling fiber systems: moving to higher-order solitons can reclaim amplifier headroom even when the pump diodes are already at their maximum current (906 mW each in this experiment).

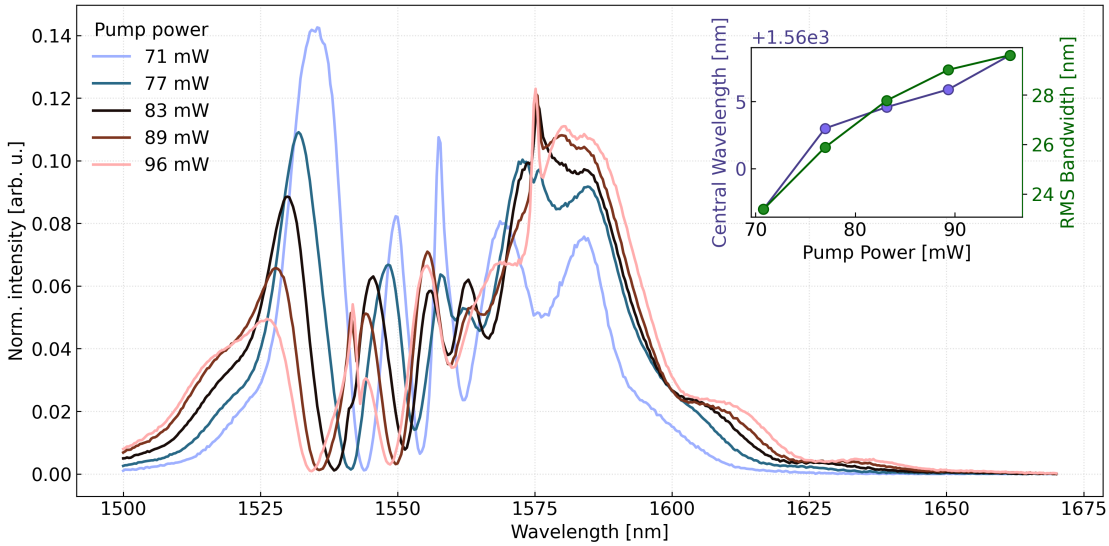

Figure 4.6 Spectral evolution of the first-order soliton after the EDFA for increasing MO pump power. With both 979 nm pump diodes driven at their maximum 906 mW, self-phase modulation in the erbium-doped fiber broadens and heavily modulates the soliton from 24 nm bandwidth at71 mW (light blue) to a 29 nm span at 96 mW (coral). Concomitantly, the spectral centroid drifts to longer wavelength as the higher-energy pulses sample the red-tilted EDFA gain profile. The inset quantifies these trends: the centroid (blue markers, left axis) shifts by $\approx$ 10nm, while the RMS bandwidth (green markers, right axis) climbs by $\approx$20%. The multi-lobed structure reflects the interplay of gain shaping, residual dispersion and cascading SPM along the amplified section.

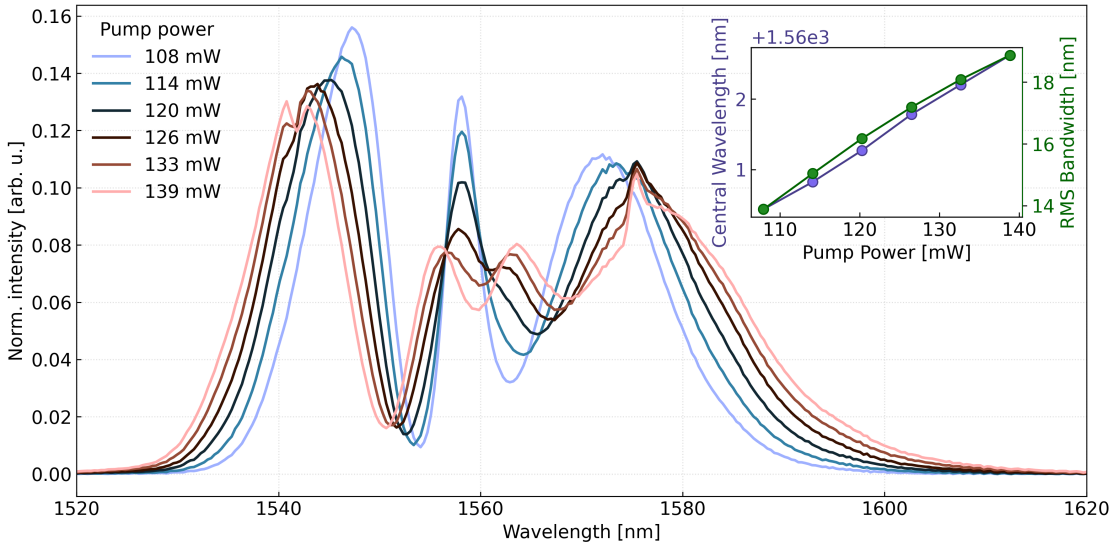

Figure 4.7 Spectral evolution of the second-order soliton after the EDFA, recorded while the master oscillator pump power is stepped from 108 mW to 139 mW. With both 979 nm pump diodes driven at their maximum current, the broader, higher-repetition-rate second-order pulses undergo weaker Self Phase Modulation (SPM) than their fundamental counterparts, yet their spectra still evolve in a systematic way. The inset shows that the RMS bandwidth widens from about 14 nm to 19 nm as the drive increases, and that the spectral centroid drifts by roughly 2 nm toward longer wavelengths, an effect that follows the red shift of the EDFA gain curve at higher fluence. Although the bandwidth growth is more modest than for the first-order soliton, consistent with each pulse carrying only half the energy but arriving twice as often, the overall trend confirms that SPM remains the dominant agent of spectral broadening and red-shifting as the drive power is increased.

Figures 4.6 and 4.7 show that passage through the EDFA dramatically reshapes the spectra of both the first- and second-order solitons. The dominant mechanism is SPM: as the high-peak-power pulses traverse the $\sim$ 1.7 m of highly nonlinear erbium-doped fiber, the Kerr effect imprints a time-dependent phase that, after Fourier transformation, manifests as a sequence of spectral lobes. Each time the accumulated nonlinear phase crosses an odd multiple of $\pi/2$ the instantaneous frequency chirp reverses sign, carving a new pair of peaks and giving the spectrum its characteristic "split" appearance. A convenient rule of thumb relates the total SPM-induced spectral phase to the lobe count, N, via $\phi_{\mathrm{SPM}} \simeq (N - \frac{1}{2})\pi$ [64]. Counting the distinct maxima in Figure 4.6 therefore implies $\phi_{\mathrm{SPM}} \approx 4.5\pi$ for the fundamental soliton, while the cleaner, less modulated spectrum in Figure 4.7 corresponds to about 2.5π for the second-order soliton. Although spectral broadening is essential for achieving low femtosecond durations downstream, asymmetric SPM such as that seen in the first-order case is problematic: the strongly varying residual phase cannot be fully compensated by compres-

sors, leaving pronounced temporal sub-structures that hamper optimum pulse compression and, ultimately, single-mode operation in the SPDC stage. Finally, both figures reveal the amplification of the original Kelly sidebands once their wavelengths coincide with the peak of the erbium gain spectrum.

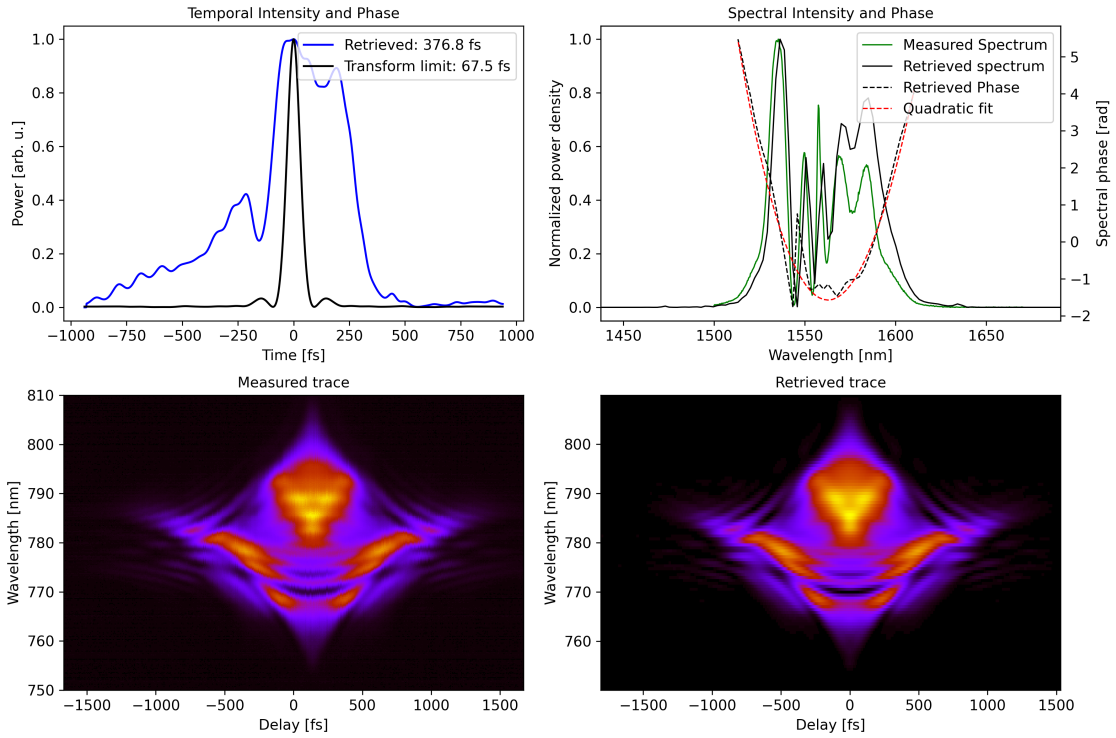

Figure 4.8 SHG-FROG retrieval of the first-order soliton at a Master Oscillator (MO) pump current of 71 mW (MO output ≈2.25 mW before the EDFA). Upper-left: Retrieved temporal intensity (blue) and phase, compared with the transform-limited envelope derived from the retrieved spectrum (black). The main pulse has an FWHM of ≈377 fs, nearly six times longer than its 68 fs transform limit, features prominent pre-pulse and trailing pedestals. Upper-right: Measured (green) and retrieved (black) spectra together with the retrieved spectral phase (dashed black) and its least-squares quadratic fit (red). The oscillatory phase is consistent with the SPM-induced modulation seen after the EDFA. Lower panels: Experimental (left) and reconstructed (right) SHG-FROG traces; the visual agreement confirms a reliable retrieval (FROG error $\leq 2 \times 10^{-3}$). The characteristic "winged" pattern reflects the spectral lobe structure and the large non-linear phase accumulation in and past the EDFA.

After amplification the soliton pulses are bright enough to be measured directly with the SHG-FROG apparatus introduced in Section 3.3. Figure 4.8 (fundamental soliton, 71 mW pump) and Figure 4.9 (second-order soliton, 136 mW pump) place the raw and COPRA-reconstructed FROG spectrograms alongside the retrieved temporal and spectral profiles.

Both traces expose a large positive quadratic spectral phase, around 8993 fs^2 for the first

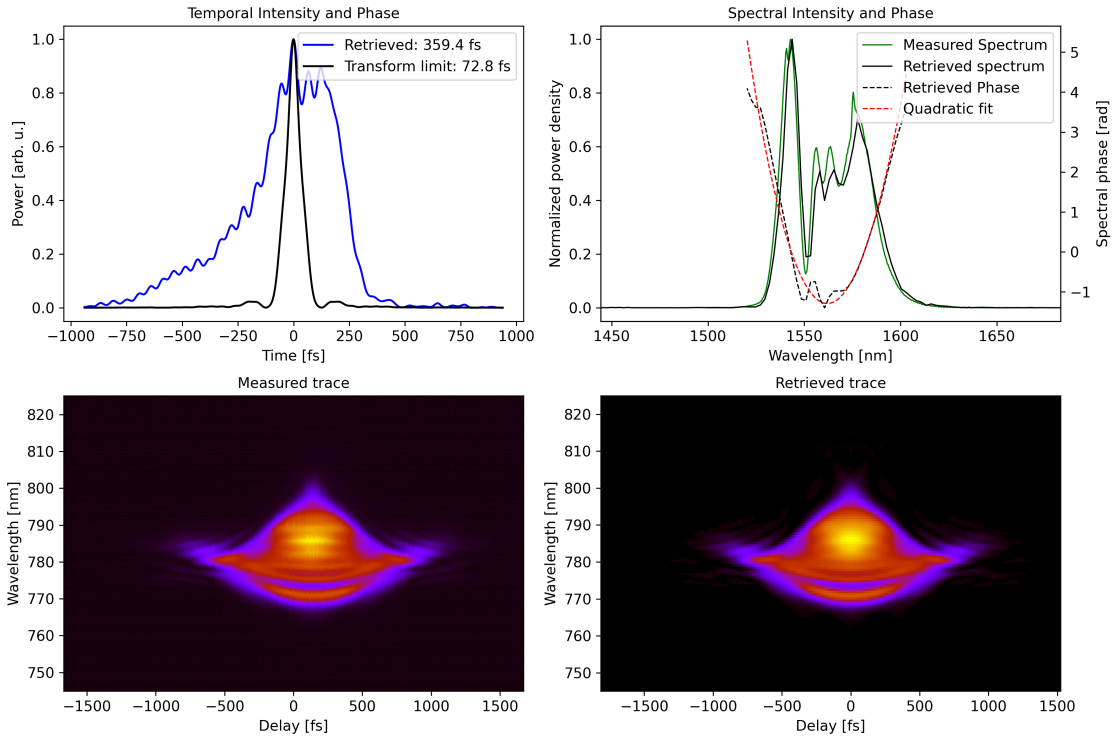

Figure 4.9 SHG-FROG retrieval for the second-order soliton at MO pump power of 136 mW (MO output ≈5 mW optical before the EDFA). Upper-left: Retrieved temporal intensity (blue) versus the transform-limited envelope supported by the measured spectrum (black). The pulse width is ≈359.4 fs FWHM, compared to an 73 fs transform limit, indicating a large residual chirp. The oscillatory noise is a measurement artifact. Upper-right: Measured spectrum (green) and retrieved spectrum (black) with the extracted spectral phase (dashed black) and its quadratic fit (red). Less phase oscillations are observed, consistent with the reduced SPM spectrum splitting. Lower panels: Experimental (left) and reconstructed (right) SHG-FROG traces display excellent agreement, confirming a robust retrieval (FROG error $\leq 3 \times 10^{-3}$). The "eye-shaped" fringe pattern, precursor to the previously observed wings, reflects the smoother spectral modulation and lower peak power of the second order soliton relative to its fundamental counterpart.

order soliton and 13 000 fs^2 for the second. Because the PM1550 cavity fiber is anomalously dispersive ($\beta_2 < 0$), this chirp must originate almost entirely in the normally-dispersive erbium-doped fibre of the EDFA and is reinforced by asymmetric self-phase modulation: it is suspected that the high-power core of the pulse saturates the gain more strongly than its wings, imprinting an additional positive phase that grows with input power [99]. The result is a retrieved pulse width five to six times larger than the transform limit in both soliton orders.

Pre-compensating this phase inside the fiber laser would require re-balancing in the MO

and the EDFA (discussed in Section 4.4). Instead, the current system relies on external compression: a prism pair positioned after the EDFA removes the bulk quadratic phase, while any residual oscillatory phase left by the unbalanced SPM is found to be cleaned up later throught the SHG process (Sections 4.2 and 4.3).

Quantitatively, the SHG-FROG measures FWHM durations of 375 fs to 253 fs for the fundamental soliton as the MO pump rises from 71 mW to 97 mW; the corresponding transform limits fall from 67 fs to 45 fs. In the second-order regime the pulses lengthen slightly, 509 fs to 359 fs over 114–139 mW, while their transform limits stay below 90 fs. Combining these durations with the average powers in Figure 4.5 gives per-pulse energies of a few nanojoules, enough to seed the downstream SHG and SPDC stages.

Noise and Stability

One of the first long term goals with this source is to produce quantum states of light by conditioning the intensity measurements between each twin beam. This requires that the classical noise of the pump be understood, and ideally, minimized, well before the quantum correlations are analyzed. The natural figure of merit is the RIN, which expresses intensity fluctuations as a fraction of the mean power and is therefore independent of any absolute calibration. In the time-domain the root-mean-square RIN is defined as [100]

$$\mathrm{RIN}_{\mathrm{rms}} = \frac{\sigma_P}{\langle P \rangle}, \tag{4.4}$$

where $P(t)$ is the instantaneous optical power, $\langle P \rangle = \langle P(t) - \bar{P} \rangle$ its mean over a record of length $t_{\max}$, and σ_P the corresponding standard deviation. A complementary, and often more informative, description is obtained in the frequency domain by forming the single-sided Power-Spectral Density (PSD), $S_P(f)$, of the fluctuations. Normalizing by $\langle P \rangle^2$ yields the spectral RIN [101],

$$\mathrm{RIN}(f) = \frac{S_P(f)}{\langle P \rangle^2} = \mathcal{F}\left[\frac{\langle \Big(P(t) - \langle P \rangle\Big)\Big(P(t+\tau) - \langle P \rangle\Big) \rangle_\tau}{\langle P \rangle^2}\right], \tag{4.5}$$

whose integral over the analysis bandwidth $[1/T,\ f_{\mathrm{rep}}/2]$ gives the integrated RIN,

$$\text{i-RIN} = \int_{1/t_{\max}}^{f_{\mathrm{rep}}/2} \mathrm{RIN}(f)\, df. \tag{4.6}$$

These two definitions, the time-domain RMS and frequency-domain integrated-RIN (i-RIN), will be used throughout this section to quantify the source's stability.

The absolute limit for any intensity-noise measurement is the quantum–mechanical shot-noise limit, the fluctuation that remains even if all classical noise sources are eliminated. Shot noise originates from the discrete, Poissonian arrival of photons at the detector; its single-sided PSD therefore scales with the photon energy $h\nu$ and is inversely proportional to the average optical power $\langle P \rangle$:

$$\mathrm{RIN}_{\mathrm{shot}}(f) \;=\; \frac{2h\nu}{\langle P \rangle}. \tag{4.7}$$

The factor 2 merely converts the two-sided shot-noise spectrum to the single-sided convention. For the two operating conditions investigated; 136 mW MO pump for standard second-order soliton operating conditions and 99 mW for a power-matched fundamental soliton, the shot-noise RIN floors are -159 dB Hz^{-1} with the EDFA off and -179 dB Hz^{-1} at full EDFA gain. Any RIN trace that reaches these levels, once detector responsivity and electronics noise are removed, is already quantum-noise-limited; further suppression can only come from higher optical power, tighter mode matching, or quantum-correlation techniques rather than additional classical stabilization.

The RIN was characterized by following the methodology in [102]. A 1.2 GHz InGaAs photodiode (Thorlabs DET01CFC) monitored the pulse train, and a 2.5 GHz oscilloscope (Keysight DSO9254A) acquired 205 Mpoint at 10 GSa/s. The 20.5 ms record length fixes the resolution bandwidth at 64.5 Hz which is used as the lower integration bound for the i-RIN, while the 10 GSa/s sampling rate sets a 5 GHz Nyquist limit, well above the highest noise component of interest, $f_{\mathrm{rep}}/2 \simeq$30 MHz. The 30 MHz analysis bandwidth, one half of the 60.1 MHz cavity round-trip frequency, is adequate for both the fundamental and second-order operating points. Recall that the second order state may be pictured as two bound solitons circulating together, thus the pulse train still repeats at the same 60.1 MHz rate, so every pulse-to-pulse intensity fluctuation is confined to sidebands below $f_{\mathrm{rep}}/2$. Because the optical pulse (571 fs at most) is far shorter than the photodiode's 0.9 ns electrical rise time, each pulse is recorded as a delta function-like spike whose voltage peak is proportional to its energy. The detector response time is likewise much shorter than the 8 ns period between pulses, allowing the baseline to settle to the electronic noise floor between peaks. These inequalities ensure that the peak-sampled voltage sequence faithfully captures pulse-to-pulse energy fluctuations while providing a clean reference region for accurate power-spectral-density estimation.

For the time-domain RIN analysis each pulse's peak voltage is first corrected for the electronic baseline: the average "floor" voltage level, obtained by integrating over the central 80 % of the interpulse interval, is subtracted sample-by-sample before peak detection. The resulting peak-voltage stream is then low-pass–filtered with a moving-average window that rolls off at 30 MHz, matching the frequency range covered in the PSD measurement. Figure 4.10 plots

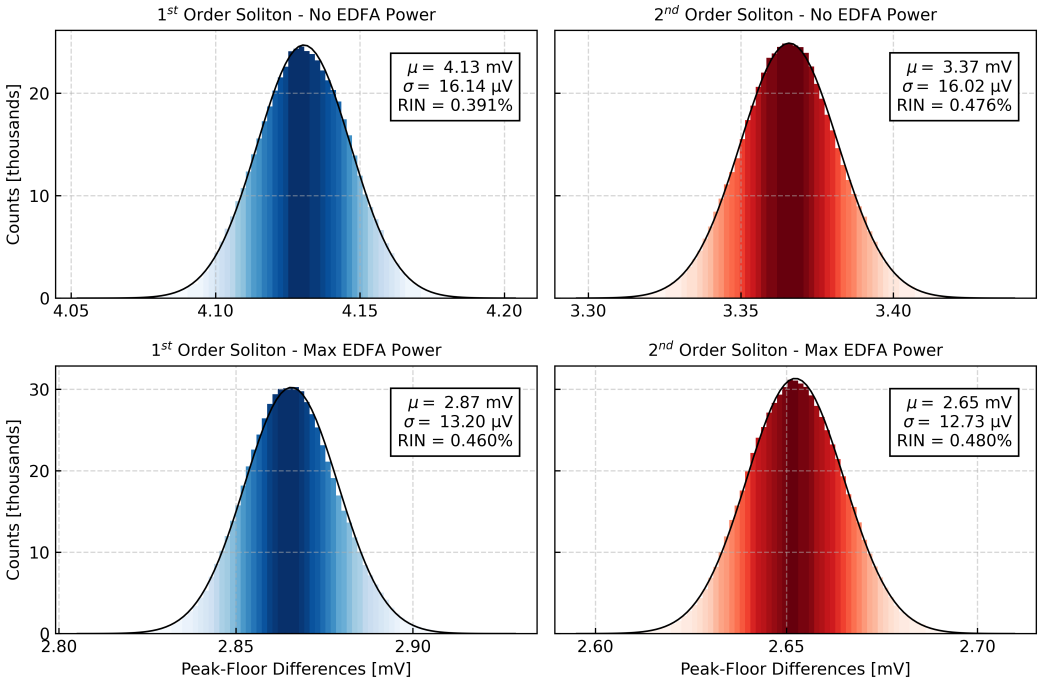

Figure 4.10 Temporal relative-intensity noise of the fiber laser's soliton output, obtained from histograms of the peak–floor voltage recorded over 10^6 consecutive pulses. Top row: laser operated without EDFA gain; bottom row: EDFA driven at its maximum 906 mW pump power. Left: fundamental (1st-order) soliton; right: 2nd-order soliton. Bars show the measured distribution, while the black curves are Gaussian fits from which the mean pulse amplitude μ, the RMS fluctuation σ, and the normalized RIN $= \sigma/\mu$ (values inset) are extracted. EDFA amplification reduces the mean peak–floor voltage but leaves σ nearly unchanged, so the RIN rises from 0.39 % to 0.46 % for the 1st order soliton and remains around 0.48 % for the 2nd order soliton. Under both operating conditions the 2nd-order soliton exhibits the larger RIN, confirming that higher-order dynamics impose stronger pulse-to-pulse intensity fluctuations.

the histogram-derived RMS RIN for all four operating points. Two clear trends emerge. Driving the EDFA to full gain raises the mean pulse energy while simultaneously clamping small-signal fluctuations through gain saturation; because shot noise grows only as the square-root of power whereas the signal grows linearly, the relative (power-normalised) noise floor drops. In addition, the EDFA's long upper-state lifetime (≈1 ms) acts as a low-pass reservoir that smooths pump-induced intensity jitter [103]. Further, the second-order soliton has a higher RIN. As discussed, the second order operating point consists of two quasi-independent solitons circulating in tandem. Each accrues its own amplitude and phase jitter from cavity loss, spontaneous emission and fiber non-nonlinearities; because these fluctuations are largely uncorrelated, their variances add, while the mean power only doubles. The net effect is a

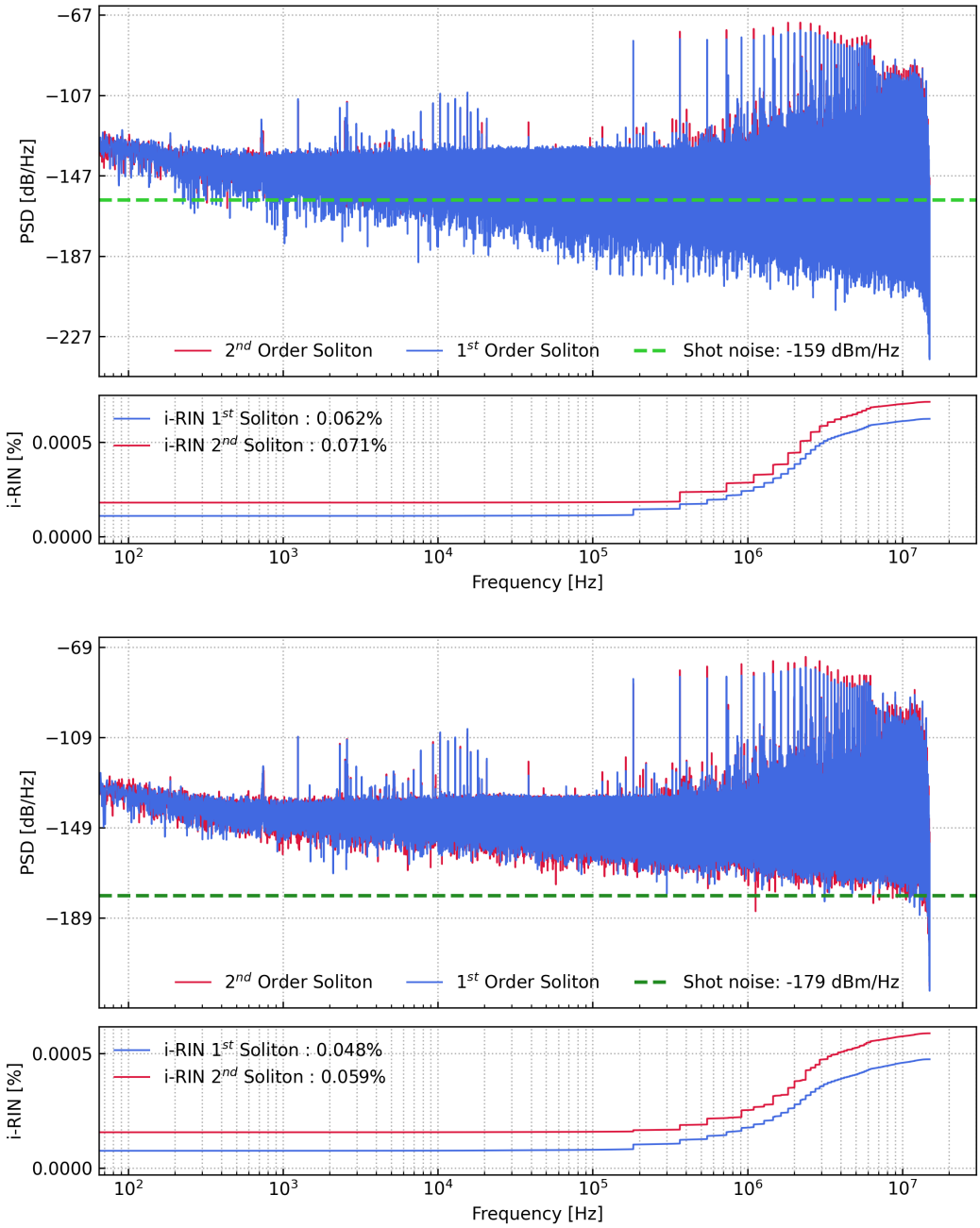

Figure 4.11 Frequency-domain assessment of the laser's intensity stability for the fundamental (blue) and 2nd-order (red) solitons. Top panel: laser operated without EDFA gain; bottom panel: EDFA pumped at its maximum 906 mW. Upper traces show the single-sided PSD of the photocurrent fluctuations; the green dashed line indicates the shot-noise floor. Lower traces plot the i-RIN characterized to half the repetition rate of the first order soliton. At full bandwidth of 30 MHz the i-RIN reaches 0.062 % for the 1st-order soliton and 0.071 % for the 2nd-order soliton in the ungained case; EDFA amplification lowers these figures to 0.048 % and 0.059 %, respectively.

larger σ/μ ratio and hence a higher RIN compared with fundamental regime.

Frequency-domain RIN is obtained from the same oscilloscope trace by computing the single-sided power-spectral density $S_V(f)$ of the baseline-subtracted voltage $V(t)$ and normalizing it with $\langle V \rangle^2$ as prescribed in equation 4.5. Figure 4.11 overlays the PSD spectra for the fundamental and second-order solitons. The main features mirror the time-domain results: the second order state exhibits a consistently higher RIN than the fundamental, and driving the EDFA into saturation lowers the overall noise floor. For the unamplified oscillator, measure i-RINs of 0.062 % (fundamental soliton) and 0.071 % (second-order soliton). These values align with typical figures for negatively-dispersion-managed, SESAM mode-locked Er-fiber sources, e.g. 0.072 % reported for a 162 MHz system [104], but remain above the best-in-class 0.014 % achieved in a dispersion-managed 1 GHz SESAM Er-fiber laser [105].

Several spectral details deserve comment. A broadband shoulder that rises above shot noise near ≈1 MHz appears in both soliton orders and is more pronounced when the EDFA is off; it is characteristic of amplified-spontaneous-emission beating within the oscillator. Superimposed on this pedestal are narrow peaks: the strongest ones at integer multiples of f_{rep} stem from residual mode beating, while weaker lines below 100 kHz track pump-diode current noise and cavity-length dither [106].

Note that because the EDFA-on measurement required neutral-density attenuation to keep the photodiode response linear (and most importantly functional), the plotted RIN spectrum is referenced to the attenuated power rather than the full intracavity level. Although this means the absolute shot-noise floor is understated, the trace still correctly reveals relative features, most notably the ≈10 kHz pump-noise spur [106], and thus remains valuable for diagnosing dominant noise mechanisms.

Concluding, the RMS RIN extracted from the pulse-peak statistics does not coincide with the value obtained by integrating the PSD. For the two estimates to agree, one must integrate the single-sided spectral RIN all the way from DC to f_{rep} and remove the discrete comb lines at the harmonics nf_{rep} [102], because the peak-sampling method is insensitive to those narrow intracavity mode-beating tones. The mismatch therefore reflects slightly different effective bandwidths and the unequal treatment of the nf_{rep} features rather than any inconsistency in the underlying data; with adjusted integration ranges, notch filters at the mode-beat frequencies and identical low-pass cut-offs, the two RIN estimates would converge, as required by Parseval's theorem.

Finally, the stability measurement is plotted in Figure 4.12. Over one hour, the average output power of both operating regimes remains relatively steady. The second-order soliton delivers a higher mean power (227 mW) than the fundamental (220 mW), yet the absolute

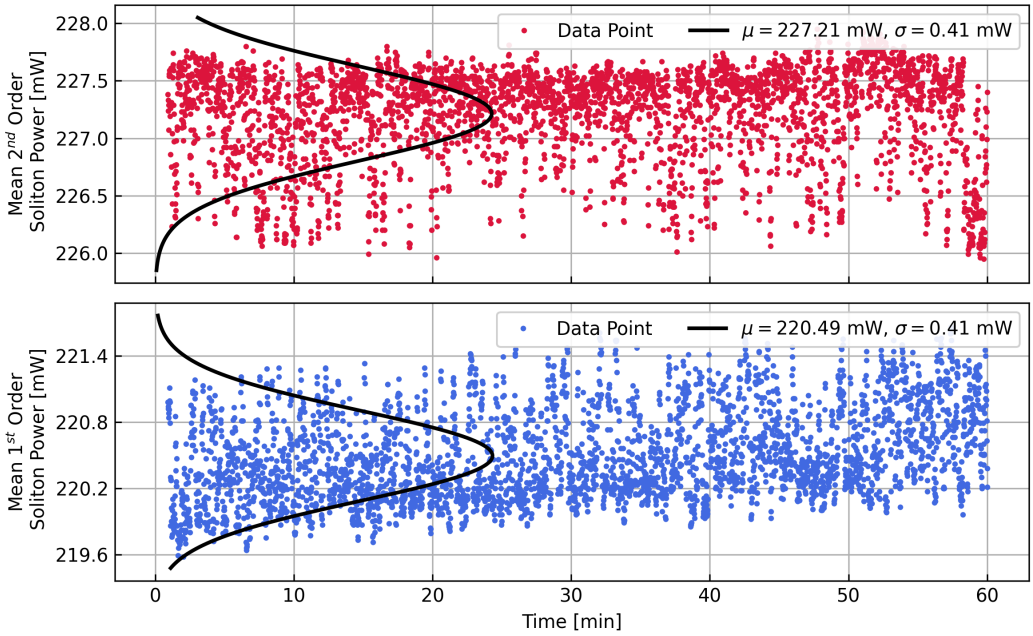

Figure 4.12 Mean output power of the second-order (top, red) and fundamental (bottom, blue) solitons over a 60-minute run. Dots are per-trace data points sampled at 1 Hz; the solid black curves overlay the marginal distributions, giving $\mu_{2\mathrm{nd}}$ =227.2 mW and $\mu_{1\mathrm{st}}$ =220.5 mW with identical rms drifts of 0.41 mW.

drift is identical in both cases: a one-sigma spread of only 0.41 mW. This corresponds to a fractional stability of ≈0.18 %, fully consistent with the sub-percent RIN measured in the frequency domain, indicating that long-term thermal and pump fluctuations are reasonably suppressed and do not preferentially affect either soliton order.

4.2 Temporal Engineering and Pulse Compression

Equipped with the knowledge of the full complex field (envelope) retrieved by SHG-FROG (recall that the underlying frequency comb cannot be resolved directly), the chronocyclic Wigner/SVD framework introduced in Section 3.1 can finally be deployed. Applying it to the pulses of Figures 4.8 (first-order) and 4.9 (second-order) yields the Wigner maps shown in Figure 4.13. In both cases a bright ridge that climbs from early times toward higher frequencies indicates a large positive chirp suspected to be imposed by the normally dispersive erbium fiber. The fundamental soliton features more red–blue interference bands and a more pronounced horizontal "S-bend", both indicators of strong SPM. The more intense SPM can also be observed in the spectral phase, with more phase shifts ($\approx 4.5\pi$). The $N = 2$ soliton, which carries half the pulse energy at twice the repetition rate, accumulates only $\approx 2.5\pi$ of

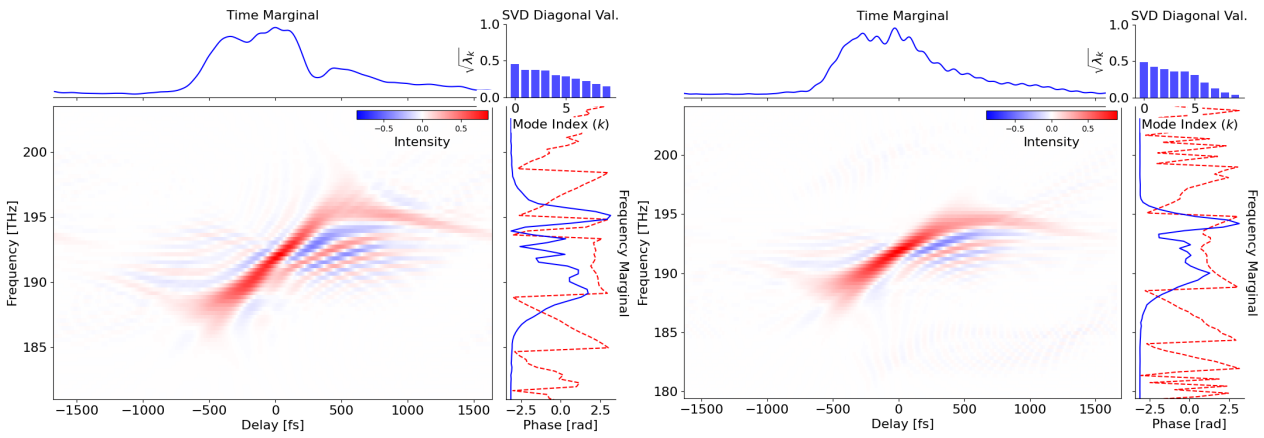

Figure 4.13 Chronocyclic Wigner function of the amplified solitons. Left: first-order soliton (MO pump power of 71 mW); right: second-order soliton (MO pump power of 136 mW). Each main panel shows the joint time–frequency Wigner density matrix $W_C(t,\omega)$; top and right marginals give the temporal and spectral intensities, and the insets list the dominant singular values from an SVD analysis.

SPM; its Wigner map therefore shows milder fringes and a closer to quadratic phase.

The singular-value decomposition of each Wigner matrix quantifies the mode content. The first-order pulse spreads its energy over more orthogonal chronocyclic modes, giving an effective Schmidt number $K_C \approx 8$; the second-order pulse is cleaner at $K_C \approx 6.4$. Higher-order operation thus suppresses some of the excess spectro-temporal modes.

The immediate challenge at the output of the EDFA is therefore to drive the number of spectro-temporal modes down as much as possible, and enhance the pulse quality to drive more efficient SHG and later purer SPDC. Two mechanisms discussed above inflate the chronocyclic Schmidt number: unbalanced self-phase modulation, whose oscillatory phase grows with peak power, and a large positive quadratic chirp. The first can be mitigated by operating the cavity in the second-order-soliton regime, while the second can be removed with a standard grating- or prism-pair compressor that supplies negative group-delay dispersion. To quantify the extent of how beneficial such an added phase would be, Figure 4.14 contrasts, for a range of MO pump powers, the Schmidt number K_C and pulse width measured directly from SHG-FROG, with the same quantities after numerically stripping only the quadratic phase (i.e. the performance reachable with a pure GDD compressor). For the fundamental soliton both the raw FWHM and K_C fall as MO power rises because energy leaks into satellite pulses, but once the quadratic chirp is removed the K_C still creeps upward, indicating that growing SPM, not residual GDD, dominates the multimode content. The second-order soliton behaves oppositely: its raw K_C increases slightly with power, yet after quadratic

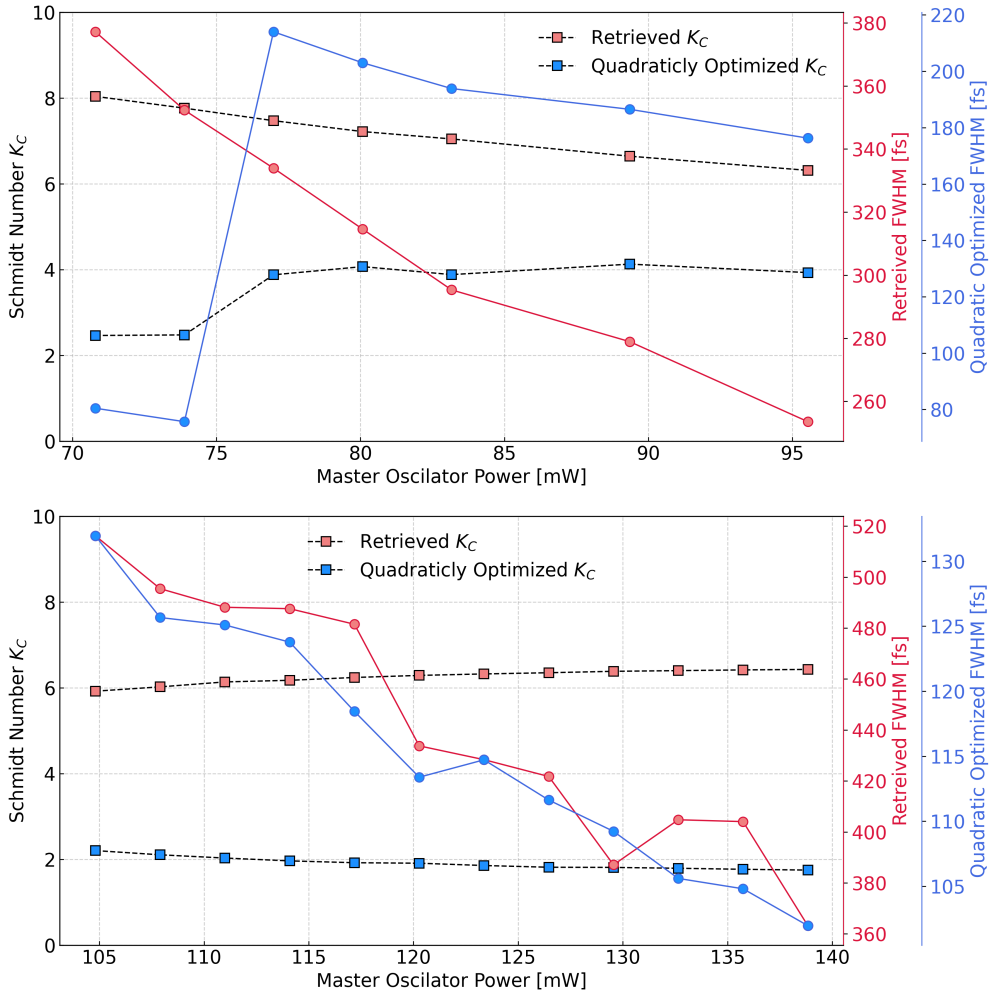

Figure 4.14 Impact of pure GDD compensation on pulse quality. Chronocyclic Schmidt number K_C (left ordinate) and temporal FWHM (right ordinate) plotted versus master oscillator pump power for the first-order soliton (upper panel) and second-order soliton (lower panel). Red symbols give the raw SHG-FROG values at the EDFA output; blue symbols show the same pulses after numerically stripping the best-fit quadratic phase, i.e. the performance attainable with a grating/prism GDD compressor. Removing only the quadratic term roughly halves K_C for the first-order pulse and drives the second-order pulse toward $K_C \approx 2$, while compressing the duration by a factor of ≈ 3 in both cases.

compensation it drops monotonically (approaching ≈ 1.9 at the highest drive) and the pulse compresses theoretically from $\approx$480 fs to $\approx$105 fs. Thus, combining the second order operating point with a simple negative GDD compressor is the most effective route to near-single-mode operation without sacrificing average power.

With the second soliton chosen as the working point since its chronocyclic Schmidt number can be driven to below 2 with only quadratic compensation, the pulse is compressed with a

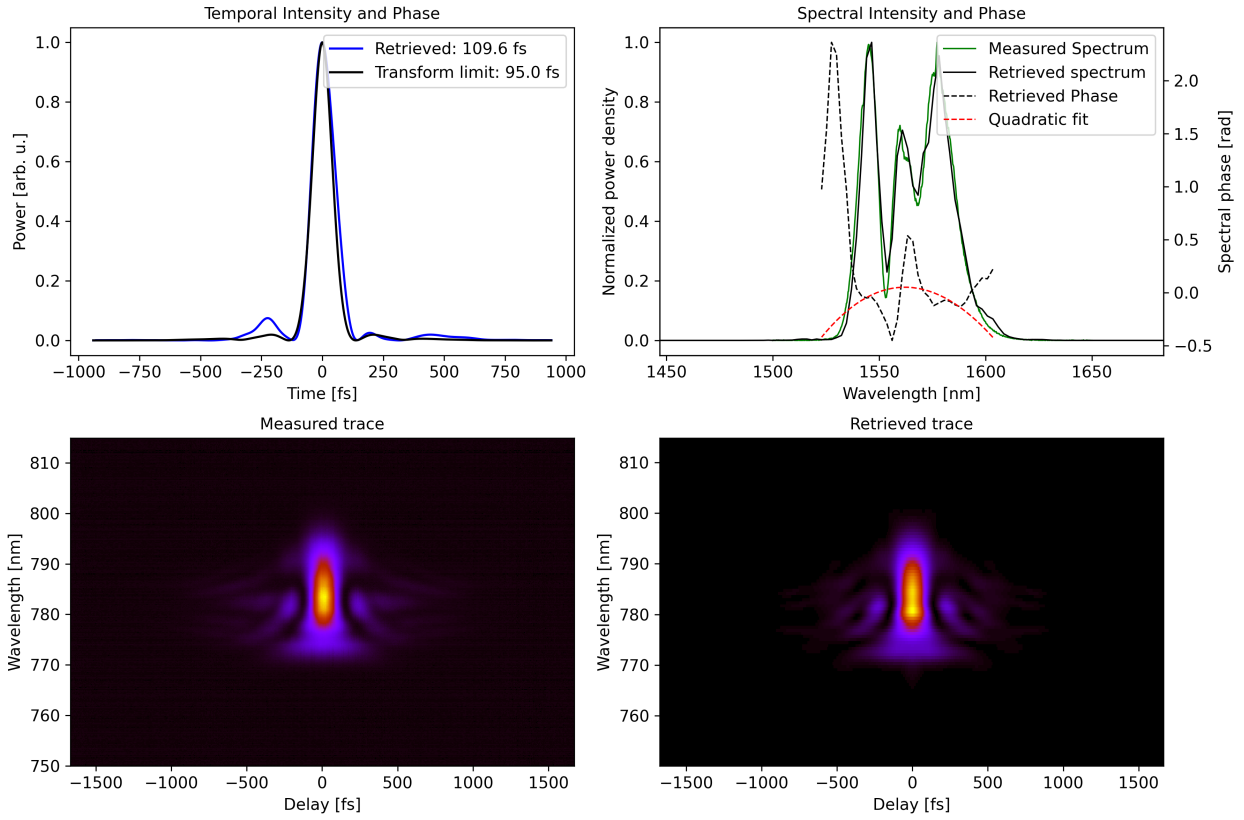

Figure 4.15 SHG-FROG of the prism compressed second order soliton (MO pump ≈136 mW). After the silicon-prism compressor, the retrieved pulse narrows to 110 fs FWHM, only 17 % above the 93 fs transform limit, with its quadratic phase essentially canceled. The measured and reconstructed spectrograms overlap closely, confirming successful single-stage GDD compression.

two-prism silicon compressor (Figure 4.17). Silicon offers a high negative GVD at 1.56 µm, allowing the 13 000 fs^2 of positive GDD accumulated in the cavity and EDFA to be canceled within a small footprint. The prisms have a 32.1° apex angle; their parallel faces are separated by 53 mm, and the beam enters the first prism 3 mm, and the second prism 5 mm, from their respective apices. This geometry delivers $-1.31 \times 10^4 fs^2$ of GDD and an associated third-order dispersion of $-1.63 \times 10^5 fs^3$. Operating near Brewster angle keeps Fresnel losses below 20 mW, although the residual negative TOD contributes slightly the formation of asymmetric satellite pulses. The prism separation is fine-tuned in situ by maximizing the downstream SHG signal, ensuring that the quadratic phase is suppressed as much as possible.

Figures 4.15 (compressed SHG-FROG retrieval) and 4.16 (corresponding chronocyclic Wigner function) depict the second-order soliton (show in Figure 4.9) after optimal two-prism compression. This is the pulse configuration that maximize the SHG output discussed in the next

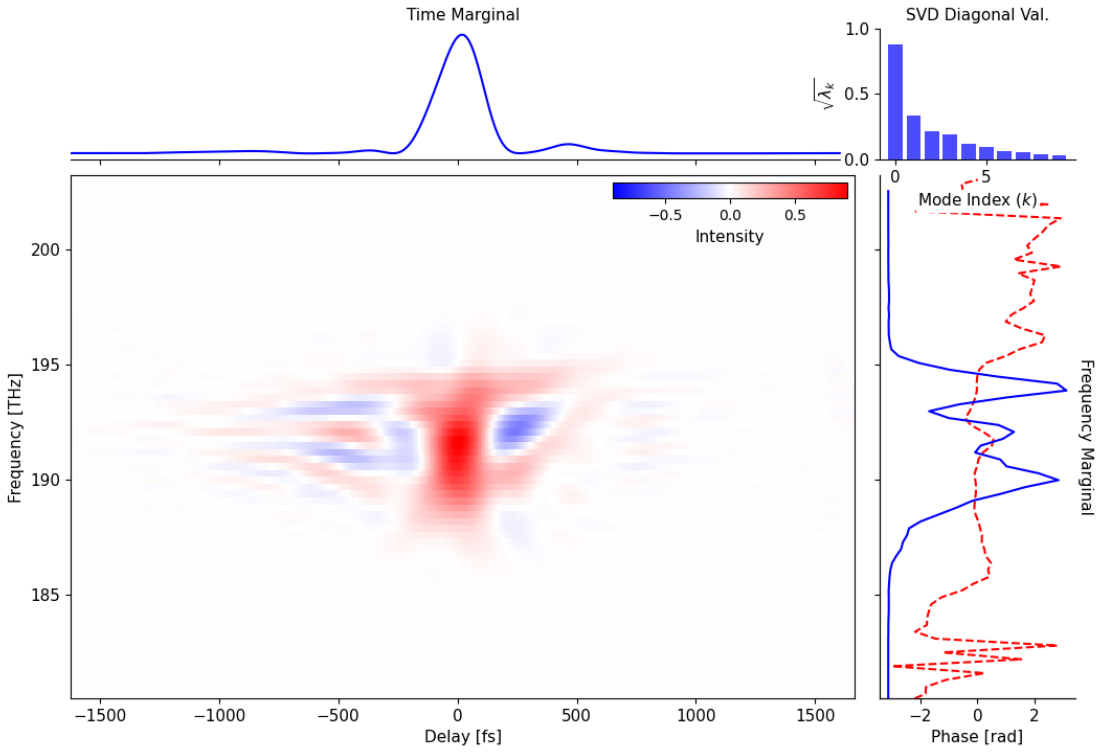

Figure 4.16 Chronocyclic Wigner function of the prism-compressed second-order soliton. The joint time-frequency density now shows a near-vertical, almost symmetric core, confirming removal of the large positive chirp; residual red-blue sidelobes stem from the small cubic phase left by the silicon prisms. An SVD of the map yields a dominant first singular value that captures >80 % of the energy, giving an effective Schmidt number $K_{\mathrm{C}} \approx 1.64$, a more than three-fold reduction relative to the uncompressed pulse.

section. The steep time-to-frequency tilt that dominated the uncompressed Wigner function has disappeared, leaving an almost vertical core. Only a faint, asymmetric pedestal survives in the temporal marginal, attributable to the residual TOD imposed by the silicon prisms. Singular-value analysis now gives an effective Schmidt number $K_{\mathrm{C}} = 1.64$, slightly below the ~ 2 predicted from the quadratic-only model; the extra reduction stems from mild spectral filtering of the wings by the residual TOD, which concentrates energy into the principal mode. The pulse width compresses to 110 fs, within 15 % of the 95 fs transform limit, which is also pushed up by the TOD.

The characterization of the laser's temporal characteristics shows that chasing the shortest FWHM alone is a poor proxy for true single-mode performance. More important in our opinion is the spectro-temporal purity of the field; how much energy resides in a single, well-

defined joint time-frequency mode. The chronocyclic Wigner/SVD framework introduced here provides a quantitative yard-stick: the effective Schmidt number K_C. By analyzing K_C rather than pulse width, it was discovered that operating in the second-order-soliton regime and compensating only the quadratic phase yields a pulse that is appreciably cleaner ($K_C \approx 1.64$) than a shorter, more distorted fundamental soliton. The method therefore supplies a practical design loop for optimizing pulse systems whenever non-trivial nonlinear phase is unavoidable: retrieve the electric field with its phase, calculate the Wigner map, and minimize K_C.

4.3 Second-Harmonic Based Generation of the SPDC Pump

4.3.1 Experimental Configuration and SHG Performance

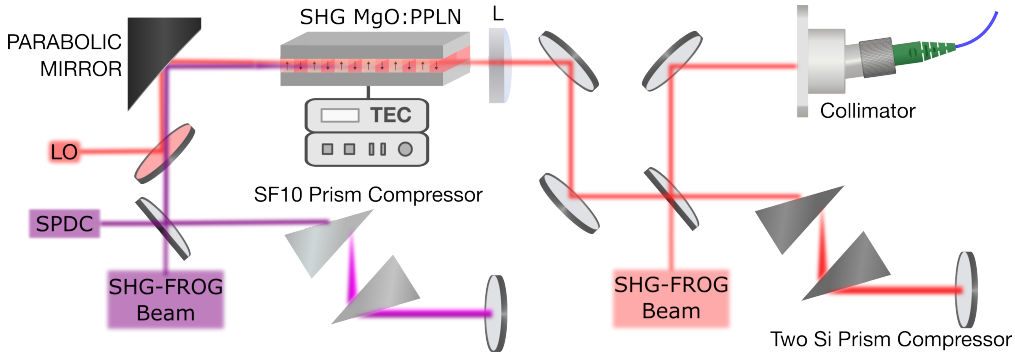

Figure 4.17 Simplified SHG system schematic. The femtosecond pump (red) is routed to prism-pair compressor, before being focused by a lens (L) into a temperature-stabilized MgO:PPLN crystal for second-harmonic generation. Residual fundamental light is tapped off as a local-oscillator (LO) reference, while the frequency-doubled output can be optionally compressed and routed either to an SPDC stage or to the SHG-FROG diagnostics arm. Polarization optics are omitted for clarity.

Efficient Second Harmonic Generation (SHG) is the linchpin that links the fiber-laser pump to all downstream quantum-light experiments. To maximize conversion while preserving pulse quality, the frequency doubling is produced in a type-0, 5 % MgO-doped Periodically Poled Lithium Niobate (MgO:PPLN) crystal (MSHG1550-0.5-0.3, Covesion). MgO:PPLN combines a large effective nonlinear coefficient ($d_{\text{eff}} \approx 14\,\text{pm/V}$) with the versatility of quasi-phase matching: the 0.3 mm-long chip is segmented into six gratings whose periods span 18.8 µm to 20.3 µm in 0.3 µm steps. Together with closed-loop temperature control, this discrete set of periods allows fine tuning of the phase matching condition across the full bandwidth of the femtosecond pump, maximizing conversion efficiency while and keeping the spectral and temporal quality needed for the downstream SPDC stage.

At the laser output the pulse train is first set to a well-defined linear state with a half-wave/quarter-wave plate pair (AHWP05M-1430 + AQWP05M-1430, Thorlabs), a step that minimizes Fresnel losses inside the prism-pair compressor. A second half-wave plate positioned after the compressor then rotates the beam to extraordinary polarization, matching the type-0 interaction in the MgO:PPLN crystal. The collimated beam ($1/e^2$ radius $w_0 \approx 2.16\,\mathrm{mm}$) is focused into the 0.3 mm-thick crystal by an 11 mm focal-length aspheric lens (C220TMD-C, Thorlabs), yielding an intra-crystal waist of $w \approx 10.1\,\mu\mathrm{m}$. This produces a Rayleigh range $z_R \approx 51\,\mu\mathrm{m}$ and a confocal parameter $2z_R \approx 103\,\mu\mathrm{m}$, giving a focusing parameter $l/2z_R \approx 2.9$, close to the Boyd–Kleinman optimum of 2.84 for Gaussian-beam parametric interaction [107]. The resulting tight focus maximizes nonlinear overlap while keeping spatial walk-off and dispersion negligible.

The tight focus and femtosecond pulse lengths translate to a peak intensity of about $19\,\mathrm{GW\,cm^{-2}}$ inside the crystal, more than twice the $8\,\mathrm{GW\,cm^{-2}}$ damage threshold reported by the manufacturer. To stave off photorefractive index build-up and green-induced infrared absorption, the crystal is run near the top of its specified range (≈150–200°C) in a closed-loop oven/TEC assembly (PV10 & OC3, Covesion). Elevated temperature raises the effective damage threshold and slows the onset of both degradation mechanisms [108], allowing long-term, high-flux operation without compromising conversion efficiency.

The co-propagating fundamental (1560 nm) and second-harmonic (780 nm) beams are first recollimated by an off-axis parabolic mirror (MPD00M9-P01, Thorlabs). A 750 nm short-pass filter (FESH0750, Thorlabs) suppresses green fluorescence co-generated with the SHG. The cleaned beam then meets a 950 nm dichroic mirror (DMSP950, Thorlabs), which transmits the second harmonic and reflects the pump, routing both wavelengths to the appropriate inputs of the SPDC stage. The second-harmonic beam can optionally be de-chirped with a single-prism, double-pass compressor that is functionally equivalent to a two-prism pair [109]. A 60.6°-apex SF10 prism (SF10 25.4 x 25.4 mm Ultrafast Prism, Edmund Optics) is used at its Brewster angle; the beam enters and exits the prism with ≈3 mm insertion and traverses ≈7 mm of glass on the two intermediate passes. A retro-reflector tunes the free space dispersion length to 10 cm. The geometry provides $\approx 1500\,\mathrm{fs^2}$ of positive group-delay dispersion to compress the SHG pulse to near transform limit as observed in Figure 4.20.

To pinpoint the best operating point, the temperature-dependent (T) quasi-phase matching response for a periodically poled crystal of length L, with period width Λ, and wavenumber k evaluated at wavelength λ,

$$\Phi(\lambda, T) = \mathrm{sinc}\left[\frac{L}{2}\left(k_{2\omega}(\tfrac{\lambda}{2}, T) - 2k_{\omega}(\lambda, T) - \tfrac{2\pi}{\Lambda}\right)\right], \tag{4.8}$$

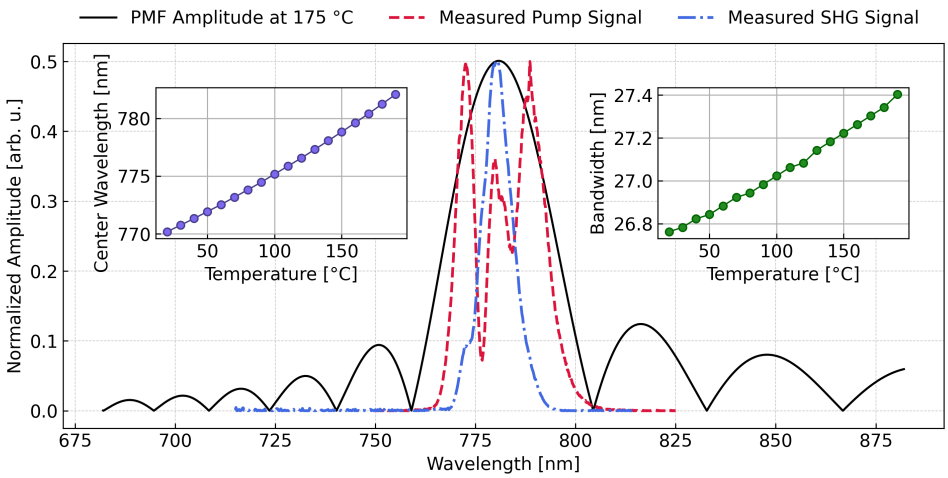

Figure 4.18 Calculated type-0 MgO:PPLN phase matching amplitude at 175 °C (black) overlaid with the measured fundamental pump spectrum (red, dashed) and its second harmonic (blue, dash-dotted) for MO pump power of 136 mW. Insets show the temperature tuning of the SHG center wavelength (left) and FWHM bandwidth (right). All curves are normalized to their respective maxima.

is computed using the MgO:PPLN Sellmeier coefficients supplied by Covesion. For each of the six grating periods (18.8–20.3 µm) the crystal temperature was swept from 150 °C to the 200 °C device limit and the overlap integral with the measured pump spectrum was evaluated. The optimum converged at 175 °C for the19.1 µm period, where $\Delta k \approx 0$ across the full pump bandwidth. Figure 4.18 overlays this sinc-shaped phase matching envelope (black) with the fundamental and second-harmonic spectra recorded at 136 mW master oscillator power (soliton described in Figures 4.9, 4.15, 4.13 and 4.16). Consistent with theory for Gaussian pulses [110], the SHG bandwidth is compressed by the factor $2\sqrt{2}$: the 17 nm RMS bandwidth of the second order soliton narrows to 5.64 nm at 780 nm. Although the theoretical phase peak sits a few nanometres short of the pump center, empirical temperature scans confirm that 175 °C yields the highest conversion efficiency, a result attributed to minor grating-period tolerances and residual dispersion in the prism compressor.

The MO pump power setting of 136 mW is not arbitrary; as mentioned in Section 4.2, it is the power that maximizes the SHG conversion efficiency. At this operating point a fundamental power of 202.087 ± 0.082 mW incident on the 0.3 mm MgO:PPLN yields 91.110 ± 0.151mW of SHG power, corresponding to an external conversion efficiency of 45.1 %. Such performance is, to our knowledge, a highpoint for broadband (∼100 fs), single-pass frequency doubling in a sub-millimeter bulk Periodically Poled Lithium Niobate (PPLN) crystal. Earlier benchmarks include ∼13 % in a 0.5 mm sample reported [111] for 100 fs pulses, and ∼42 % in an identical

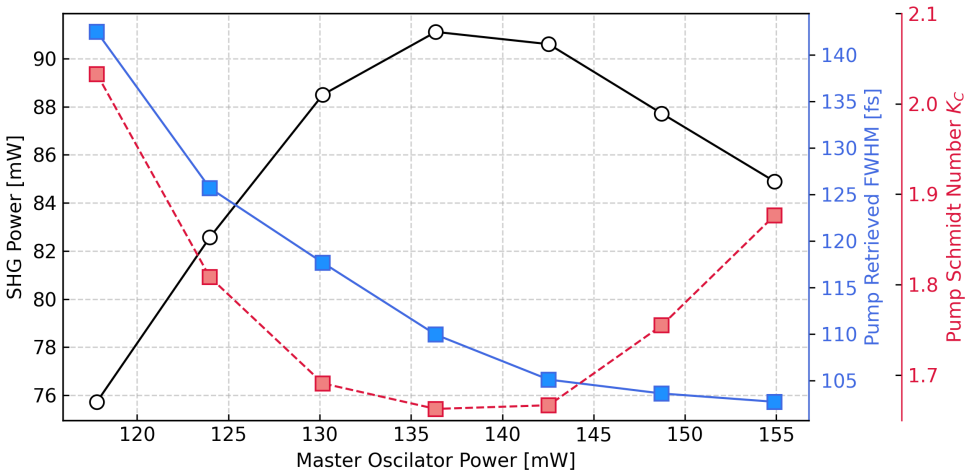

Figure 4.19 Influence of the MO pump power on second-harmonic performance. Black circles (left axis) trace the average SHG output power. The blue squares (solid line, right axis) give the pump pulse width retrieved from SHG-FROG (FWHM in fs), while the red squares (dashed, right axis) plot the chronocyclic Schmidt number K_C of the fundamental pump.

0.3 mm PPLN crystal, also pumped with an Er fiber laser, as reported in [112]. In contrast, the first-order soliton produced by the fiber source tops out at ≈25 % under ideal compression but with identical focusing conditions.

Delving deeper in the MO pump power dependence of the SHG, Figure 4.19 summarizes the pump-power scan: the average SHG output power appears in black, while the pump's chronocyclic Schmidt number K_C and FWHM pulse width are shown in red and blue, respectively. For each MO setting, the prism compressor was re-tuned to maximize SHG conversion, so any residual chirp reflects intrinsic limits rather than unequal compression. Note that the minimum pulse width extracted from the SHG-FROG is slightly longer than the value predicted by an ideal quadratic-phase compression model shown in Figure 4.14. The discrepancy is attributed to residual higher-order dispersion which the prism pair cannot fully compensate

As the MO power is raised from 118 mW to 155 mW, two clear tendencies emerge. First, the SHG curve is almost a mirror image of the K_C trace: conversion climbs steeply as the pump approaches single-mode behavior, peaks at 136 mW where K_C reaches its minimum, then falls as the state becomes increasingly multimode. Second, the pulse width shrinks monotonically with power, yet the SHG efficiency does not track that narrowing; in fact, the 780 nm output is highest well before the pulse is shortest. This contrast supports the previous statement that spectro-temporal purity, not simple brevity, is the relevant metric for broadband parametric conversion. This last point is further pushed in Section 4.3.2 below by establishing that the

single-pass SHG efficiency scales inversely with the effective chronocyclic Schmidt number, $\eta_{\mathrm{SHG}} \propto 1/K_{\mathrm{C}}^{\mathrm{eff}}$.

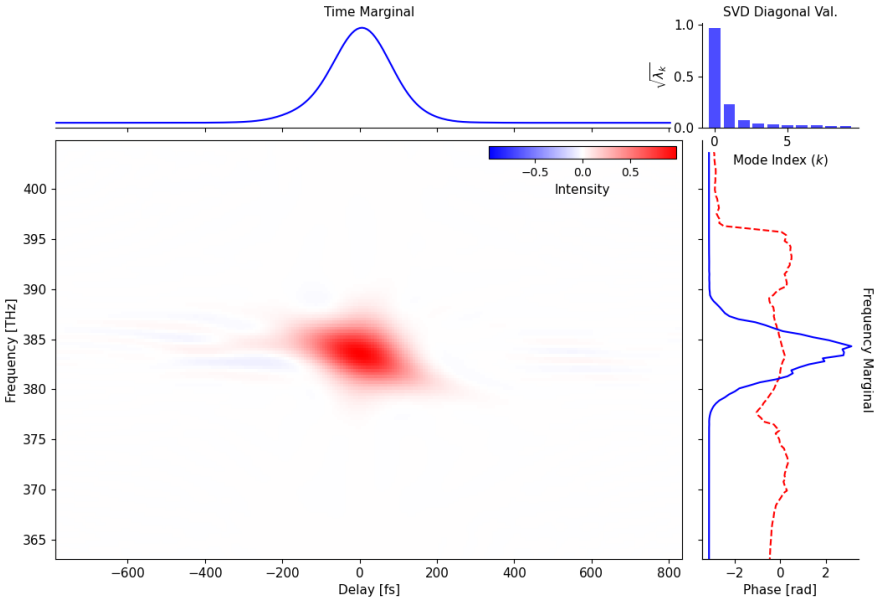

Figure 4.20 Chronocyclic Wigner analysis of the recompressed 136 mW SHG pulse. The joint time–frequency map is dominated by a single, compact lobe centered at zero delay and 385 THz (780 nm), with a slight negative tilt that betrays a small residual linear chirp. Both marginals are near-Gaussian: the temporal envelope is ≈90 fs FWHM, while the spectral width matches the expected $2\sqrt{2}$ compression of the pump. The singular-value histogram confirms high purity, with the first mode carrying $> 85\,\%$ of the energy ($K_{\mathrm{C}} \approx 1.12$).

The coupled-wave model developed in Section 4.3.2 also predicts that the SHG crystal itself acts as a spectro-temporal filter, preferentially converting the dominant Schmidt mode of the pump and thereby reducing the overall mode count. Experimental results bear this out: in Figure 4.20 the reconstructed chronocyclic Wigner function of the recompressed 136 mW SHG pulse shows a nearly single-lobed distribution, and in Figure 4.21 the uncompressed SHG Schmidt number K_{C} (blue) drops well below that of the pump (red), reaching 1.18 at the conversion optimum. Because a dedicated pulse-compression stage shaves only another ~ 0.6 off K_{C} while costing ≈20 % in throughput, it is not utilized for routine operation.

One might expect the SHG pulse to shorten in proportion to its reduced bandwidth, yet the uncompressed durations remain nearly unchanged throughout the power scan. The reason is that two competing effects cancel. First, the second field is generated instantaneously as the square of the pump envelope, which compresses the temporal variance by a factor 2 (FWHM $\rightarrow$ FWHM$/\sqrt{2}$). Second, the spectrum is simultaneously narrowed through the self-

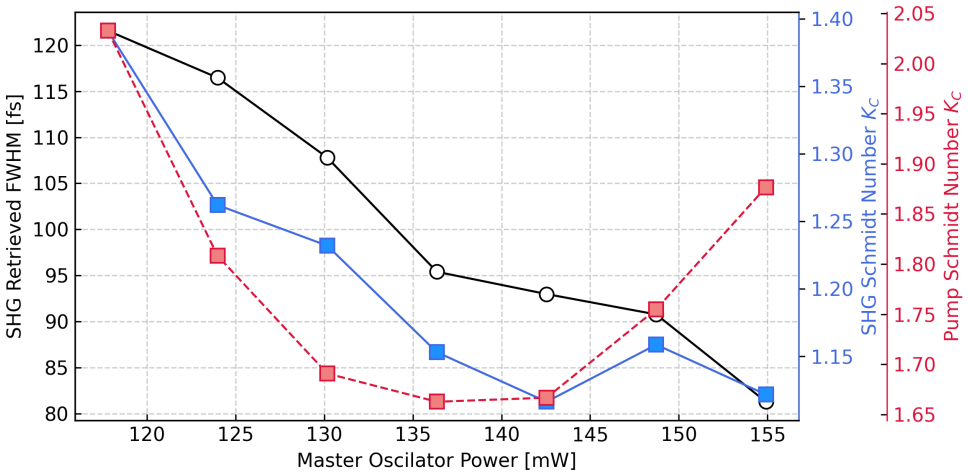

Figure 4.21 Master oscillator pump power dependence of second-harmonic pulse quality. Black circles (left axis) plot the SHG FWHM pulse durations. The corresponding chronocyclic Schmidt number K_{C} are shown for the fundamental pump (red squares, dashed, right axis) and for the generated second harmonic (blue squares, solid, right axis). The evolution of these metrics with pump power is discussed in the main text.

convolution of the pump envelope and the sinc-shaped phase matching window by essentially the same factor $\sqrt{2}$. The quadratic shortening in time therefore cancels with that halving of bandwidth required to keep the time–bandwidth product constant for a nearly transform-limited pulse, leaving the SHG FWHM almost identical to that of the pump even as the spectral width contracts.

In short, the SHG process not only supplies the SPDC seed but also self-cleans it into an almost single-mode, short pulse.

4.3.2 Coupled Wave Analysis and Connection to K_{C}

To theoretically interpret the trends uncovered above, a semi-rigorous quantitative model based on the coupled-wave formalism is developed below, linking second-harmonic conversion directly to the pump's spectro-temporal purity. Starting with the coupled–wave equation for second–harmonic generation, consider a $\chi^{(2)}$ crystal of length L pumped by a fundamental pump field with complex envelope $A_\omega(z,t)$. Under the undepleted–pump and slowly–varying–envelope approximations, the second–harmonic envelope $A_{2\omega}(z,t)$ obeys the scalar coupled–wave equation

$$\frac{\partial A_{2\omega}}{\partial z}(z,t) = i\,\kappa\,A_\omega^2(z,t)\,e^{i\Delta k z}, \tag{4.9}$$

where κ collects material constants and $\Delta k = k(2\omega) - 2k(\omega) - 2\pi/\Lambda$ is the quasi–phase–mismatch. Integrating (4.9) from $z = 0$ to $z = L$ gives

$$A_{2\omega}(L,t) \;=\; i\kappa \int_0^L dz\, A_\omega^2(0,t)\, e^{i\Delta k z} = i\kappa L\, \mathrm{sinc}\left(\frac{\Delta k L}{2}\right) e^{i\frac{\Delta k L}{2}}\, A_\omega^2(0,t), \tag{4.10}$$

so that phase–matching introduces the familiar PMF

$$\Phi(\Omega) \;\equiv\; \mathrm{sinc}\left[\frac{\Delta k(\Omega) L}{2}\right] e^{i\frac{\Delta k(\Omega) L}{2}}. \tag{4.11}$$

The conversion efficiency for the SHG process can be derived in the frequency domain through the overlap integral of the convolved spectrum with the crystal PMF. Let the pump spectrum envelope be $\tilde{A}(\Omega) = |\tilde{A}(\Omega)| e^{i\phi(\Omega)}$, with $\Omega = \omega - \omega_0$. The second–order nonlinear polarization driving the SHG at $2\omega_0$ is the self–convolution of $\tilde{A}(\Omega)$, giving in the frequency domain

$$A_{2\omega}(L) \propto \mathcal{O} \equiv \int_{-\infty}^{+\infty} \mathrm{d}\Omega\; \tilde{A}(\Omega)\tilde{A}(-\Omega)\Phi(\Omega). \tag{4.12}$$

The SHG conversion efficiency therefore scales as

$$\eta_{\mathrm{SHG}} \propto |\mathcal{O}|^2 \tag{4.13}$$

Equation (4.12) is a bilinear form that can be rewritten with two independent frequency variables (see Annex B for more details):

$$\mathcal{O} = \iint_{-\infty}^{+\infty} d\Omega_1 d\Omega_2\; \tilde{A}(\Omega_1)\tilde{A}(\Omega_2)\, \underbrace{\left[\Phi\left(\tfrac{\Omega_1 - \Omega_2}{2}\right)\delta(\Omega_1 + \Omega_2)\right]}_{K(\Omega_1,\Omega_2)}. \tag{4.14}$$

The symmetric crystal kernel

$$K(\Omega_1,\Omega_2) = \Phi\left[\frac{\Omega_1 - \Omega_2}{2}\right]\delta(\Omega_1 + \Omega_2) \tag{4.15}$$

acts as a Hermitian operator on the pump spectrum. Because K is Hermitian and positive–semidefinite by construction, it admits a Schmidt decomposition of the form

$$K(\Omega_1,\Omega_2) = \sum_n \lambda_n\, u_n(\Omega_1) u_n^*(\Omega_2), \tag{4.16}$$

where u_n are orthonormal eigenmodes and λ_n their eigenvalues ($\lambda_n \geq 0$). Expanding $\tilde{A}(\Omega) =$

$\sum_n a_n u_n(\Omega)$ with $a_n = \langle u_n|A\rangle$, the overlap integral can be recast as

$$\mathcal{O} = \sum_n \lambda_n |a_n|^2 \qquad , \qquad |\mathcal{O}|^2 \leq \sum_n \lambda_n^2 |a_n|^4 \equiv S_2. \tag{4.17}$$

The last inequality follows from Cauchy–Schwarz inequality.

Equation (4.17) can be linked to the chronocyclic Schmidt number. Defining the pump density matrix,

$$\rho(\Omega_1, \Omega_2) = \tilde{A}(\Omega_1)\tilde{A}^*(\Omega_2), \tag{4.18}$$

and multiplying it element-wise (Hadamard product) by the crystal kernel K yields the composite kernel

$$\tilde{\rho}(\Omega_1, \Omega_2) = \rho(\Omega_1, \Omega_2)\, K(\Omega_1, \Omega_2) = \tilde{A}(\Omega_1)\tilde{A}^*(\Omega_2)\, \Phi\left(\frac{\Omega_1 - \Omega_2}{2}\right)\, \delta(\Omega_1 + \Omega_2). \tag{4.19}$$

Taking the sum–difference variables $\Sigma = (\Omega_1 + \Omega_2)/2$ and $\Delta = (\Omega_1 - \Omega_2)/2$, and performing the inverse Fourier transform in the sum coordinate ($\Sigma \to t$) produces the effective chronocyclic Wigner function,

$$\begin{aligned} W_{\text{eff}}(t, \Omega) &= \frac{1}{\sqrt{2\pi}} \int_{-\infty}^{+\infty} d\Sigma\; \tilde{\rho}\,(\Sigma + \Delta, \Sigma - \Delta)\; e^{-i2\Sigma t}\Big|_{\Delta=\Omega} \\ &= \frac{1}{\sqrt{2\pi}} \int_{-\infty}^{+\infty} d\Delta_\Omega\; \Phi(\Delta_\Omega)\, \tilde{A}\left(\Omega + \frac{\Delta_\Omega}{2}\right) \tilde{A}^*\left(-\Omega + \frac{\Delta_\Omega}{2}\right)\, e^{-i\Delta_\Omega t}, \end{aligned} \tag{4.20}$$

with $\Delta_\Omega = \Omega_1 - \Omega_2$, matching the form of (3.5). Equation (4.20) shows that W_{eff} is the pump Wigner function filtered along its anti-diagonal by the phase matching envelope Φ, retaining only frequency pairs that satisfy energy conservation.

The effective chronocyclic Schmidt number can be retrieved in the usual way. Because the Hadamard product leaves the right–left basis of the decomposition of K intact, the composite kernel (4.19) has the same eigen-modes as K but rescaled eigen-values

$$\tilde{\lambda}_n \;=\; \lambda_n\, |a_n|^2. \tag{4.21}$$

The Wigner transform ((4.20)) is unitary, so its singular-value spectrum is also $\{\tilde{\lambda}_n\}$. The corresponding chronocyclic Schmidt number is therefore

$$K_{\text{C}}^{\text{eff}} = \frac{\left(\sum_n \tilde{\lambda}_n\right)^2}{\sum_n \tilde{\lambda}_n^2} = \frac{S_1^2}{S_2}, \qquad S_1 = \sum_n \tilde{\lambda}_n,\; S_2 = \sum_n \tilde{\lambda}_n^2. \tag{4.22}$$

Combining (4.13), (4.17) and (4.22) gives the general bound

$$\eta_{\mathrm{SHG}} \propto |\mathcal{O}|^2 \leq S_2 = \frac{S_1^2}{K_{\mathrm{C}}^{\mathrm{eff}}}. \tag{4.23}$$

Since $\tilde{\lambda}_n$ combines the crystal spectrum λ_n with the pump modal weights ($|a_n|^2$), pulse-shaping, i.e modifying K_{C}, can impact $K_{\mathrm{C}}^{\mathrm{eff}}$ by redistributing the weights a_n even though the $\{\lambda_n\}$ themselves are fixed by the crystal. Therefore, minimizing the chronocyclic Schmidt number K_{CW} maximizes the upper bound on the SHG conversion efficiency, in agreement with the experimental trends. The absolute optimum ($K_{\mathrm{CW}} \to 1$) is reached when the pump spectrum occupies a single eigen–mode u_0, i.e. when $a_0 = 1$ and $a_{n>0} = 0$.

Squaring the pump envelope, to which the SHG field is proportional, preferentially selects frequency pairs that share the same eigen-mode index. At the same time, the sinc-shaped phase matching filter Φ suppresses side-lobe frequencies that would otherwise feed higher-order modes. Together, these operations funnel nearly all weight into the leading composite eigen-value $\tilde{\lambda}_0$; the higher-order $\tilde{\lambda}_{n>0}$ become vanishingly small, the effective Schmidt number $K_{\mathrm{CW}}^{\mathrm{eff}}$ approaches unity, and multimode artifacts, tilt, side-bands, and asymmetric pedestals, disappear. This theoretical picture matches the measurements: the recorded SHG spectra show a single, well-defined lobe with a substantially cleaner background than the pump, confirming that mode squeezing in the nonlinear conversion stage is responsible for the experimentally observed spectral purity.

4.4 Pump Improvement

Although the femtosecond pulse train emerging from the fiber oscillator, and its frequency-doubled second harmonic, already provide a working SPDC pump and self-reference, the system still offers considerable headroom for refinement. The discussion that follows therefore reviews a set of targeted engineering adjustments designed to extract higher pulse energies, cleaner spectral and temporal profiles, and superior conversion efficiency.

Starting from the MO cavity, the present configuration carries $\approx -66\,900\,\mathrm{fs}^2$ of anomalous GDD from relatively long component PM1550 tails. Trimming these tails until the cavity dispersion sits just below zero and splicing in an extra 10 to 20 cm of Er-doped fiber can shift the laser from an over-compressed soliton regime to a stretched-pulse regime; this configuration can suppress soliton fission, broadens the stable pump-power window, and boosts pulse energy by 20–30 % [113]. A complementary upgrade is to tap the weak (≈ -40dB) crosstalk leaking from the unused port of the circulator to detect the carrier-envelope offset frequency;

feeding this beat back to the pump-diode current closes a simple yet effective carrier envelope phase-stabilization loop, as already demonstrated in all-PM Er-fiber frequency combs [114]. Finally, for long-term environmental robustness, the entire oscillator can be bonded to an actively temperature-regulated aluminum base-plate. The exposed fiber components on the upper side can then be over-moulded with a low-modulus silicone potting compound; the cured silicone forms a hermetic barrier that blocks humidity (which has a strong effect on the SAM) and dust while damping mechanical stress. Because only the top side is encapsulated, the underside remains in direct contact with the base plate, preserving efficient thermal regulation.

At the EDFA stage, the strong positive chirp and onset of spectral break-up indicates strong positive nonlinear phase accumulation from SPM compounded by the normal dispersion of the Er-doped gain fiber [115]. This can be adressed by increasing the anomalous-dispersion PM1550 pre-chirp fiber before the amplifier: about 3 m would impose a counter-balancing quadratic phase [116, 117]. Downstream, the output pigtail can be trimmed or replaced by a short photonic-crystal fiber with known GDD and TOD, ensuring the pulses reach the SHG stage at ideal compression when accounting for all the intermediate optics without the need for a pulse compressor. For dynamic optimization, an in-line acousto-optic programmable dispersive filter can apply a parabolic phase so the pulse evolves self-similarly through the amplifier [118]; the amplifier-similariton regime is well-known to suppress modulation instability and support higher pulse energies than conventional chirped pulse amplification schemes [116, 119–121]. Collectively, these measures could stabilize the spectrum, and reclaim roughly 20–30 % more usable pulse energy.

Finally, a simple solution to increase the SHG conversion efficiency would be to use a longer crystal. Because the MO now runs in the second-order soliton regime, its 16 nm bandwidth fits the acceptance bandwidth of a longer nonlinear crystal. Swapping the present 0.3 mm MgO:PPLN for a 0.5 mm device nearly doubles the interaction length and is expected to raise single-pass conversion by roughly 15–20 % [122]. Beyond this, once the fiber dispersion is fully tamed, the logical next step is to replace the free-space crystal with a fiber-pigtailed ridge-waveguide PPLN: these modules routinely deliver overall CW conversion of 58–70% at the watt level [123], while state-of-the-art nanophotonic designs have reached over 53% conversion efficiency from 1550 to 775 nm [124].

CHAPTER 5 BRIGHT TYPE-II SPDC GENERATION

This final chapter reports initial observations of Spontaneous Parametric Down-Conversion (SPDC) generated in a Periodically Poled Lithium Niobate (PPLN) waveguide using the femtosecond source developed in chapter 4. The SPDC PPLN crystal is first pre-characterized with classical light, exploiting the fact that the inverse SHG process shares the same nonlinear tensor element and phase-matching conditions as type-II SPDC. The femtosecond 1560 nm fundamental pump beam described in Chapter 4.2 was linearly polarized at $\pm 45^\circ$ and was focused into the PPLN, and the SHG yield was mapped as a function of grating period and oven temperature. The optimum parameters were found to be a 10 µm poling period at 135 °C, from which reciprocal-process arguments predict a pair-production efficiency of roughly 5×10^5 photons/s in the low-gain regime.

Armed with these settings, the crystal was pumped with the 780 nm SHG engineered pump described in Section 4.3 and the down-converted light was imaged onto an InGaAs camera. Clear, collinear emission was recorded on both orthogonal polarization channels, corresponding to a brightness of $\sim 6.9 \times 10^6$ signal–idler pairs per second. These preliminary results validate the phase-matching model and set the stage for high-signal-to-noise coincidence and heralding experiments.

5.1 Pre-Characterisation of the SPDC Crystal

Degenerate, type-II SPDC spontaneously converts a single, high-intensity pump photon into a pair of lower-energy daughter photons that are orthogonally polarized and share the pump energy equally. Because the ordinary and extraordinary polarizations experience different refractive indices, the quasi-phase-matching grating must be engineered with this birefringence in mind. The resulting Phase Matching Function (PMF), defined in (4.8), governs the degeneracy of photon pairs, dictating both their center wavelength and bandwidth.

The nonlinear medium used to generate SPDC in this project is a 0.5 mm long, MgO-doped Periodically Poled Lithium Niobate (MgO:PPLN) chip featuring five grating periods from 9.20 µm to 10.0 µm in 0.20 µm steps (MSHG1180-0.5-40 780/1560 AR, Covesion). Focusing the SHG femtosecond pump of Chapter 4 into the waveguide produces peak intensities that approach the crystal's damage threshold of 8 GW cm^{-2}; to mitigate photo-refractive damage blue-induced infrared absorption, the oven temperature is therefore maintained above 100 °C throughout.

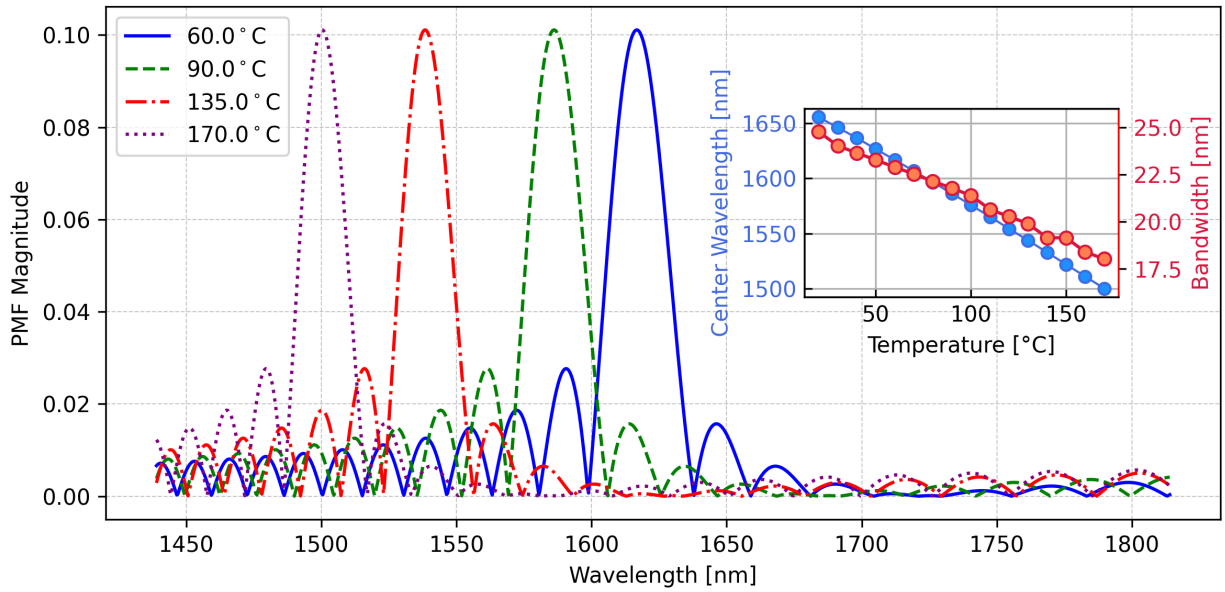

Figure 5.1 Calculated phase-matching function magnitude for the 10 µm period, type-II PPLN crystal at four representative oven temperatures. As the temperature rises, the PMF peak blue-shifts and narrows, with the model predicting its maximum efficiency near 115 °C. In practice, the strongest SHG/SPDC response was observed at 135 °C, a 20 °C offset that likely arises from uncertainties in the Sellmeier coefficients, waveguide dispersion, or slight deviations in the fabricated grating period.

A numerical temperature–period sweep based on Covesion's Sellmeier dispersion data shows that the PMF attains its maximum for the 10 µm domain at 115 °C, yielding collinear, degenerate SPDC at 1560 nm. The resulting tuning curves are plotted in Figure 5.1. The SPDC peak shifts and narrows about an order of magnitude more rapidly with temperature than the SHG tuning shown earlier in Figure 4.18: about 0.9 nm/°C for SPDC versus 0.07 nm/°C for SHG, and the bandwidth contracts at a comparable rate.

The increased sensitivity is a direct consequence of birefringent phase matching. In SHG the pump and harmonic waves both sample the same polarization branch, so a temperature change perturbs the mismatch $k_{2\omega} - 2k_{\omega}$ only via the ordinary (or extraordinary) thermo-optic coefficient. In type-II SPDC, however, the signal and idler occupy orthogonal branches, and the mismatch $k_p - k_s - k_i$ depends on the difference of the effective refractive indexes $n_e(T) - n_o(T)$; dn_e/dT is around 20 times dn_o/dT in lithium niobate [125], amplifying $\partial\Delta k/\partial T$ and therefore the tuning of both center wavelength and bandwidth.

In practice the true phase-matching optimum can drift far from its theoretical prediction, with offsets as large as 70 °C having been reported for lithium-niobate devices [126]. The

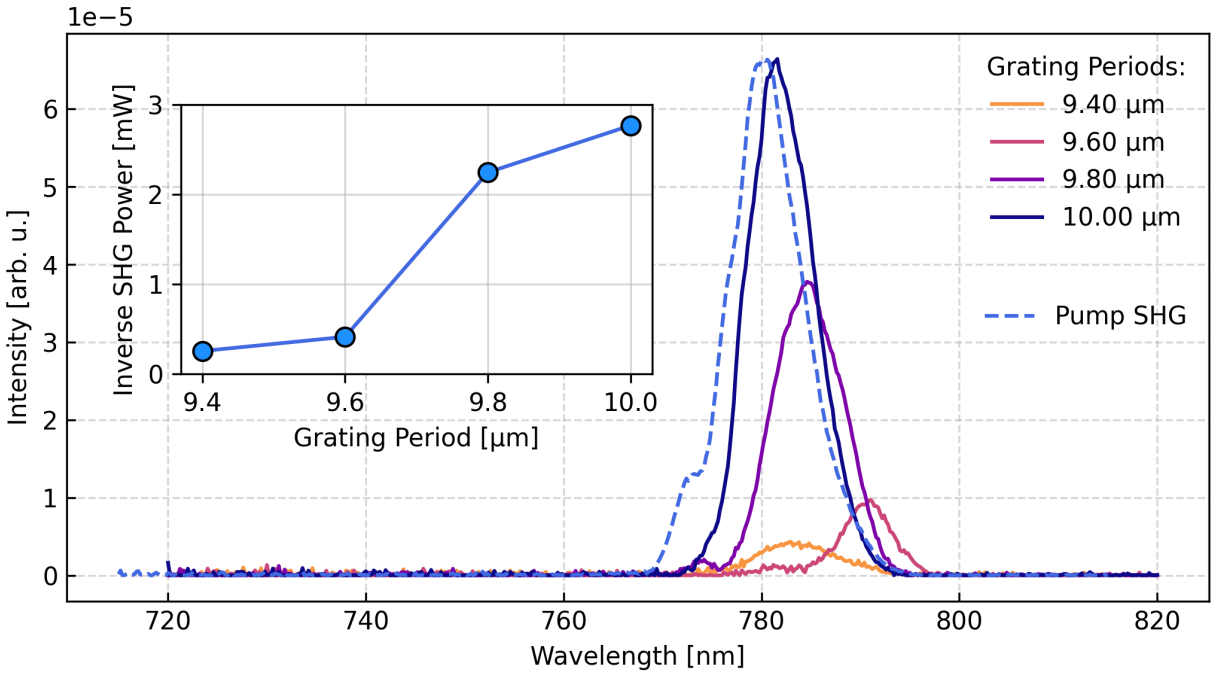

Figure 5.2 Measured second-harmonic spectra and average powers obtained by pumping the SPDC PPLN crystal in the reverse direction (fundamental at 1560 nm, MO pump power of 116 mW). Four grating periods were probed. The inset plots the corresponding SHG powers, 0.28, 0.32, 2.3 and 2.8 mW, respectively, highlighting the increase in conversion efficiency with period. The blue dashed line is the reference SHG spectrum produced in a purpose-built SHG PPLN (same pump power), included to show the target phase-matching wavelength and baseline bandwidth.

mismatch stems from uncertainty in Sellmeier coefficients, finite fabrication tolerances in the grating period, and small errors in the poling duty cycle. Rather than rely solely on theory, the crystal is characterized using the inverse SHG process to its SPDC counterpart. Recall that in PPLN, e-polarized type-II interaction is governed by the d_{31} element of the non-linear $\chi^{(2)}$ susceptibility tensor. Injecting 1560 nm light that is linearly polarized at $\pm 45°$ excites the same non-linear tensor elements and obeys the same quasi-phase-matching condition as type-II SPDC, so maximizing the SHG yield automatically reveals the optimal temperature–period pair for down-conversion while providing an experimental benchmark for the conversion efficiency.

To carry out the measurement the SPDC PPLN replaces the dedicated SHG MgO:PPLN in the setup of Figure 4.17. The pump is rotated with a half-wave plate, and the focusing optic is swapped for a 15.3 mm aspheric lens (C260TMD-C, Thorlabs) that satisfies the Boyd-Kleinman focusing condition with a confocal-parameter criterion of 2.84 [107]. For the four

longest grating periods (the 9.2 µm period provides negligible power and it optimum was out of the temperature range), the oven temperature is swept from 100 °C to 200 °C, and at the temperature giving the highest SHG power the spectrum is recorded. The peak powers and corresponding spectra are summarized in Figure 5.2, alongside the reference spectrum from the purpose-designed SHG crystal (Section 4.3).

The temperature sweep confirms that the longest grating period, 10 µm, yields the highest conversion efficiency, exactly as predicted, but the optimum occurs at 135 °C, about 20 °C higher than the Sellmeier-based estimate. At this setting the "reverse" SHG spectrum generated in the SPDC crystal almost perfectly overlays the reference SHG spectrum from the dedicated SHG PPLN, demonstrating excellent spectral mode matching (residual sub-nanometer detuning can be trimmed with a slight oven adjustment during SPDC operation). The peak back-converted SHG power is 2.25 mW for an incident fundamental power of 202 mW, corresponding to an external conversion efficiency of roughly 1.1%.

The pair-production efficiency can be estimated by returning to the coupled-wave equations in the undepleted-pump, slowly-varying-envelope limit. Let $A_{2\omega}(z)$ denote the complex envelope of the second-harmonic field at position z in the PPLN, and let $A_{\parallel}(z)$ and $A_{\perp}(z)$ be the fundamental envelopes launched with equal power and linear polarizations at $\pm 45^{\circ}$ with respect to the crystal axes. With the grating period and oven temperature adjusted so that the residual phase mismatch is negligible $\left(e^{i\Delta kz} \simeq 1\right)$, equation (4.9) simplifies to

$$\frac{\partial A_{2\omega}}{\partial z} = i\,\kappa\, A_{\parallel} A_{\perp}, \tag{5.1}$$

where κ is the nonlinear coupling constant introduced earlier and incorporates d_{eff}, the refractive indices, and the effective mode area. Integration of (5.1) over the crystal length L yields $A_{2\omega}(L) = i\kappa L A_{\parallel} A_{\perp}$. Rewriting the field amplitudes in terms of photon-flux gives

$$\langle n_{2\omega}(z)\rangle = \kappa^2 z^2\, \langle n_{\parallel}\rangle \langle n_{\perp}\rangle. \tag{5.2}$$

Expressed in terms of average SHG power $\bar{P}_2 = \hbar\omega_2 f_{\text{rep}} \langle n_2\rangle$ and equal pump powers $\bar{P}_1 = \hbar\omega_1 f_{\text{rep}}\langle n_{\parallel}\rangle = \hbar\omega_1 f_{\text{rep}}\langle n_{\perp}\rangle$, a single calibration constant can be extracted

$$\Gamma = \frac{\kappa^2}{4\hbar\omega f_{\text{rep}}} = \frac{\bar{P}_2}{\bar{P}_1^2} \tag{5.3}$$

which is measured in the high-power inverse SHG experiment described above.

To translate the SHG calibration into a quantitative prediction for pair production in the

low-gain regime, the pump is treated classically and the signal and idler fields are promoted to operators. With the residual phase mismatch suppressed ($\Delta k \approx 0$), the coupled Heisenberg equations for a collinear, type-II interaction reduce to

$$\frac{\partial}{\partial z}\begin{bmatrix}\hat{a}_{\parallel}(z)\\ \hat{a}^{\dagger}_{\perp}(z)\end{bmatrix} = i\kappa\, A_{2\omega}\begin{bmatrix}0 & 1\\ -1 & 0\end{bmatrix}\begin{bmatrix}\hat{a}_{\parallel}(z)\\ \hat{a}^{\dagger}_{\perp}(z)\end{bmatrix}, \tag{5.4}$$

where $\hat{a}_{\parallel}$ and $\hat{a}_{\perp}$ annihilate the orthogonally polarized, degenerate daughter modes. Solving Eq. (5.4) yields the familiar twin-beam statistics

$$\langle \hat{n}_{\parallel}(L)\rangle = \langle \hat{n}_{\perp}(L)\rangle = \sinh^2(g)\,, \qquad g \equiv \kappa L\,|A_{2\omega}|, \tag{5.5}$$

and, in the low-gain limit $g \ll 1$, the pair probability per pulse simplifies to

$$p_{\text{pair}} \simeq g^2 = \kappa^2 L^2 |A_{2\omega}|^2. \tag{5.6}$$

Relating the second-harmonic field to the measured average SHG power through $\bar{P}_2 = \kappa \bar{P}_1^2$ shows that $p_{\text{pair}} = \kappa \bar{P}_2$. In the calibration run, $\bar{P}_2 = 2.25\,\text{mW}$ of SHG power was obtained from $\bar{P}_1 = 202\,\text{mW}$ of input power, giving $\kappa = 5.51 \times 10^{-5}\ \text{mW}^{-1}$. For the SPDC experiment described next, the intra-crystal second-harmonic pump is $\bar{P}_2 = 70.1\,\text{mW}$, so the expected pair probability is $p_{\text{pair}} = \kappa \bar{P}_2 = 3.87 \times 10^{-3}$ per pulse. At a repetition rate of $f_{\text{rep}} = 121.6$ MHz, this corresponds to a single-pass brightness of $N_{\text{pairs}} \approx 4.7 \times 10^5$ signal–idler pairs per second.

5.2 Preliminary Results

Producing and detecting SPDC proved to be the most demanding milestone of this work. Stable pair generation was achieved only after iterative optimization of the femtosecond pump, boosting average power, reshaping the pulse spectro-temporally, and after inverse-SHG characterization of the MgO:PPLN identified the true phase-matching window. The results reported below are therefore a first-generation proof-of-concept that future runs will refine. In practice, success came not from a single perfect alignment (although crucial) but from a systematic feedback loop in which parameters like focusing, compressor settings, collection optics and laser operating conditions were repeatedly tweaked until photon pairs emerged. For perspective, establishing a reproducible, collinear type-II SPDC signal required nearly two years of incremental adjustments after the laser became fully operational.

The most reliable pair generation was obtained under the following conditions, as shown in

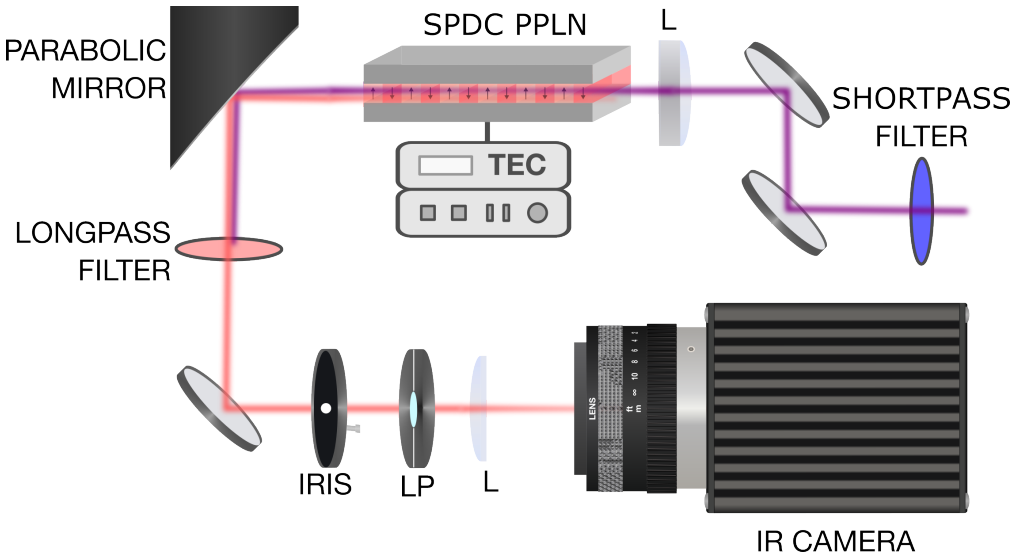

Figure 5.3 Simplified schematic of the preliminary SPDC experiment. Filtered 780 nm pump (purple) is focused into a temperature-controlled PPLN. The collinear 1560 nm SPDC output (red) is collimated, passed through a long-pass filter and iris, polarized by a linear polarizer (LP), and imaged on an infrared camera. Polarization optics are omitted for clarity.

Figure 5.3. The mode-locked fiber laser was run at an MO pump power of 136 mW; the EDFA was set to full output and the pulse compressor tuned to 111.6 fs. This produced optimized second-harmonic pulses of 101.6 fs and 70.1 mW of average power injected in the PPLN (see Section 4.3). The extraordinarily polarized SHG, not recompressed for maximal power, was sent directly to the SPDC stage. Residual 1560 nm light was removed by the dichroic of the SHG setup followed by two short-pass filters (FESH0850, Thorlabs). The resulting 2.5 mm diameter beam ($M^2 \approx 1.2$) was focused into the temperature-controlled PPLN with a 15.3 mm aspheric lens (C260TMD-B, Thorlabs). The calculated waist was 14.2 µm, giving a confocal parameter of 171 µm; the crystal-length-to-confocal-parameter ratio of 2.9 is close to the Boyd–Kleinman optimum [107].

The crystal was mounted in a Covesion oven (PV10 & OC3) and held at the empirically optimized 137 °C. After the crystal, an off-axis parabolic mirror (MPD119-P01, Thorlabs) collimated the mixed 780/1560 nm beam. A long-pass filter (FELH1500, Thorlabs) blocked the pump; the down-converted light then passed an iris and a rotatable linear polarizer (LPVIS050-MP2, Thorlabs) before being imaged onto a Goldeye G-008 SWIR camera (Allied Vision) (gain = 1) with a 49.8 mm plano-convex lens (LA1131-C, Thorlabs).

Beam coupling was optimized by maximizing the in-crystal second-harmonic light at 390 nm, a convenient real-time proxy for correct phase matching. Because the type-II grating is engineered for an extraordinary-polarized pump, even a slight vertical tilt of the PPLN

disrupts the birefringent phase-matching condition; the 390 nm signal drops almost instantly when this tilt is off, providing a highly sensitive alignment cue.

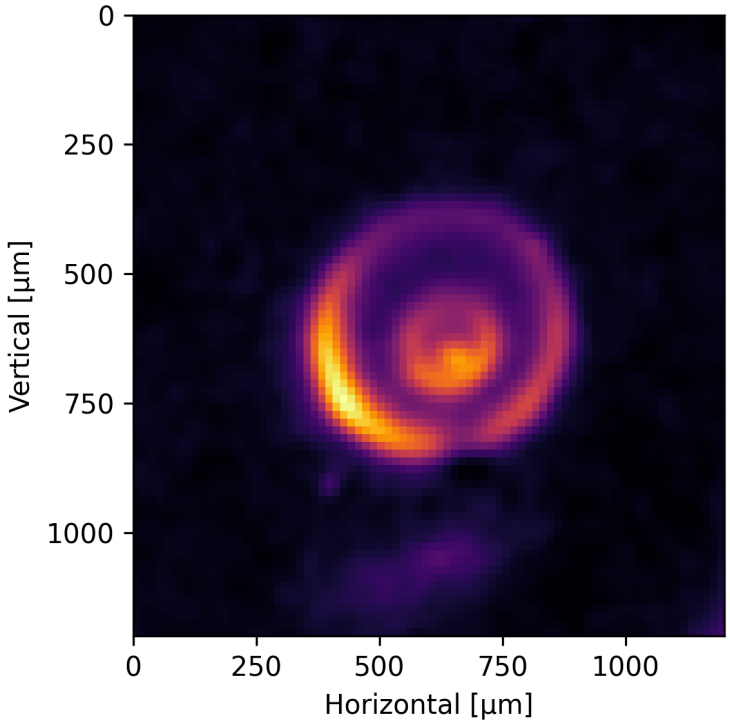

Figure 5.4 Far-field image of the broadband Cherenkov-type 0 SPDC emitted by the MgO:PPLN when no spatial filtering is applied. The outer annulus traces the non-collinear phase-matching cone; its brightest sector (lower left outer quadrant) corresponds to photon wavelengths > 1500 nm, whereas the remainder of the ring becomes visible only when the 1500 nm long-pass filter is replaced by a 1000 nm one. The two fainter, concentric inner rings are attributed to back-reflections between the crystal facets and downstream optics. Color scale: normalized camera counts; axes give camera-plane coordinates in micrometers.

Initially only a bright extraordinary-polariùed quarter-ring appeared on the InGaAs camera, resembling the non-collinear cone typical of type-I SPDC. Replacing the 1500 nm long-pass with a broader 1000 nm filter revealed a complete annulus (Figure 5.4). The pattern persisted on all periods, and more faintly when the pump was tuned off-period, indicating that the emission is not governed by the quasi-phase-matched type-II interaction but by a different mechanism.

The annulus is suspected to be non-linear Cherenkov–type-0 SPDC, not the quasi-phase-matched type-II process targeted in the design. Whilst the e-polarized type-II interaction is governed by the d_{31} tensor element of $\chi^{(2)}$ in $LiNbO_3$, type-0 interaction leverages the d_{33} element. In a PPLN the sign flip of the d_{33} tensor at each domain wall launches a polarization

wave that travels at the pump's phase velocity; when that super-luminal source outruns certain down-converted modes it radiates at the Cherenkov angle $\cos\theta = n_p/n_{s,i}$ [127]. Because only the extraordinary-polarized pump couples to d_{33}, the emission inherits the same extraordinary polarization and fans out over a broad type-I cone, often wider than 40°, producing the bright annulus seen on the camera. Although this radiation still satisfies energy conservation and originates from the same $\chi^{(2)}$ nonlinearity (and is therefore formally SPDC), its phase matching is governed by the Cherenkov condition rather than by the engineered quasi phase matched grating, making it broadband, less sensitive to period detuning, and routinely reported as parasitic rings in PPLN [128].

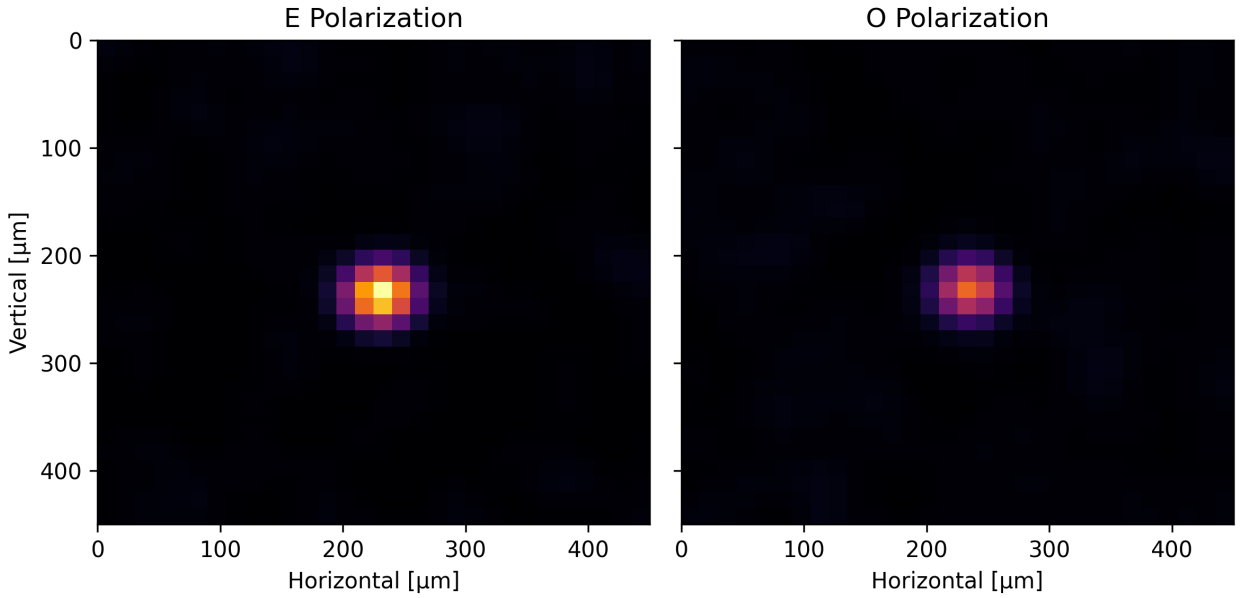

Figure 5.5 Spatial profiles of the collinear type-II SPDC measured on the InGaAs camera after polarisation filtering. Left: extraordinary (e) component; right: ordinary (o) component. The e-polarized spot is ~ 1.5 times brighter, a disparity attributed to a faint residual contribution from nonlinear Cherenkov radiation that is not fully removed by the spectral filtering.

After the wide angle Cherenkov cone was cropped with an iris, two clean, near-collinear spots remained on the InGaAs camera, one extraordinary-polarized (vertical rotated linear polarizer) and one ordinary-polarized (horizontal rotated linear polarizer) shown in Figure 5.5. From the camera's saturation calibration at gain = 1, these correspond to 5.2×10^6 photons/s in the e-channel (6.7×10^{-13}W) and 3.4×10^6 photons/second in the ordinary channel (4.4×10^{-13}W).

The ≈ 1.5 times brightness excess of the e-spot is attributed to a small leak of extraordinary-polarized Cherenkov emission that survives the spatial filtering. This Cherenkov channel is

measured to be $\approx 20\times$ brighter than the collinear type-II signal, in line with its being driven by the d_{33} coefficient ($\sim 25\,\mathrm{pm\,V^{-1}}$), which is roughly six times larger than the d_{31} coefficient ($\sim 4\,\mathrm{pm\,V^{-1}}$) governing the type-II process [129].

To isolate the genuine type-II signal, off-period frames (crystal detuned from the 10 µm grating) were subtracted from on-period frames, removing residual 1560 nm pump and camera dark noise below a fixed threshold. Consistent with the Sellmeier model and crystal pre-characterization, the collinear emission is prominent only on the 10 µm grating; it is barely detectable on the 9.8 µm and 9.6 µm grating periods and vanishes on shorter periods. Rotating the pump away from pure extraordinary polarization immediately quenches the count rate, confirming that the interaction proceeds via the d_{31} tensor element. Assuming each detected o-photon has an e-partner, the ordinary channel sets a conservative lower bound of 6.9×10^6 paired photons per second, about 0.03 pairs per pulse at the 121.6 MHz repetition rate.

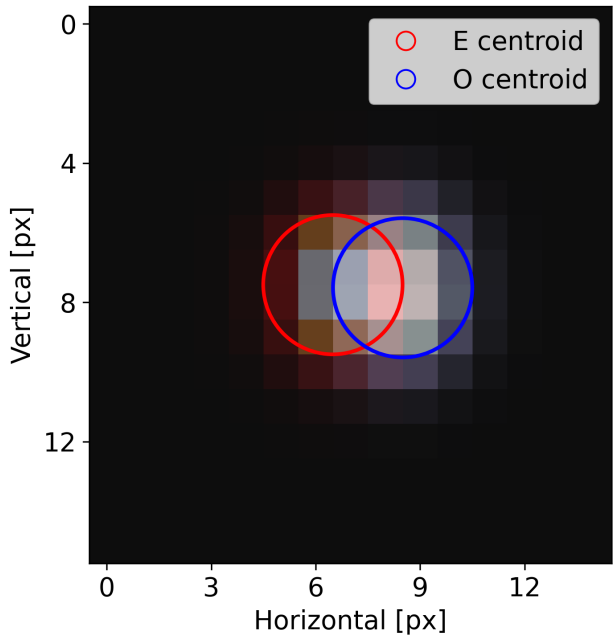

Figure 5.6 Overlay of extraordinary (red) and ordinary (blue) SPDC spots; circles mark the intensity-weighted centroids. The measured lateral separation of ≈ 30 µm matches the Poynting-vector walk-off predicted for a 0.5 mm MgO:PPLN crystal followed by the 25 mm collimator, and 50 mm imaging lens.

The final SPDC characteristic that is observed for the type-II emission is beam walk-off, the angular divergence between the Poynting vectors of extraordinary and ordinary waves in a birefringent crystals like PPLN. It is manifested here as a small lateral displacement between the two SPDC spots when the linear polarizer is removed. Figure 5.6 shows a measured separation of ≈30 µm. Contrasting this to what is expected: inside the 0.5 mm

MgO:PPLN the extraordinary ray departs from the ordinary by the walk-off angle

$$\rho_{\text{int}} \approx \arctan\Big[(n_o^2 - n_e^2)/n_e^2\Big] \simeq 1.9^\circ \; (3.3 \times 10^{-2}\,\text{rad}), \tag{5.7}$$

producing an exit-face offset of

$$\Delta x_{\text{exit}} = L \tan \rho_{\text{int}} \approx 0.5\,\text{mm} \times 0.033 \approx 16\,\mu\text{m}. \tag{5.8}$$

Placed at the focus of the 25.4-mm off-axis parabolic mirror, this shift becomes a collimation angle

$$\theta_{\text{ext}} = \frac{\Delta x_{\text{exit}}}{f_{\text{OAP}}} \approx \frac{16\,\mu\text{m}}{25.4\text{ mm}} \approx 6.3 \times 10^{-4}\,\text{rad}. \tag{5.9}$$

The $f_{\text{lens}} = 50$ mm imaging lens then maps that angle back to a focal-plane displacement

$$\Delta x_{\text{focus}} = f_{\text{lens}} \theta_{\text{ext}} \approx 50\text{ mm} \times 6.3 \times 10^{-4} \approx 32\,\mu\text{m}, \tag{5.10}$$

consistent with the ≈30 µm offset observed experimentally.

5.3 Discussion

The prototype source delivers ≈ 9.8×10^4 photons/s/mW (≈ 6.9×10^6 photons/s from 70.1 mW intra-crystal pump), below the stated brightness benchmark of 10^6 pairs/s/mW (Section 2). The yield is nonetheless higher than predicted from the inverse-SHG calibration, suggesting that a faint, spectrally broad leakage of the 1560 nm fundamental pump may seed the process or that local gain is larger than assumed. No entanglement metrics; visibility, fidelity, or joint-spectral purity, have yet been taken, so the quantum quality of the pairs remains to be verified. Even so, the experiment constitutes, to our knowledge, the first demonstration of femtosecond, Er-fiber-pumped, type-II SPDC in MgO:PPLN and therefore establishes a workable starting point.

Several straightforward upgrades should move the source beyond the 10^6 pairs/s/mW threshold. As with the SHG case, because the laser operates as a second-order soliton and therefor the pump spectrum is narrower than initially anticipated; replacing the 0.5 mm PPLN with a 1 mm one would double the gain. Further, a waveguide implementation such as a ridge or proton-exchanged PPLN would increase mode confinement, could boost conversion efficiency by an order of magnitude, and simplify fiber coupling. The SHG pulses were also left chirped to maximize average power. Pre-chirping the fundamental beam so that the second harmonic arrives transform-limited at the SPDC crystal should raise the peak intensity and hence the

pair rate without the added losses of recompression.

Beyond length-scaling and wave-guiding, several advanced architectures could push the source solidly into the high-gain ($> 10^6$ pairs/s/mW) regime. Resonant or multi-pass pumping is the most direct lever. A double-pass geometry, or, a polarization-Sagnac loop in which the crystal sits inside a low-loss cavity and the pump retraces its path, can increase the nonlinear interaction length without sacrificing bandwidth. Telecom-band Sagnac sources based on periodically poled crystals have already demonstrated order-of-magnitude brightness enhancements while maintaining excellent phase stability and entanglement fidelity [31, 130, 131], whilst a double pass configuration increases brightness while reducing the mode-count of the generated SPDC [46]. More generally, cavity-enhanced SPDC scales the pair flux as $F/(1-R)^2$ (with R the cavity reflectivity) and can reach the sub-threshold high-gain regime where stimulated down-conversion further boosts flux [132, 133]. A complementary route is dispersion engineering. Selecting or fabricating $\chi^{(2)}$ media whose zero-group-velocity-mismatch point lies near 1560 nm would relax the walk-off constraint, allow centimeter-scale interaction lengths, and thus raise the gain without resorting to tight focusing. Finally, seeded SPDC offers a controllable brightness knob. Injecting a weak, spectrally matched signal into one of the daughter modes stimulates the conjugate idler while preserving the desired photon-number correlations and time-energy entanglement; recent experiments have shown brightness increases of an order of magnitude with no measurable loss in quantum-state quality [32, 134].

Combining these strategies: waveguides for mode confinement, Sagnac or cavity recursion for path length, dispersion tailoring for longer crystals, and gentle seeding, should lift the present source well past the 10^6 pairs/s/mW benchmark and open the door to noise-limited quantum-metrology experiments.

CHAPTER 6 CONCLUSION

6.1 Summary of Works

This thesis addresses time-domain quantum optics on three fronts. First, Chapter 3 develops the chronocyclic Wigner-function formalism and, through a singular-value decomposition of the discretized distribution, defines the chronocyclic Schmidt number K_{C} as a rigorous, mode-independent gauge of joint time–frequency purity. Numerical tests on dispersion and SPM shaped frequency combs, together with full reconstructions obtained using an in-house SHG-FROG platform, verify that the SVD faithfully reproduces field statistics and links K_{C} to the conventional Schmidt number that quantifies spectral entanglement in biphoton SPDC states.

Chapter 4 translates these concepts into hardware by engineering a turn-key femtosecond pump. A custom mode-locked Er-fiber laser delivers 228 mW, 1560 nm pulses at 121.6 MHz; free-space compression shortens them to 110 fs, and an MgO:PPLN SHG converts them to 780 nm with 45% efficiency, yielding 91 mW average power. Applying the chronocyclic-Wigner analysis shows that both the fundamental ($K_{\mathrm{C}} = 1.64$) and frequency-doubled ($K_{\mathrm{C}} = 1.18$) pulses approach the single-mode limit, providing a spectrally and temporally clean pump for nonlinear interactions.

Chapter 5 demonstrates femtosecond type-II SPDC in a periodically poled lithium niobate bulk crystal. Classical backward-SHG mapping identified optimal phase-matching at a 10 µm grating and 135 °C, predicting low-gain pair production of 5×10^5 photons per second. Under the engineered 780 nm pump these conditions yield collinear, cross-polarized signal and idler beams with a measured brightness of $\sim 6.9 \times 10^6$ paired photons per second. These preliminary results validate the phase-matching model and establish a platform for high-signal-to-noise coincidence and heralded-photon experiments.

6.2 Limitations

The chronocyclic Schmidt number K_{C} introduced in Chapter 3, while valuable as a compact, mode-agnostic indicator of joint time–frequency purity, nonetheless has inherent constraints. Because it condenses the entire chronocyclic Wigner distribution into a single scalar, it cannot reveal the specific regions in time–frequency space where multimode contamination or low-level noise reside, nor can it discriminate isolated impurities from broad-band distortions. Its numerical value depends sensitively on the sampling grid and apodization used during Wigner

reconstruction, so changes in reconstruction settings or measurement bandwidth can shift K_C by tens of percent, complicating comparisons across platforms. Moreover, any ambiguities or artefacts in the SHG-FROG phase-retrieval step, such as temporal sign indeterminacy or carrier-envelope-offset errors, propagate directly into the SVD and may inflate apparent purity. Finally, as a second-order metric, K_C gives little insight into higher-order, non-Gaussian structure that can lurk beneath ostensibly low values of K_C.

Chapter4's pump source inherits limitations from each stage of its construction. Residual second- and third-order dispersion in the mode-locked Er-fiber oscillator restricts the useful spectral width to roughly 40 nm (FWHM), which in turn caps the transform-limited pulse duration near 90 fs and imposes a temporal pedestal that lowers contrast. Efforts to amplify and spectrally broaden the pulses are hampered by strong self-phase modulation in the Er-doped fiber amplifier: the nonlinear phase jumps embedded in the broadened spectrum resist conventional de-chirping and prevent compression below ∼100 fs. These phase discontinuities also complicate any attempt to extend the bandwidth into the ∼10 fs few-optical-cycle regime needed for genuine time-domain quantum-optic experiments. At the frequency-doubling stage, group-velocity mismatch of PPLN photo refractive heating limit the ultimate SHG conversion efficiency curbing the achievable pump fluence that can be delivered to the SPDC crystal and ultimately bounding the attainable pair-production rate.

The first SPDC experiments described in Chapter5 expose the intrinsic weakness of type-II interactions and the material constraints of lithium niobate at telecom wavelengths. The effective nonlinear coefficient accessed in type-II quasi-phase-matched $LiNbO_3$ is only about one-third of the type-0 value, so even under optimum poling and temperature the pair-production rate remains orders of magnitude lower than competing geometries and must be driven by higher pump powers or longer guides. Material and waveguide dispersion near 1560 nm introduce group-velocity mismatch between the ordinary and extraordinary photons on the order of 0.5 ps/mm, stretching the joint temporal envelope and narrowing the phase-matching bandwidth. Finally, Fresnel reflections at the chip facets, imperfect collection, and the falling quantum efficiency of InGaAs detectors toward longer wavelengths attenuate the detected flux and obscure spectral fine structure. Collectively, these factors cap the present brightness at roughly 7×10^6 pairs per second and limit the generation of highly pure, indistinguishable photon pairs required for advanced quantum-metrology protocols.

6.3 Future Research

Looking beyond the present results, three complementary research avenues emerge. First, the chronocyclic-Wigner analysis developed in Chapter 3 would benefit from metrics that preserve

spatial information rather than collapsing it into a scalar. Extending the framework to mode-resolved entropic measures, or applying tensor-network decompositions that capture higher-order correlations, could map where in the chronocyclic plane residual impurity originates and provide a richer basis for tailoring pulse-shaping strategies.

In Chapters 4 and 5, the most accessible performance gains come from (i) re-balancing dispersion and nonlinear phase within the pump chain, (ii) lengthening the nonlinear interaction in both the SHG and SPDC stages, and (iii) adopting self-seeding geometries such as Sagnac or double-pass loops to recycle undepleted pump light and enhance pair production. Looking farther ahead, moving the master-oscillator to a stretched-pulse regime, coupled with a modest pre-chirp before the EDFA, should tame the SPM-induced phase jumps and allow compression to the few-cycle regime directly from the fiber laser. This, in turn, paves the way for a fully fiber-integrated source in which the oscillator, amplifier and PPLN waveguides are fusion-spliced inside a single enclosure, eliminating free-space alignment drift and enabling true turnkey operation.

Within such a fiber platform, SHG efficiency can be raised by replacing bulk PPLN with periodically poled thin-film lithium-niobate-on-insulator waveguides, while the SPDC stage can migrate to monolithic, fiber-pigtailed chips that deliver brighter, spectrally factorable type-II photon pairs. Finally, exploring periodically poled $KTiOPO_4$, whose ordinary and extraordinary group velocities cross much closer to 1560 nm than in $LiNbO_3$, or custom-poled stoichiometric crystals with a zero-dispersion wavelength near 1560 nm offers a path to group-velocity-matched SPDC. Such dispersion-engineered platforms promise higher brightness, intrinsically indistinguishable photon pairs, and seamless compatibility with telecom-band quantum networks.

REFERENCES

[1] K. C. Tan and H. Jeong, "Nonclassical light and metrological power: An introductory review," *AVS Quantum Science*, vol. 1, no. 1, Nov. 2019. [Online]. Available: http://dx.doi.org/10.1116/1.5126696

[2] P.-A. Moreau, E. Toninelli, T. Gregory, and M. J. Padgett, "Imaging with quantum states of light," *Nature Reviews Physics*, vol. 1, no. 6, p. 367–380, May 2019. [Online]. Available: http://dx.doi.org/10.1038/s42254-019-0056-0

[3] J. Aasi *et al.*, "Enhanced sensitivity of the ligo gravitational wave detector by using squeezed states of light," *Nature Photonics*, vol. 7, no. 8, pp. 613–619, Aug 2013. [Online]. Available: https://doi.org/10.1038/nphoton.2013.177

[4] K. Hashimoto, D. B. Horoshko, M. I. Kolobov, Y. Michael, Z. Gefen, and M. V. Chekhova, "Fourier-transform infrared spectroscopy with undetected photons from high-gain spontaneous parametric down-conversion," *Communications Physics*, vol. 7, no. 1SN - 2399-3650, p. 217, Jul 2024. [Online]. Available: https://doi.org/10.1038/s42005-024-01717-3

[5] A. I. Lvovsky and M. G. Raymer, "Continuous-variable optical quantum-state tomography," *Reviews of Modern Physics*, vol. 81, no. 1, p. 299–332, Mar. 2009. [Online]. Available: http://dx.doi.org/10.1103/RevModPhys.81.299

[6] S. M. Kolenderska, F. Vanholsbeeck, and P. Kolenderski, "Fourier domain quantum optical coherence tomography," *Opt. Express*, vol. 28, no. 20, pp. 29 576–29 589, Sep 2020. [Online]. Available: https://opg.optica.org/oe/abstract.cfm?URI=oe-28-20-29576

[7] A. F. Abouraddy, M. B. Nasr, B. E. A. Saleh, A. V. Sergienko, and M. C. Teich, "Quantum-optical coherence tomography with dispersion cancellation," *Phys. Rev. A*, vol. 65, p. 053817, May 2002. [Online]. Available: https://link.aps.org/doi/10.1103/PhysRevA.65.053817

[8] Z. Ibarra-Borja, C. Sevilla-Gutiérrez, R. Ramírez-Alarcón, H. Cruz-Ramírez, and A. B. U'Ren, "Experimental demonstration of full-field quantum optical coherence tomography," *Photon. Res.*, vol. 8, no. 1, pp. 51–56, Jan 2020. [Online]. Available: https://opg.optica.org/prj/abstract.cfm?URI=prj-8-1-51

[9] S.-Y. Baek and Y.-H. Kim, "Spectral properties of entangled photons generated via type-i frequency-nondegenerate spontaneous parametric down-conversion," *Phys. Rev. A*, vol. 80, p. 033814, Sep 2009. [Online]. Available: https://link.aps.org/doi/10.1103/PhysRevA.80.033814

[10] B. Li, Z. Yuan, J. Williams, W. Jin, A. Beckert, T. Xie, J. Guo, A. Feshali, M. Paniccia, A. Faraon, J. Bowers, A. Marandi, and K. Vahala, "Down-converted photon pairs in a high-q silicon nitride microresonator," *Nature*, vol. 639, pp. 922–927, 03 2025.

[11] M. Bock, A. Lenhard, C. Chunnilall, and C. Becher, "Highly efficient heralded single-photon source for telecom wavelengths based on a ppln waveguide," *Opt. Express*, vol. 24, no. 21, pp. 23 992–24 001, Oct 2016. [Online]. Available: https://opg.optica.org/oe/abstract.cfm?URI=oe-24-21-23992

[12] M. V. Jabir and G. K. Samanta, "Robust, high brightness, degenerate entangled photon source at room temperature," *Scientific Reports*, vol. 7, no. 1, p. 12613, Oct 2017. [Online]. Available: https://doi.org/10.1038/s41598-017-12709-5

[13] F. Hou, X. Xiang, R. Quan, M. Wang, Y. Zhai, S. Wang, T. Liu, S. Zhang, and R. Dong, "An efficient source of frequency anti-correlated entanglement at telecom wavelength," *Applied Physics B*, vol. 122, no. 5, Apr. 2016. [Online]. Available: http://dx.doi.org/10.1007/s00340-016-6402-3

[14] C. Riek, P. Sulzer, M. Seeger, A. S. Moskalenko, G. Burkard, D. V. Seletskiy, and A. Leitenstorfer, "Subcycle quantum electrodynamics," *Nature*, vol. 541, no. 7637, p. 376–379, Jan. 2017. [Online]. Available: http://dx.doi.org/10.1038/nature21024

[15] P. Yan, W. Xu, H. Hu, Z. Zhang, Z. Li, and R. Shu, "Recent advances, applications, and perspectives in erbium-doped fiber combs," *Photonics*, vol. 11, no. 3, 2024. [Online]. Available: https://www.mdpi.com/2304-6732/11/3/192

[16] E. Desurvire and M. N. Zervas, "Erbium-doped fiber amplifiers: Principles and applications," *Physics Today*, vol. 48, no. 2, pp. 56–58, 02 1995. [Online]. Available: https://doi.org/10.1063/1.2807915

[17] R. Paschotta, "Periodic poling," RP Photonics Encyclopedia, 2005. [Online]. Available: https://www.rp-photonics.com/periodic_poling.html

[18] E. J. Stanton, J. Chiles, N. Nader, G. Moody, N. Volet, L. Chang, J. E. Bowers, S. W. Nam, and R. P. Mirin, "Efficient second harmonic generation in nanophotonic

gaas-on-insulator waveguides," *Opt. Express*, vol. 28, no. 7, pp. 9521–9532, Mar 2020. [Online]. Available: https://opg.optica.org/oe/abstract.cfm?URI=oe-28-7-9521

[19] T. S. Iskhakov, A. Perez, K. Y. Spasibko, M. V. Chekhova, and G. Leuchs, "Super-bunched bright squeezed vacuum state," 2012. [Online]. Available: https://arxiv.org/abs/1202.1682

[20] S. Virally, P. Cusson, and D. Seletskiy, "Enhanced electro-optic sampling with quantum probes," *Physical Review Letters*, vol. 127, 12 2021.

[21] J.-L. Smirr, R. Frey, E. Diamanti, R. Alléaume, and I. Zaquine, "Intrinsic limitations to the quality of pulsed spontaneous parametric downconversion sources for quantum information applications," *J. Opt. Soc. Am. B*, vol. 28, no. 4, pp. 832–841, Apr 2011. [Online]. Available: https://opg.optica.org/josab/abstract.cfm?URI=josab-28-4-832

[22] L. Coccia, A. Santamato, G. Vallone, and P. Villoresi, "Optimal focusing conditions for bright spontaneous parametric down-conversion sources," *Physical Review A*, vol. 107, no. 6, Jun. 2023. [Online]. Available: http://dx.doi.org/10.1103/PhysRevA.107.063712

[23] T. E. Keller and M. H. Rubin, "Theory of two-photon entanglement for spontaneous parametric down-conversion driven by a narrow pump pulse," *Phys. Rev. A*, vol. 56, pp. 1534–1541, Aug 1997. [Online]. Available: https://link.aps.org/doi/10.1103/PhysRevA.56.1534

[24] P.-A. Moreau, J. Sabines-Chesterking, R. Whittaker, S. K. Joshi, P. M. Birchall, A. McMillan, J. G. Rarity, and J. C. F. Matthews, "Demonstrating an absolute quantum advantage in direct absorption measurement," *Scientific Reports*, vol. 7, no. 1, p. 6256, Jul 2017. [Online]. Available: https://doi.org/10.1038/s41598-017-06545-w

[25] T. Jennewein, C. Simon, G. Weihs, H. Weinfurter, and A. Zeilinger, "Quantum cryptography with entangled photons," *Phys. Rev. Lett.*, vol. 84, pp. 4729–4732, May 2000. [Online]. Available: https://link.aps.org/doi/10.1103/PhysRevLett.84.4729

[26] S.-R. Zhao, Y.-Z. Zhang, W.-Z. Liu, J.-Y. Guan, W. Zhang, C.-L. Li, B. Bai, M.-H. Li, Y. Liu, L. You, J. Zhang, J. Fan, F. Xu, Q. Zhang, and J.-W. Pan, "Field demonstration of distributed quantum sensing without post-selection," *Phys. Rev. X*, vol. 11, p. 031009, Jul 2021. [Online]. Available: https://link.aps.org/doi/10.1103/PhysRevX.11.031009

[27] P. G. Kwiat, E. Waks, A. G. White, I. Appelbaum, and P. H. Eberhard, "Ultrabright source of polarization-entangled photons," *Physical Review A*, vol. 60, no. 2, p.

R773–R776, Aug. 1999. [Online]. Available: http://dx.doi.org/10.1103/PhysRevA.60.R773

[28] Y.-H. Kim, S. P. Kulik, and Y. Shih, "Bell-state preparation using pulsed nondegenerate two-photon entanglement," *Physical Review A*, vol. 63, no. 6, May 2001. [Online]. Available: http://dx.doi.org/10.1103/PhysRevA.63.060301

[29] K. Park, J. Lee, D.-G. Im, D. Kim, and Y. S. Ihn, "Ultrabright fiber-coupled ploarization-entangled photon source with spectral brightness surpassing 2.0 mhz/mw/nm," 2024. [Online]. Available: https://arxiv.org/abs/2409.15620

[30] J. Schneeloch, S. H. Knarr, D. F. Bogorin, M. L. Levangie, C. C. Tison, R. Frank, G. A. Howland, M. L. Fanto, and P. M. Alsing, "Introduction to the absolute brightness and number statistics in spontaneous parametric down-conversion," *Journal of Optics*, vol. 21, no. 4, p. 043501, feb 2019. [Online]. Available: https://dx.doi.org/10.1088/2040-8986/ab05a8

[31] O. Kuzucu and F. N. C. Wong, "Pulsed sagnac source of narrow-band polarization-entangled photons," *Phys. Rev. A*, vol. 77, p. 032314, Mar 2008. [Online]. Available: https://link.aps.org/doi/10.1103/PhysRevA.77.032314

[32] D. Adamou, L. Hirsch, T. Shields, S. Yoon, A. C. Dada, J. M. R. Weaver, D. Faccio, M. Peccianti, L. Caspani, and M. Clerici, "Quantum-enhanced time-domain spectroscopy," *Science Advances*, vol. 11, no. 4, p. eadt2187, 2025. [Online]. Available: https://www.science.org/doi/abs/10.1126/sciadv.adt2187

[33] J. F. Haase, Z.-Y. Wang, J. Casanova, and M. B. Plenio, "Pulse-phase control for spectral disambiguation in quantum sensing protocols," *Phys. Rev. A*, vol. 94, p. 032322, Sep 2016. [Online]. Available: https://link.aps.org/doi/10.1103/PhysRevA.94.032322

[34] T. Ono, Y. Tsujimoto, K. Wakui, and M. Fujiwara, "Quantum interference of pulsed time-bin entanglement generated from silicon ring resonator," *Scientific Reports*, vol. 14, 01 2024.

[35] P. J. Mosley, J. S. Lundeen, B. J. Smith, P. Wasylczyk, A. B. U'Ren, C. Silberhorn, and I. A. Walmsley, "Heralded generation of ultrafast single photons in pure quantum states," *Phys. Rev. Lett.*, vol. 100, p. 133601, Apr 2008. [Online]. Available: https://link.aps.org/doi/10.1103/PhysRevLett.100.133601

[36] P. G. Kwiat, K. Mattle, H. Weinfurter, A. Zeilinger, A. V. Sergienko, and Y. Shih, "New high-intensity source of polarization-entangled photon pairs,"

Phys. Rev. Lett., vol. 75, pp. 4337–4341, Dec 1995. [Online]. Available: https://link.aps.org/doi/10.1103/PhysRevLett.75.4337

[37] Y.-C. Jeong, K.-H. Hong, and Y.-H. Kim, "Bright source of polarization-entangled photons using a ppktp pumped by a broadband multi-mode diode laser," *Opt. Express*, vol. 24, no. 2, pp. 1165–1174, Jan 2016. [Online]. Available: https://opg.optica.org/oe/abstract.cfm?URI=oe-24-2-1165

[38] C. Kim, H. Kim, M. Choi, J. Lee, Y. Park, S. Moon, J. Lee, H. Hwang, M.-K. Seo, Y.-H. Kim, Y.-S. Kim, H. Jung, and H. Kwon, "Integrated bright source of polarization-entangled photons using lithium niobate photonic chips," 2025. [Online]. Available: https://arxiv.org/abs/2506.23625

[39] J. Kellner, A. Sabatti, T. Kuttner, R. J. Chapman, and R. Grange, "Counter-propagating spontaneous parametric down-conversion source in lithium niobate on insulator," 2025. [Online]. Available: https://arxiv.org/abs/2506.21396

[40] L. Cruz-Rodriguez, D. Dey, A. Freibert, and P. Stammer, "Quantum phenomena in attosecond science," *Nature Reviews Physics*, vol. 6, no. 11, p. 691–704, Oct. 2024. [Online]. Available: http://dx.doi.org/10.1038/s42254-024-00769-2

[41] K.-C. Chang, X. Cheng, M. C. Sarihan, and C. W. Wong, "Recent advances in high-dimensional quantum frequency combs," *Newton*, vol. 1, no. 1, p. 100024, 2025. [Online]. Available: https://www.sciencedirect.com/science/article/pii/S2950636025000167

[42] C. A. Casacio, L. S. Madsen, A. Terrasson, M. Waleed, K. Barnscheidt, B. Hage, M. A. Taylor, and W. P. Bowen, "Quantum-enhanced nonlinear microscopy," *Nature*, vol. 594, no. 7862, pp. 201–206, Jun 2021. [Online]. Available: https://doi.org/10.1038/s41586-021-03528-w

[43] R. Erdmann, D. Branning, W. Grice, and I. A. Walmsley, "Restoring dispersion cancellation for entangled photons produced by ultrashort pulses," *Phys. Rev. A*, vol. 62, p. 053810, Oct 2000. [Online]. Available: https://link.aps.org/doi/10.1103/PhysRevA.62.053810

[44] G. Triginer, M. D. Vidrighin, N. Quesada, A. Eckstein, M. Moore, W. S. Kolthammer, J. E. Sipe, and I. A. Walmsley, "Understanding high-gain twin-beam sources using cascaded stimulated emission," *Phys. Rev. X*, vol. 10, p. 031063, Sep 2020. [Online]. Available: https://link.aps.org/doi/10.1103/PhysRevX.10.031063

[45] J. Williams, R. Nehra, E. Sendonaris, L. Ledezma, R. M. Gray, R. Sekine, and A. Marandi, "Ultra-short pulse biphoton source in lithium niobate nanophotonics at 2um," 2024. [Online]. Available: https://arxiv.org/abs/2402.05163

[46] A. M. Pérez, T. S. Iskhakov, P. Sharapova, S. Lemieux, O. V. Tikhonova, M. V. Chekhova, and G. Leuchs, "Bright squeezed-vacuum source with 1.1 spatial mode," *Opt. Lett.*, vol. 39, no. 8, pp. 2403–2406, Apr 2014. [Online]. Available: https://opg.optica.org/ol/abstract.cfm?URI=ol-39-8-2403

[47] D. Seletskiy, P. Cusson, A. Rasputnyi, S. Virally, F. Tani, and M. Chekhova, "Bright few-cycle quantum light," in *Ultrafast Phenomena and Nanophotonics XXIX*, M. Betz and A. Y. Elezzabi, Eds., vol. PC13364, International Society for Optics and Photonics. SPIE, 2025, p. PC133640O. [Online]. Available: https://doi.org/10.1117/12.3043124

[48] A. Rasputnyi, Z. Chen, M. Birk, O. Cohen, I. Kaminer, M. Krüger, D. Seletskiy, M. Chekhova, and F. Tani, "High-harmonic generation by a bright squeezed vacuum," *Nature Physics*, vol. 20, no. 12, p. 1960–1965, Oct. 2024. [Online]. Available: http://dx.doi.org/10.1038/s41567-024-02659-x

[49] Y.-H. Kim, M. V. Chekhova, S. P. Kulik, M. H. Rubin, and Y. Shih, "Interferometric bell-state preparation using femtosecond-pulse-pumped spontaneous parametric down-conversion," *Phys. Rev. A*, vol. 63, p. 062301, May 2001. [Online]. Available: https://link.aps.org/doi/10.1103/PhysRevA.63.062301

[50] A. Eckstein, A. Christ, P. J. Mosley, and C. Silberhorn, "Highly efficient single-pass source of pulsed single-mode twin beams of light," *Phys. Rev. Lett.*, vol. 106, p. 013603, Jan 2011. [Online]. Available: https://link.aps.org/doi/10.1103/PhysRevLett.106.013603

[51] F. Laudenbach, R.-B. Jin, C. Greganti, M. Hentschel, P. Walther, and H. Hübel, "Numerical investigation of photon-pair generation in periodically poled $m\mathrm{TiO}x\mathrm{o}_4$ ($m =$ K, rb, cs; $x = p$, as)," *Phys. Rev. Appl.*, vol. 8, p. 024035, Aug 2017. [Online]. Available: https://link.aps.org/doi/10.1103/PhysRevApplied.8.024035

[52] Wang, Jinbao and Lin, Haibo, "The single-cycle biphotons generated by noncollinear spdc in the chirped qpm crystals," *J. Eur. Opt. Society-Rapid Publ.*, vol. 20, no. 1, p. 6, 2024. [Online]. Available: https://doi.org/10.1051/jeos/2024004

[53] M. M. Weston, H. M. Chrzanowski, S. Wollmann, A. Boston, J. Ho, L. K. Shalm, V. B. Verma, M. S. Allman, S. W. Nam, R. B. Patel, S. Slussarenko, and G. J.

Pryde, "Efficient and pure femtosecond-pulse-length source of polarization-entangled photons," *Opt. Express*, vol. 24, no. 10, pp. 10 869–10 879, May 2016. [Online]. Available: https://opg.optica.org/oe/abstract.cfm?URI=oe-24-10-10869

[54] R.-B. Jin, R. Shimizu, K. Wakui, H. Benichi, and M. Sasaki, "Widely tunable single photon source with high purity at telecom wavelength," *Opt. Express*, vol. 21, no. 9, pp. 10 659–10 666, May 2013. [Online]. Available: https://opg.optica.org/oe/abstract.cfm?URI=oe-21-9-10659

[55] R.-B. Jin, R. Shimizu, K. Wakui, M. Fujiwara, T. Yamashita, S. Miki, H. Terai, Z. Wang, and M. Sasaki, "Pulsed sagnac polarization-entangled photon source with a ppktp crystal at telecom wavelength," *Opt. Express*, vol. 22, no. 10, pp. 11 498–11 507, May 2014. [Online]. Available: https://opg.optica.org/oe/abstract.cfm?URI=oe-22-10-11498

[56] J. Paye, "The chronocyclic representation of ultrashort light pulses," *IEEE Journal of Quantum Electronics*, vol. 28, no. 10, pp. 2262–2273, 1992.

[57] D. Kane and R. Trebino, "Characterization of arbitrary femtosecond pulses using frequency-resolved optical gating," *IEEE Journal of Quantum Electronics*, vol. 29, no. 2, pp. 571–579, 1993.

[58] J. Riedel. (2014) Wigner function = fourier transform + coordinate rotation. [Online]. Available: https://blog.jessriedel.com/2014/04/01/wigner-function-fourier-transform-coordinate-rotation/

[59] W. K. Wootters, "A wigner-function formulation of finite-state quantum mechanics," *Annals of Physics*, vol. 176, no. 1, pp. 1–21, 1987. [Online]. Available: https://www.sciencedirect.com/science/article/pii/000349168790176X

[60] M. Beck, M. G. Raymer, I. A. Walmsley, and V. Wong, "Chronocyclic tomography for measuring the amplitude and phase structure of optical pulses," *Opt. Lett.*, vol. 18, no. 23, pp. 2041–2043, Dec 1993. [Online]. Available: https://opg.optica.org/ol/abstract.cfm?URI=ol-18-23-2041

[61] R. Paschotta, "Frequency combs," RP Photonics Encyclopedia, 2007. [Online]. Available: https://www.rp-photonics.com/frequency_combs.html

[62] T. Fortier and E. Baumann, "20 years of developments in optical frequency comb technology and applications," *Communications Physics*, vol. 2, no. 1, p. 153, Dec 2019. [Online]. Available: https://doi.org/10.1038/s42005-019-0249-y

[63] A. S. Wyatt and I. A. Walmsley, *Measuring Ultrashort Optical Pulses*. Heidelberg: Springer International Publishing, 2013, pp. 1–21. [Online]. Available: https://doi.org/10.1007/978-3-319-00017-6_1

[64] R. H. Stolen and C. Lin, "Self-phase-modulation in silica optical fibers," *Phys. Rev. A*, vol. 17, pp. 1448–1453, Apr 1978. [Online]. Available: https://link.aps.org/doi/10.1103/PhysRevA.17.1448

[65] F. X. Kärtner and U. Keller, "Stabilization of solitonlike pulses with a slow saturable absorber," *Opt. Lett.*, vol. 20, no. 1, pp. 16–18, Jan 1995. [Online]. Available: https://opg.optica.org/ol/abstract.cfm?URI=ol-20-1-16

[66] S. A. Diddams, "Bigger and better: The critical role of self-phase modulation in ultra-precise optical frequency combs," in *Conference on Lasers and Electro-Optics/Quantum Electronics and Laser Science Conference and Photonic Applications Systems Technologies*. Optica Publishing Group, 2007, p. JTuC5.

[67] D. R. Austin, T. Witting, A. S. Wyatt, and I. A. Walmsley, "Measuring sub-planck structural analogues in chronocyclic phase space," *Optics Communications*, vol. 283, no. 5, pp. 855–859, 2010, quo vadis Quantum Optics? [Online]. Available: https://www.sciencedirect.com/science/article/pii/S0030401809010529

[68] D. J. Jones, S. A. Diddams, J. K. Ranka, A. Stentz, R. S. Windeler, J. L. Hall, and S. T. Cundiff, "Carrier-envelope phase control of femtosecond mode-locked lasers and direct optical frequency synthesis," *Science*, vol. 288, no. 5466, pp. 635–639, 2000. [Online]. Available: https://www.science.org/doi/abs/10.1126/science.288.5466.635

[69] R. Holzwarth, T. Udem, T. W. Hänsch, J. C. Knight, W. J. Wadsworth, and P. S. J. Russell, "Optical frequency synthesizer for precision spectroscopy," *Phys. Rev. Lett.*, vol. 85, pp. 2264–2267, Sep 2000. [Online]. Available: https://link.aps.org/doi/10.1103/PhysRevLett.85.2264

[70] N. C. Geib, M. Zilk, T. Pertsch, and F. Eilenberger, "Common pulse retrieval algorithm: a fast and universal method to retrieve ultrashort pulses," *Optica*, vol. 6, no. 4, pp. 495–505, Apr 2019. [Online]. Available: https://opg.optica.org/optica/abstract.cfm?URI=optica-6-4-495

[71] W. P. Grice and I. A. Walmsley, "Spectral information and distinguishability in type-ii down-conversion with a broadband pump," *Phys. Rev. A*, vol. 56, pp. 1627–1634, Aug 1997. [Online]. Available: https://link.aps.org/doi/10.1103/PhysRevA.56.1627

[72] F. Graffitti, J. Kelly-Massicotte, A. Fedrizzi, and A. M. Brańczyk, "Design considerations for high-purity heralded single-photon sources," *Phys. Rev. A*, vol. 98, p. 053811, Nov 2018. [Online]. Available: https://link.aps.org/doi/10.1103/PhysRevA.98.053811

[73] C. K. Law, I. A. Walmsley, and J. H. Eberly, "Continuous frequency entanglement: Effective finite hilbert space and entropy control," *Phys. Rev. Lett.*, vol. 84, pp. 5304–5307, Jun 2000. [Online]. Available: https://link.aps.org/doi/10.1103/PhysRevLett.84.5304

[74] J. H. Eberly, "Schmidt analysis of pure-state entanglement," *Laser Physics*, vol. 16, no. 6, p. 921–926, Jun. 2006. [Online]. Available: http://dx.doi.org/10.1134/S1054660X06060041

[75] Q. Guo, B. K. Gutierrez, R. Sekine, R. M. Gray, J. A. Williams, L. Ledezma, L. Costa, A. Roy, S. Zhou, M. Liu, and A. Marandi, "Ultrafast mode-locked laser in nanophotonic lithium niobate," *Science*, vol. 382, no. 6671, pp. 708–713, 2023. [Online]. Available: https://www.science.org/doi/abs/10.1126/science.adj5438

[76] E. Innerhofer, T. Südmeyer, F. Brunner, R. Paschotta, and U. Keller, "Mode-locked high-power lasers and nonlinear optics – a powerful combination," *Laser Physics Letters*, vol. 1, no. 2, p. 82, jan 2004. [Online]. Available: https://dx.doi.org/10.1002/lapl.200310025

[77] L. Huang, A. K. Mills, Y. Zhao, D. J. Jones, and S. Tang, "Miniature fiber-optic multiphoton microscopy system using frequency-doubled femtosecond er-doped fiber laser," *Biomed. Opt. Express*, vol. 7, no. 5, pp. 1948–1956, May 2016. [Online]. Available: https://opg.optica.org/boe/abstract.cfm?URI=boe-7-5-1948

[78] O. Haderka, R. Machulka, J. Peřina, A. Allevi, and M. Bondani, "Spatial and spectral coherence in propagating high-intensity twin beams," *Scientific Reports*, vol. 5, no. 1, p. 14365, Sep 2015. [Online]. Available: https://doi.org/10.1038/srep14365

[79] C.-Y. Cho, J.-Y. Lai, C.-S. Hsu, Y.-T. Huang, J.-H. Jang, and M.-H. Chou, "Power scaling of continuous-wave second harmonic generation in a mgo:ppln ridge waveguide and the application to a compact wavelength conversion module," *Opt. Lett.*, vol. 46, no. 12, pp. 2852–2855, Jun 2021. [Online]. Available: https://opg.optica.org/ol/abstract.cfm?URI=ol-46-12-2852

[80] B. Ainslie, "A review of the fabrication and properties of erbium-doped fibers for optical amplifiers," *Journal of Lightwave Technology*, vol. 9, no. 2, pp. 220–227, 1991.

[81] N. Namekata, S. Sasamori, and S. Inoue, "800 mhz single-photon detection at 1550-nm using an ingaas/inp avalanche photodiode operated with a sine wave gating," *Opt. Express*, vol. 14, no. 21, pp. 10 043–10 049, Oct 2006. [Online]. Available: https://opg.optica.org/oe/abstract.cfm?URI=oe-14-21-10043

[82] D. Reddy, R. Nerem, S. W. Nam, R. Mirin, and V. Verma, "Superconducting nanowire single-photon detectors with 98% system detection efficiency at 1550 nm," no. 7, 2020-11-23 05:11:00 2020.

[83] L. Rivard, "Development of a versatile 76 mhz fiber based source of 9-fs pulses in the near-infrared and phase-stable ps pulses in the mid-infrared," Master's thesis, Polytechnique Montréal, June 2023. [Online]. Available: https://publications.polymtl.ca/54125/

[84] A. Labranche, "Conception of a low-noise ultrafast fiber laser system toward nj phase stable pulses in the mid-infrared," Master's thesis, Polytechnique Montréal, December 2020. [Online]. Available: https://publications.polymtl.ca/5561/

[85] C. DIETRICH, "Development of a low-noise ultrafast fiber laser and optimization of nonlinear crystals for bright, high-purity entangled photon sources," Ph.D. dissertation, POLYTECHNIQUE MONTRÉAL, 2024.

[86] G. Divyangna, "Evaluation of gain and noise figure spectrum of edfa by optimizing its parameters with different pumping schemes in the scenario of wdm system," in *Emerging Technology Trends in Electronics, Communication and Networking*, S. Gupta and J. N. Sarvaiya, Eds. Singapore: Springer Singapore, 2020, pp. 136–146.

[87] C. Kim, S. Bae, K. Kieu, and J. Kim, "Sub-femtosecond timing jitter, all-fiber, cnt-mode-locked er-laser at telecom wavelength," *Opt. Express*, vol. 21, no. 22, pp. 26 533–26 541, Nov 2013. [Online]. Available: https://opg.optica.org/oe/abstract.cfm?URI=oe-21-22-26533

[88] R. Paschotta, "Noise of mode-locked lasers (part ii): timing jitter and other fluctuations," *Applied Physics B*, vol. 79, no. 2, pp. 163–173, Jul 2004. [Online]. Available: https://doi.org/10.1007/s00340-004-1548-9

[89] J. Limpert, T. Clausnitzer, A. Liem, T. Schreiber, H.-J. Fuchs, H. Zellmer, E.-B. Kley, and A. Tnnermann, "High-average-power femtosecond fiber chirped-pulse

amplification system," *Opt. Lett.*, vol. 28, no. 20, pp. 1984–1986, Oct 2003. [Online]. Available: https://opg.optica.org/ol/abstract.cfm?URI=ol-28-20-1984

[90] S. L. Schieffer, J. A. Berger, B. L. Rickman, V. P. Nayyar, and W. A. Schroeder, "Thermal effects in semiconductor saturable-absorber mirrors," *J. Opt. Soc. Am. B*, vol. 29, no. 4, pp. 543–552, Apr 2012. [Online]. Available: https://opg.optica.org/josab/abstract.cfm?URI=josab-29-4-543

[91] D. Y. Tang, L. M. Zhao, B. Zhao, and A. Q. Liu, "Mechanism of multisoliton formation and soliton energy quantization in passively mode-locked fiber lasers," *Phys. Rev. A*, vol. 72, p. 043816, Oct 2005. [Online]. Available: https://link.aps.org/doi/10.1103/PhysRevA.72.043816

[92] J. M. Soto-Crespo, N. Akhmediev, P. Grelu, and F. Belhache, "Quantized separations of phase-locked soliton pairs in fiber lasers," *Opt. Lett.*, vol. 28, no. 19, pp. 1757–1759, Oct 2003. [Online]. Available: https://opg.optica.org/ol/abstract.cfm?URI=ol-28-19-1757

[93] G. Agrawal, "Chapter 4 - self-phase modulation," in *Nonlinear Fiber Optics (Fifth Edition)*, fifth edition ed., ser. Optics and Photonics, G. Agrawal, Ed. Boston: Academic Press, 2013, pp. 87–128. [Online]. Available: https://www.sciencedirect.com/science/article/pii/B9780123970237000048

[94] J. P. Gordon, "Theory of the soliton self-frequency shift," *Opt. Lett.*, vol. 11, no. 10, pp. 662–664, Oct 1986. [Online]. Available: https://opg.optica.org/ol/abstract.cfm?URI=ol-11-10-662

[95] A. Rantamäki, J. Lyytikäinen, J. Nikkinen, and O. G. Okhotnikov, "Effect of thermal management on the propertiesof saturable absorber mirrors in high-power mode-locked semiconductor disk lasers," *Quantum Electronics*, vol. 41, no. 9, p. 786, sep 2011. [Online]. Available: https://dx.doi.org/10.1070/QE2011v041n09ABEH014658

[96] R. Paschotta, "Kelly sidebands," RP Photonics Encyclopedia, 2005. [Online]. Available: https://www.rp-photonics.com/kelly_sidebands.html

[97] M. Dennis and I. Duling, "Experimental study of sideband generation in femtosecond fiber lasers," *IEEE Journal of Quantum Electronics*, vol. 30, no. 6, pp. 1469–1477, 1994.

[98] S. M. J. Kelly, "Characteristic sideband instability of the periodically amplified (average) soliton." in *XVIII International Quantum Electronics Conference*. Optica Publishing Group, 1992, p. TuH3. [Online]. Available: https://opg.optica.org/abstract.cfm?URI=IQEC-1992-TuH3

[99] F. Cattani, D. Anderson, A. Berntson, and M. Lisak, "Effect of self-phase modulation in chirped-pulse-amplification-like schemes," *J. Opt. Soc. Am. B*, vol. 16, no. 11, pp. 1874–1879, Nov 1999. [Online]. Available: https://opg.optica.org/josab/abstract.cfm?URI=josab-16-11-1874

[100] E. Rubiola, K. Volyanskiy, and L. Larger, "Measurement of the laser relative intensity noise," 04 2009, pp. 50–53.

[101] R. Paschotta, "Relative intensity noise," RP Photonics Encyclopedia, 2007. [Online]. Available: https://www.rp-photonics.com/relative_intensity_noise.html

[102] C. R. Smith, R. D. Engelsholm, and O. Bang, "Pulse-to-pulse relative intensity noise measurements for ultrafast lasers," *Opt. Express*, vol. 30, no. 5, pp. 8136–8150, Feb 2022. [Online]. Available: https://opg.optica.org/oe/abstract.cfm?URI=oe-30-5-8136

[103] G. Danion, F. Bondu, G. Loas, and M. Alouini, "Ghz bandwidth noise eater hybrid optical amplifier: design guidelines," *Opt. Lett.*, vol. 39, no. 14, pp. 4239–4242, Jul 2014. [Online]. Available: https://opg.optica.org/ol/abstract.cfm?URI=ol-39-14-4239

[104] K. Wu, P. Shum, S. Aditya, C. Ouyang, J. Wong, L. Quoc Huy, and K. Lee, "Noise conversion from pump to the passively mode-locked fiber lasers at 1.5 μm," *Optics Letters*, vol. 37, pp. 1901–1903, 05 2012.

[105] H. Byun, M. Sander, A. Motamedi, H. Shen, G. Petrich, L. Kolodziejski, E. Ippen, and F. Kärtner, "Compact, stable 1 ghz femtosecond er-doped fiber lasers," *Applied Optics*, vol. 49, pp. 5577–5582, 10 2010.

[106] X. Cheng, W. Pan, X. Zeng, J. Dong, S. Cui, and Y. Feng, "Relative intensity noise comparison of fiber laser and amplified spontaneous emission sources," *Optical Fiber Technology*, vol. 54, p. 102119, 2020. [Online]. Available: https://www.sciencedirect.com/science/article/pii/S1068520019306911

[107] G. D. Boyd and D. A. Kleinman, "Parametric interaction of focused gaussian light beams," *Journal of Applied Physics*, vol. 39, no. 8, pp. 3597–3639, 07 1968. [Online]. Available: https://doi.org/10.1063/1.1656831

[108] Y. Furukawa, K. Kitamura, A. Alexandrovski, R. K. Route, M. M. Fejer, and G. Foulon, "Green-induced infrared absorption in mgo doped linbo3," *Applied Physics Letters*, vol. 78, no. 14, pp. 1970–1972, 04 2001. [Online]. Available: https://doi.org/10.1063/1.1359137

[109] S. Akturk, X. Gu, M. Kimmel, and R. Trebino, "Extremely simple single-prism ultrashort-pulse compressor," *Opt. Express*, vol. 14, no. 21, pp. 10 101–10 108, Oct 2006. [Online]. Available: https://opg.optica.org/oe/abstract.cfm?URI=oe-14-21-10101

[110] T. Ehmke, A. Knebl, S. Reiss, I. R. Fischinger, T. G. Seiler, O. Stachs, and A. Heisterkamp, "Spectral behavior of second harmonic signals from organic and non-organic materials in multiphoton microscopy," *AIP Advances*, vol. 5, no. 8, p. 084903, 03 2015. [Online]. Available: https://doi.org/10.1063/1.4915134

[111] A. M. Schober, M. Charbonneau-Lefort, and M. M. Fejer, "Broadband quasi-phase-matched second-harmonic generation of ultrashort optical pulses with spectral angular dispersion," *J. Opt. Soc. Am. B*, vol. 22, no. 8, pp. 1699–1713, Aug 2005. [Online]. Available: https://opg.optica.org/josab/abstract.cfm?URI=josab-22-8-1699

[112] L. Huang, X. Zhou, and S. Tang, "Optimization of frequency-doubled Er-doped fiber laser for miniature multiphoton endoscopy," *Journal of Biomedical Optics*, vol. 23, no. 12, p. 126503, 2018. [Online]. Available: https://doi.org/10.1117/1.JBO.23.12.126503

[113] R. Paschotta, "Mode-locked fiber lasers," RP Photonics Encyclopedia, 2006, refer to the Stretched-pulse Fiber Lasers section. [Online]. Available: https://www.rp-photonics.com/mode_locked_fiber_lasers.html

[114] L. C. Sinclair, I. Coddington, W. S. Swann, and N. R. Newbury, "Stabilization of the offset frequency of an all polarization-maintaining fiber erbium frequency comb," in *CLEO: 2013*, 2013, pp. 1–2.

[115] X. Shan, Y. Zheng, and R. Zhu, "Self-phase modulation-induced instability of high-power narrow-linewidth fiber amplifiers," *Photonics*, vol. 10, no. 12, 2023. [Online]. Available: https://www.mdpi.com/2304-6732/10/12/1330

[116] D. Schimpf, E. Seise, J. Limpert, and A. Tünnermann, "Self-phase modulation compensated by positive dispersion in chirped-pulse systems," *Optics Express*, vol. 17, pp. 4997–5007, 03 2009.

[117] J. Sun, Y. Zhou, Y. Dai, J. Li, F. Yin, J. Dai, and K. Xu, "All-fiber polarization-maintaining erbium-doped dispersion-managed fiber laser based on a nonlinear amplifying loop mirror," *Appl. Opt.*, vol. 57, no. 6, pp. 1492–1496, Feb 2018. [Online]. Available: https://opg.optica.org/ao/abstract.cfm?URI=ao-57-6-1492

[118] F. Verluise, V. Laude, Z. Cheng, C. Spielmann, and P. Tournois, "Amplitude and phase control of ultrashort pulses by use of an acousto-optic programmable dispersive filter: Pulse compression and shaping," *Optics Letters*, vol. 25, pp. 575–577, 04 2000.

[119] R. Paschotta, "Parabolic pulses," 2006. [Online]. Available: https://www.rpphotonics.com/parabolic_pulses.html

[120] B. Nie, D. Pestov, F. Wise, and M. Dantus, "Generation of 42-fs and 10-nj pulses from a fiber laser with self-similar evolution in the gain segment," *Optics Express*, vol. 19, pp. 12 074–12 080, 06 2011.

[121] J.-F. Zhang, L. Wu, and L. Li, "Self-similar parabolic pulses in optical fiber amplifiers with gain dispersion and gain saturation," *Phys. Rev. A*, vol. 78, p. 055801, Nov 2008. [Online]. Available: https://link.aps.org/doi/10.1103/PhysRevA.78.055801

[122] Sep 2024. [Online]. Available: https://covesion.com/knowledge-hub/technical-guide-frequency-doubling-femtosecond-fibre-lasers/

[123] S. Suntsov, C. Rüter, D. Brüske, and D. Kip, "Watt-level 775 nm shg with 70

[124] C. Wang, C. Langrock, A. Marandi, M. Jankowski, M. Zhang, B. Desiatov, M. M. Fejer, and M. Lončar, "Ultrahigh-efficiency wavelength conversion in nanophotonic periodically poled lithium niobate waveguides," *Optica*, vol. 5, no. 11, p. 1438, Nov. 2018. [Online]. Available: http://dx.doi.org/10.1364/OPTICA.5.001438

[125] S. Hbeeb and A. S. Abdullah, "Thermo-optic coefficient of lithium niobate ln using optical interferometric technique," *Journal of Optics*, 12 2024.

[126] P. Kuo, T. Gerrits, V. Verma, S. Nam, O. Slattery, L. Ma, and X. Tang, "Characterization of type-ii spontaneous parametric down-conversion in domain-engineered ppln," vol. 9762, 03 2016, p. 976211.

[127] L. Hong, B. Chen, C. Hu, P. He, and Z.-Y. Li, "Rainbow cherenkov second-harmonic radiation," *Phys. Rev. Appl.*, vol. 18, p. 044063, Oct 2022. [Online]. Available: https://link.aps.org/doi/10.1103/PhysRevApplied.18.044063

[128] X. Deng, H. Ren, H. Lao, and X. Chen, "Research on cherenkov second-harmonic generation in periodically poled lithium niobate by femtosecond pulses," *J. Opt. Soc. Am. B*, vol. 27, no. 7, pp. 1475–1480, Jul 2010. [Online]. Available: https://opg.optica.org/josab/abstract.cfm?URI=josab-27-7-1475

[129] W. Risk, T. Gosnell, and A. Nurmikko, "Compact blue-green lasers," *Compact Blue-Green Lasers, by W. P. Risk and T. R. Gosnell and A. V. Nurmikko, pp. 552. ISBN 0521623189. Cambridge, UK: Cambridge University Press, January 2003.*, 01 2003.

[130] M. Hentschel, H. Huebel, A. Poppe, and A. Zeilinger, "Compact sagnac-type source for entangled photon pairs," in *CLEO/Europe and EQEC 2009 Conference Digest.* Optica Publishing Group, 2009, pp. ED1—2.

[131] P. J. Thomas, C. J. Chunnilall, D. J. M. Stothard, D. A. Walsh, and M. H. Dunn, "Production of degenerate polarization entangled photon pairs in the telecom-band from a pump enhanced parametric downconversion process," *Opt. Express*, vol. 18, no. 25, pp. 26 600–26 612, Dec 2010. [Online]. Available: https://opg.optica.org/oe/abstract.cfm?URI=oe-18-25-26600

[132] O. Slattery, L. Ma, K. Zong, and X. Tang, "Background and review of cavity-enhanced spontaneous parametric down-conversion," *Journal of Research of the National Institute of Standards and Technology*, vol. 124, 08 2019.

[133] J. A. Zielińska and M. W. Mitchell, "Theory of high gain cavity-enhanced spontaneous parametric down-conversion," *Phys. Rev. A*, vol. 90, p. 063833, Dec 2014. [Online]. Available: https://link.aps.org/doi/10.1103/PhysRevA.90.063833

[134] P. Wan, W.-Z. Zhu, Y.-C. Lou, Z.-M. Cheng, Z.-C. Ren, H. Zhang, X.-L. Wang, and H.-T. Wang, "Postselection-free cavity-enhanced narrow-band orbital angular momentum entangled photon source," *Phys. Rev. Lett.*, vol. 134, p. 053801, Feb 2025. [Online]. Available: https://link.aps.org/doi/10.1103/PhysRevLett.134.053801

APPENDIX A DERIVATION OF THE MOMENT IDENTITY

The rms pulse width is defined via the second temporal moment (see equation 4.3.2 in [93])

$$\langle t^2 \rangle = \frac{\int_{-\infty}^{\infty} t^2 |E(t)|^2 \, dt}{\int_{-\infty}^{\infty} |E(t)|^2 \, dt}. \tag{A.1}$$

We adopt the angular-frequency convention

$$\tilde{E}(\omega) = \int_{-\infty}^{\infty} E(t) \, e^{i\omega t} \, dt, \tag{A.2a}$$

$$E(t) = \frac{1}{2\pi} \int_{-\infty}^{\infty} \tilde{E}(\omega) \, e^{-i\omega t} \, d\omega. \tag{A.2b}$$

Parseval's theorem then reads

$$\int_{-\infty}^{\infty} |f(t)|^2 \, dt = \frac{1}{2\pi} \int_{-\infty}^{\infty} \left| \tilde{f}(\omega) \right|^2 d\omega. \tag{A.3}$$

A direct two-step integration by parts (omitted here for brevity) gives

$$\mathcal{F}\Big\{ \, t \, E(t) \Big\}(\omega) = i \, \partial_\omega \tilde{E}(\omega), \tag{A.4}$$

where $\mathcal{F}\{\cdot\}$ denotes the transform in (A.2).

Applying (A.3) to $f(t) = tE(t)$ and using (A.4) yields

$$\int_{-\infty}^{\infty} t^2 |E(t)|^2 \, dt = \frac{1}{2\pi} \int_{-\infty}^{\infty} \left| \partial_\omega \tilde{E}(\omega) \right|^2 d\omega. \tag{A.5}$$

Writing $\tilde{E}(\omega) = A(\omega) e^{i\phi(\omega)}$ inserting $|\partial_\omega \tilde{E}|^2 = |A'|^2 + A^2(\phi')^2$ in (A.5), and (A.5) in (A.1) gives the second moment-method result

$$\langle t^2 \rangle = \langle t^2 \rangle_0 + \frac{\int_{-\infty}^{\infty} A^2(\omega) \left[\phi'(\omega) \right]^2 d\omega}{\int_{-\infty}^{\infty} A^2(\omega) \, d\omega}, \tag{A.6}$$

where $\langle t^2 \rangle_0$ is the transform-limited width.

APPENDIX B DERIVATION OF THE FREQUENCY-DOMAIN OVERLAP INTEGRAL TO ITS EIGEN-EXPANSION

From equation 4.12, after dropping the overall constants

$$\mathcal{O} = \int_{-\infty}^{+\infty} \mathrm{d}\Omega\, \tilde{A}(\Omega)\tilde{A}(-\Omega)\, \Phi(\Omega), \tag{B.1}$$

where we renamed $\tilde{A}(\Omega) \equiv \tilde{A}_{\omega}(\omega_0 + \Omega)$ for brevity.

The product $\tilde{A}(\Omega)\tilde{A}(-\Omega)$ implies that only the pair of frequencies ω_0+Ω and ω_0–Ω contribute to the envelope of the second–harmonic field at $2\omega_0$. To make the pair correlation explicit, a Dirac δ is inserted that enforces the sum condition:

$$\delta(\Omega_1 + \Omega_2) = \begin{cases} 1 & \text{when } \Omega_2 = -\Omega_1, \\ 0 & \text{otherwise.} \end{cases} \tag{B.2}$$

Using the δ–function as just described allows us to introduce two independent integration variables

$$\mathcal{O} = \iint \mathrm{d}\Omega_1\, \mathrm{d}\Omega_2\, \tilde{A}(\Omega_1)\tilde{A}(\Omega_2)\, \Phi\left(\frac{\Omega_1 - \Omega_2}{2}\right) \delta(\Omega_1 + \Omega_2). \tag{B.3}$$

Equation B.3 still evaluates to equation B.1 once the δ-function is used to set $\Omega_2 = -\Omega_1$. The advantage is that it makes explicit the bilinear form of $\mathcal{O}$,

$$\mathcal{O} = \iint \mathrm{d}\Omega_1\, \mathrm{d}\Omega_2\, A(\Omega_1) \underbrace{\left[\Phi\left(\tfrac{\Omega_1 - \Omega_2}{2}\right)\, \delta(\Omega_1 + \Omega_2)\right]}_{K(\Omega_1, \Omega_2)} A(\Omega_2). \tag{B.4}$$

Hence $K(\Omega_1, \Omega_2)$ is the integral-kernel representation of the crystal. Because $\Phi(\Omega)$ is an even function and $\delta(\Omega_1 + \Omega_2) = \delta(\Omega_2 + \Omega_1)$, the kernel is symmetric: $K(\Omega_1, \Omega_2) = K(\Omega_2, \Omega_1)$. That makes the associated operator Hermitian, which for the simplified form of the Schmidt (singular-value) decomposition.

Acting with the operator $(K\tilde{A})$ on the pump spectrum,

$$(K\tilde{A})(\Omega_1) = \int_{-\infty}^{+\infty} \mathrm{d}\Omega_2\, K(\Omega_1,\Omega_2)\tilde{A}(\Omega_2) = \int \mathrm{d}\Omega_2\, \Phi\left(\frac{\Omega_1-\Omega_2}{2}\right)\, \delta(\Omega_1+\Omega_2)\, \tilde{A}(\Omega_2) = \Phi(\Omega_1)\tilde{A}(-\Omega_1), \tag{B.5}$$

and forming the inner product with $\tilde{A}$:

$$\langle A, KA\rangle = \int_{-\infty}^{+\infty} \mathrm{d}\Omega_1\, A(\Omega_1)[KA](\Omega_1) = \int_{-\infty}^{+\infty} \mathrm{d}\Omega_1\, A(\Omega_1)\, A(-\Omega_1)\, \Phi(\Omega_1), \tag{B.6}$$

which is equation B.1. In other words

$$\mathcal{O} = \langle A,\, KA\rangle. \tag{B.7}$$

In algebraic representation

$$\begin{aligned} \mathcal{O} = \langle A,\, KA\rangle = \langle A \,|\, K \,|\, A\rangle &= \left\langle A \,\middle|\, \sum_n \lambda_n\, |u_n\rangle\langle u_n| \,\middle|\, A \right\rangle \\ &= \sum_n \lambda_n\, \langle A|u_n\rangle\langle u_n|A\rangle = \sum_n \lambda_n\, |a_n|^2, \end{aligned} \tag{B.8}$$

where $a_n \equiv \langle u_n|A\rangle$ are the pump's expansion coefficients in the eigen-basis $\{u_n\}$. The mode-matching is the overlap between the pump spectrum and its image under the crystal operator K.